

ANDREW R. MCCLUSKEY
for the degree of DOCTOR OF PHILOSOPHY

COARSE-GRAINED MODELLING FOR SOFT MATTER SCATTERING

UNIVERSITY OF BATH
DEPARTMENT OF CHEMISTRY

DIAMOND LIGHT SOURCE

Copyright © 2019 Andrew R. McCluskey

Attention is drawn to the fact that copyright of this thesis rests with the author. A copy of this thesis has been supplied on condition that anyone who consults it is understood to recognise that its copyright rests with the author and that they must not copy it or use material from it except as permitted by law or with the consent of the author.

This work is licensed under a Creative Commons “Attribution 4.0 International” license.



First printing, April 2019

"ATTICUS TOLD ME TO DELETE THE ADJECTIVES AND I'D HAVE THE FACTS."

Scout Finch – To Kill a Mockingbird

DECLARATION OF AUTHORSHIP

I, Andrew R. McCluskey, declare that this thesis titled "Coarse-grained modelling for soft matter scattering" and the work presented in it are my own. I confirm that:

- where the thesis or any part of the thesis such as a published paper, has been produced jointly with others, that a substantial part is the original work of myself, and
- where the thesis incorporates material already submitted for another degree, the extent of that material and the degree, if any, obtained.

Signed:

Date:

PUBLICATIONS

Some of the information in Chapter 2 has been previously published in:

- A. R. McCluskey *et al.* *Curr. Org. Chem.* 22.8 (2018), pp. 750–757.

Some of the work covered in Chapter 3 has been previously published in:

- A. R. McCluskey *et al.* *Phys. Chem. Chem. Phys.* 21.11 (2019), pp. 6133–6141.

Some of the work covered in Chapter 4 has been previously published in:

- A. R. McCluskey *et al.* *J. Phys. Comm.* Accepted (2019).

Some of the work covered in Chapter ?? has been previously published in:

- A. R. McCluskey *et al.* *J. Open Source Educ.* 1.2 (2018), pp.19–21.
- A. R. McCluskey *et al.* *J. Appl. Crystallogr.* Accepted (2019).

REPRODUCIBILITY STATEMENT

This thesis exists as a piece of completely reproducible research. I have endeavoured to include as much algorithmic and methodological detail within the text, and where relevant working Code Blocks written in Python.

However, in order to provide complete, and easy, reproducibility an electronic supplementary information (ESI) is available online in the form of a Git repository. This ESI provides full details of the analyses performed in this work and access to an automated analysis workflow.

The ESI may be accessed at the following doi:[10.5281/zenodo.xxxxxxx](https://doi.org/10.5281/zenodo.xxxxxxx).

ACKNOWLEDGEMENTS

This is where I will acknowledge people. Need to remember everyone...

CONTENTS

1	<i>Introduction</i>	1
1.1	<i>Soft matter self-assembly</i>	1
1.2	<i>Analysis of soft matter scattering</i>	3
1.3	<i>Coarse-graining of soft matter systems</i>	5
1.4	<i>Optimisation methodologies</i>	5
1.5	<i>Educational materials</i>	6
2	<i>Theory</i>	7
2.1	<i>Probing radiation</i>	7
2.2	<i>Scattering</i>	11
2.3	<i>Classical simulation</i>	24
2.4	<i>Optimisation & sampling methods</i>	29
3	<i>Chemically consistent modelling of X-ray and neutron reflectometry</i>	41
3.1	<i>Introduction</i>	42
3.2	<i>Experimental</i>	45
3.3	<i>Data analysis</i>	46
3.4	<i>Results & Discussion</i>	52
3.5	<i>Conclusions</i>	60
4	<i>Applying atomistic and coarse-grained simulation to reflectometry analysis</i>	61
4.1	<i>Introduction</i>	63
4.2	<i>Methods</i>	66
4.3	<i>Data analysis</i>	68
4.4	<i>Results & Discussion</i>	71
4.5	<i>Conclusions</i>	77

A *Additional Code Blocks for Differential Evolution* 79

LIST OF FIGURES

- 1.1 Three examples of soft matter species; (a) a 43 C₁₀TAB surfactant micelle, reprinted with permission from R. Hargreaves *et al.* *J. Am. Chem. Soc.* 133.41 (2011), pp. 16524–16536, copyright 2011 American Chemical Society, (b) the tunable interactions of colloids, reprinted with permission from D. J. Kraft *et al.* *J. Phys. Chem. B* 115.22 (2011), pp. 7175–7181, copyright 2011 American Chemical Society, and (c) generated using VMD (W. Humphrey *et al.* *J. Mol. Graph.* 14.1 (1996), pp. 33–38) from the crystal structure of T4-lysozyme D. R. Rose *et al.* *Protein Eng. Des. Sel.* 2.4 (1988), pp. 277–282. 2
- 1.2 A graphical representation of the packing parameters and information of the resulting self-assembled structure. 3
- 1.3 Potential energy surfaces for an all-atom vs a coarse-grained potential model, reprinted with permission of the American Chemical Society from S. Kmiecik *et al.* *Chem. Rev.* 116.14 (2016), pp. 7898–7936. 5
- 2.1 A schematic representation of a synchrotron radiation source, identifying the Linac, the booster ring, the radio-frequency cavities (rf), the bending magnet (BM) and the insertion device (ID). Reprinted, with permission of Springer Nature Customer Service Centre GmbH: Springer Nature, from M. C. Garcia-Gutierrez *et al.* “Bases of Synchrotron Radiation, Light Sources, and Features of X-Ray Scattering Beamlines”. In: *Applications of Synchrotron Light to Scattering and Diffraction in Materials and Life Sciences*. 2009, pp. 1–22. 8
- 2.2 A diagram of an undulator insertion device, such as that on I07 and I22, where λ_P is the period length between opposing magnets. Reprinted, with permission of Springer Nature Customer Service Centre GmbH: Springer Nature, from M. C. Garcia-Gutierrez *et al.* “Bases of Synchrotron Radiation, Light Sources, and Features of X-Ray Scattering Beamlines”. In: *Applications of Synchrotron Light to Scattering and Diffraction in Materials and Life Sciences*. 2009, pp. 1–22. 9
- 2.3 A representation of how different techniques can be used to probe various length scales. Reprinted, with permission of Oxford University Press, from D. S. Sivia. *Elementary Scattering Theory: For X-Ray and Neutron Users*. 2011. 11

- 2.4 A schematic of the scattering of some probing radiation by a sample (blue circle). Adapted, with permission of Oxford University Press, from D. S. Sivia. *Elementary Scattering Theory: For X-Ray and Neutron Users*. 2011. 12
- 2.5 A vector diagram describing an elastic scattering event, where \mathbf{k}_i is the incident wavevector, \mathbf{k}_f is the final wavevector, 2θ is the scattering angle, and \mathbf{q} is the scattering vector. Adapted, with permission of Oxford University Press, from D. S. Sivia. *Elementary Scattering Theory: For X-Ray and Neutron Users*. 2011. 12
- 2.6 A schematic showing the propagation of the wave of probing radiation (green lines) radially outwards following the scattering event, where r is the magnitude of the displacement vector. Adapted, with permission of Oxford University Press, from D. S. Sivia. *Elementary Scattering Theory: For X-Ray and Neutron Users*. 2011. 13
- 2.7 A schematic showing the interaction of radiation scattered by two particles that are separated by the vector \mathbf{R}_j . Adapted, with permission of Oxford University Press, from D. S. Sivia. *Elementary Scattering Theory: For X-Ray and Neutron Users*. 2011. 14
- 2.8 A schematic showing the geometry of a typical specular reflectometry experiment from a layered sample. Reprinted, with permission of Oxford University Press, from D. S. Sivia. *Elementary Scattering Theory: For X-Ray and Neutron Users*. 2011. 16
- 2.9 A graphical representation of the kinematic approach; (a) the Heaviside function describing the scattering length density profile of a bare silicon substrate, (b) the δ -function arising from the first derivative of the function in (a), and (c) the reflectometry profile resulting from the kinematic approach, where the orange line at $R = 1$ identifies the break down between experimental and theory in the kinematic approach. Adapted, with permission of Oxford University Press, from D. S. Sivia. *Elementary Scattering Theory: For X-Ray and Neutron Users*. 2011. 18
- 2.10 A schematic diagram showing the reflected (r) and transmitted (t) waves when an incident (i) wave enters an interface of thickness d , where the refractive indices of each layer are n_0 , n_1 , and n_2 . Adapted, with permission of Elsevier, from F. Foglia *et al.* *Curr. Opin. Colloid Interface Sci.* 20.4 (2015), pp. 235–243. 19
- 2.11 A comparison of the kinematic approach (blue solid line), and the dynamical approach (green dashed line), to determine the reflected intensity from the material with the scattering length density profile given in Figure 2.9(a). It is clear that at low q , there is a noticeable deviation between the two. 20
- 2.12 The effect of a Fourier transform (a) the scattering length density profile for some object with a width of 10 Å, (b) the Fourier transform of this object showing the minima in the differential cross section at values of $2n\pi/10$, where n is some integer. 21

- 2.13 A schematic of the D22 instrument of the ILL. Reprinted with permission of Springer Nature Customer Service Centre GmbH: Springer Nature from I. Grillo. "Small-Angle Neutron Scattering and Applications in Soft Condensed Matter". In: *Soft-Matter Characterization*. 2008, pp. 723–782. 22
- 2.14 The Guinier plot, (a) the ideal scattering profile from a sphere of radius 20 Å, (b) the associated Guinier plot, with a straight line (orange) at low- q showing the radius of gyration to be \sim 15.5 Å. 23
- 2.15 The form of each component; attractive (blue), repulsive (orange), of the Lennard-Jones potential model (green) for argon, using parameters in A. Rahman. *Phys. Rev.* 136 (2A 1964), A405–A411. 26
- 2.16 A graphical representation of the periodic boundary conditions. Reprinted, with permission of Elsevier, from D. Frenkel *et al.* *Understanding Molecular Simulation: From Algorithms to Applications*. 1996. 27
- 2.17 Three examples of the MARTINI coarse-graining mechanism for (a) aspartic acid, (b) a water cluster, and (c) a molecule of DPPC. Reprinted with permission of the Institute of Physics, from K. Pluhackova *et al.* *J. Phys. Condens. Matter* 27.32 (2015), p. 323103. 29
- 2.18 An example of a differential evolution (DE) algorithm as applied to an Ackley function, where $a = 20$, $b = 0.2$, and $c = 2\pi$. The mutation and recombination constant in this implementation are both 0.5. Each different coloured line represents a different candidate solution. The optimisation was stopped after 100 iterations had run. 31
- 2.19 An example of a particle swarm optimisation as applied to an Ackley function, where $a = 20$, $b = 0.2$, and $c = 2\pi$. For the particle swarm, the following parameters were used $\omega = 0.9$, $\psi_g = 0.05$, and $\psi_p = 0.05$. Each different coloured line represents a different candidate solution. The optimisation was stopped after 100 iterations had run. 33
- 2.20 An example of a four variable (two nearby Gaussian functions of different sizes with added random noise and some fractional uncertainty) problem probed using a MCMC method, using values of $a = 0.1$, θ_1 and θ_2 correspond to the integral of the Gaussian function, while θ_3 and θ_4 indicate their positions; (a)-(d) histograms of the probability distribution function for each of the variables, and (e) the data (blue circles), the optimised solution (orange line), and a series of probable solutions (green lines) showing the variability present in the data uncertainty. 35
- 3.1 The two phospholipid forms investigated in this work, where R indicates the hydrocarbon tail; (a) phosphatidylglycerol (PG), (b) phosphocholine (PC). 46
- 3.2 The GIXD patterns, where Q_z is the scattering vector normal to the interface and Q_{xy} is that in the plane of the interface; (a) DPPC at 30 mN m⁻¹ and 22 °C, (b) DMPC at 30 mN m⁻¹ and 22 °C, and (c) DMPC at 30 mN m⁻¹ and 7 °C. Note that Q is equivalent to q . 51

- 3.3 The XRR profiles (left) and SLD profiles (right) for each of the four phospholipids; (a) DPPC, (b) DMPC, (c) DLPC, and (d) DMPG, at the four measured surface pressures; increasing in surface pressure from blue, orange, green to red. The different surface pressure XRR profiles have been offset in the y -axis by two orders of magnitude and the SLD profiles offset in the y -axis by $5 \times 10^{-6} \text{ \AA}^{-2}$, for clarity. 54
- 3.4 The NR profiles (left) and SLD profiles (right) for each of the four phospholipids; (a) DPPC at 15 mN m^{-1} , (b) DPPC at 20 mN m^{-1} , (c) DMPC at 20 mN m^{-1} , and (d) DMPC at 25 mN m^{-1} , where the blue data indicates the h-DES contrast, while the orange is the hd-DES. The different surface pressure XRR profiles have been offset in the y -axis by an order of magnitude and the SLD profiles offset in the y -axis by $5 \times 10^{-6} \text{ \AA}^{-2}$, for clarity. 55
- 3.5 The variation of tail layer thickness, d_t , (blue circles) and head group solvation, ϕ_h , (orange squares) with surface pressures for each of the four phospholipids; (a) DPPC, (b) DMPC, (c) DLPC, and (d) DMPG. 56
- 3.6 The probability distribution functions from the chemically-consistent modelling of DLPC; (a) at 20 mN m^{-1} , (b) at 25 mN m^{-1} , (c) at 30 mN m^{-1} , (d) at 35 mN m^{-1} . The Pearson correlation coefficient for each pair of parameters is given in the top corner of each two-dimensional PDF. 59
- 3.7 The sum of the magnitudes for each of the Pearson correlation coefficients for each of the PC-containing lipids. 59
- 4.1 The DSPC monolayer; (a) without water layer and (b) with water layer, visualised using VMD (W. Humphrey *et al.* *J. Mol. Graph.* 14.1 (1996), pp. 33–38). 67
- 4.2 The experimental surface pressure isotherm for DSPC, taken from I. Kubo *et al.* *Thin Solid Films* 393.1-2 (2001), pp. 80–85. 68
- 4.3 The NR profiles (left) and SLD profiles (right) determined at an APM associated with a surface pressure of 30 mN m^{-1} for; (a) the chemically-consistent model, (b) the Slipid all-atom potential model simulations, (c) the Berger united-atom potential model simulations, and (d) the MARTINI coarse-grained potential model simulations. From top-to-bottom the contrasts are as follows; $d_{83}\text{-D}_2\text{O}$, $d_{83}\text{-ACMW}$, $d_{70}\text{-D}_2\text{O}$, $d_{70}\text{-ACMW}$, $\text{h-D}_2\text{O}$, $d_{13}\text{-D}_2\text{O}$, $d_{13}\text{-ACMW}$. The different contrast NR profiles have been offset in the y -axis by an order of magnitude and the SLD profiles offset in the y -axis by $10 \times 10^{-6} \text{ \AA}^{-2}$, for clarity. 71
- 4.4 A comparison of the scattering length density profile for the MARTINI potential model simulations at an APM associated with a surface pressure of 30 mN m^{-1} ; the blue line shows the data where the layer thickness was 1 \AA and no interfacial roughness and the orange line shows that with a layer thickness of 4 \AA and a roughness of 0.4 \AA . 73

- 4.5 The reflectometry and SLD profiles obtained from the first 5 ns of the Slipid potential model simulation, at an APM associated with a surface pressure of 30 mN m^{-1} . From top-to-bottom the contrasts are as follows; $d_{83}\text{-D}_2\text{O}$, $d_{83}\text{-ACMW}$, $d_{70}\text{-D}_2\text{O}$, $d_{70}\text{-ACMW}$, $\text{h-D}_2\text{O}$, $d_{13}\text{-D}_2\text{O}$, $d_{13}\text{-ACMW}$. The different contrast reflectometry profiles have been offset in the y -axis by an order of magnitude and the SLD profiles offset in the y -axis by $10 \times 10^{-6} \text{ \AA}^{-2}$, for clarity. 76
- 4.6 The simulation time-averaged intrinsic density profile of the water molecules (blue dots), and phospholipid components (head groups: green dots, tail groups: red dots), where the phosphorus atoms of the phospholipid heads create the intrinsic surface at $z = 0\text{\AA}$, and the equivalent number density from the chemically-consistent model (orange line). 76

LIST OF TABLES

- 2.1 A comparision of the photon brilliance from different light sources.
Adapted, with permission of Oxford University Press, from D. S.
Sivia. *Elementary Scattering Theory: For X-Ray and Neutron Users.*
2011. 9
- 3.1 Phospholipid component volumes extracted from different literature sources. V_l corresponds to the total phospholipid volume, V_t to the tail group volume, V_h to the head group volume, MD to molecular dynamics simulations, WAXS to wide-angle X-ray scattering, NB to neutral buoyancy, and DVTD to differential vibrating tube densimetry. The values for DPPC are from R. S. Armen *et al. Biophys. J.* 75.2 (1998), pp. 734–744, W.-J. Sun *et al. Phys. Rev. E* 49.5 (1994), pp. 4665–4676, and N. Kučerka *et al. Eur. Biophys. J.* 33.4 (2004), pp. 328–334; P. Balgavý *et al. Acta. Phys. Slovaca* 51.1 (2001), pp. 53–68 respectively, the values for DMPC are from R. S. Armen *et al. Biophys. J.* 75.2 (1998), pp. 734–744 and N. Kučerka *et al. Eur. Biophys. J.* 33.4 (2004), pp. 328–334; P. Balgavý *et al. Acta. Phys. Slovaca* 51.1 (2001), pp. 53–68 respectively, the values for DLPC are from R. S. Armen *et al. Biophys. J.* 75.2 (1998), pp. 734–744 and N. Kučerka *et al. Eur. Biophys. J.* 33.4 (2004), pp. 328–334; P. Balgavý *et al. Acta. Phys. Slovaca* 51.1 (2001), pp. 53–68 respectively, the values for DMPG are from J. Pan *et al. BBA - Biomembranes* 1818.9 (2012), pp. 2135–2148, and the values for POPG are from N. Kučerka *et al. J. Phys. Chem. B* 116.1 (2012), pp. 232–239. 48
- 3.2 The invariant parameters within the chemically-consistent model.
Values for t_t were taken from the Tanford formula (C. Tanford. *The Hydrophobic Effect: Formation of Micelles and Biological Membranes.* 1980), and the SLD values for the DES from A. Sanchez-Fernandez *et al. Phys. Chem. Chem. Phys.* 18.48 (2016), pp. 33240–33249. 50
- 3.3 The best-fit values, and associated 95 % confidence intervals for each of the varying parameters for each phospholipid at the second highest surface pressure measured from XRR. The values of ϕ_h were obtained from the appropriate use of Equation 3.2. Surface pressure has been abbreviated to SP. 53
- 3.4 The best-fit values, and associated 95 % confidence intervals for each of the varying parameters for each phospholipid at the each surface pressure from NR. The values of ϕ_h were obtained from the appropriate use of Equation 3.2. 53

4.1	The different contrasts of phospholipid monolayer and water investigated.	66
4.2	The areas per molecule (APMs) associated with particular surface pressures and the size of the x - and y -cell dimension for a simulation of 100 phospholipid molecules.	68
4.3	The different scattering lengths of the head and tail phospholipid components.	69
4.4	The χ^2 values for each of the reflectometry models at an APM associated with a surface pressure of 30 mN m^{-1} .	72
4.5	The values for the parameters allowed to vary in the fitting of the chemically-consistent model, at each surface pressure measured.	72
4.6	The mean, 95 % quantile, and their spread for the z -dimension position of atoms representative of difference parts of the phospholipid, at an APM associated with a surface pressure of 30 mN m^{-1} .	77

LIST OF CODE BLOCKS

- 2.1 An example Python code block for the Abelès method for the calculation of reflectometry, adapted from A. R. J. Nelson *et al.* *J. Appl. Crystallogr.* 52.1 (2019), pp. 193–200. The input variables are `q_values` which are the q -vectors at which the reflected intensity should be calculated, `sld` which is the array of scattering length densities for the layers, and `d` which is the array of thicknesses for the layers. This will return an array of floats that is the same size as the `q_values` and contains the reflected intensities. 21
- 2.2 Code that may be used to generate the Lennard-Jones energy for a given atomistic system, which accounts for the periodic boundary condition and the energy cut-off distance. The input variables are `coordinates` which is an array of floats describing the position of the `N` particles, `cell` which are the unit cell vectors, `cut_off` which is potential energy cut-off, and `A` and `B` which are the Lennard-Jones potential parameters. This returns an array with the energy for each particle. 27
- 2.3 An example of a simple implementation for a DE algorithm as described in M. Björck. *J. Appl. Crystallogr.* 44.6 (2011), pp. 1198–1204. The input variables are `population` which is an array of floats containing the initial parent population, `f` which is the figure of merit function to be minimised, `km` which is the mutation constant, `kr` which is the recombination constant, `bounds` which is an array of floats giving the minimum and maximum values for the variables, and `max_iter` which is the maximum number of iterations that should be performed. This will return `history` which is a history of the variables that are being fit during the DE algorithm. 32

- 2.4 An example of the particle swarm optimisation algorithm from R. Poli. *J. Artif. Evol. Appl.* 2008 (2008), pp. 1–10. The input variables are `position` which is the initial position vector, `f` which is the figure of merit function to be minimised, `omega` which is the interia weight, `psig` which is the global acceleration constant, `psip` which is the personal acceleration constant, and the `max_iter` which is the maximum number of iterations that should be performed. This will return the `history` which is a history of the variables that are being fit during the PSO. 33
- 2.5 An example of the Metropolis-Hastings MCMC algorithm from N. Metropolis *et al.* *J. Chem. Phys.* 21.6 (1953), pp. 1087–1092; W. K. Hastings. *Biometrika* 57.1 (1970), pp. 97–109. The input variables are `theta` which is an array of floats giving the initial values for the variables, `f` which is the figure of merit function to be minimised, `a` which is the step size for the changes, `data` which is the experimental data, `iterations` which is the number of accepted iterations to obtain, and `nburn` which is the number of accepted iterations to ignore in the burn-in phase. This will return the `history` which is a history of the variables that are being fit during the PSO. 34
- 3.1 The chemically-consistent model class that was implemented in `refnx` Nelson *et al.*, “Refnx: Neutron and X-Ray Reflectometry Analysis in Python”, op. cit.; A. R. J. Nelson *et al.* *Refnx v0.1.2*. 2019. url: <http://doi.org/10.5281/zenodo.2552023>. The input variables are `vol` which is an array of floats containing the initial values for the head and tail group volumes, `b` which is the calculated scattering length for the head and tail groups, `d_h` which is the initial value for the thickness of the head group region, `c_length` which is the number of carbon atoms in the phospholipid tail, `str` which is the name to be given to the object. The `slabs` function will return an array of floats representing the scattering length density profile. 49
- 3.2 The `set_constraints` that was used to impose chemical-consistency on the phospholipid monolayer structure.. The input variables are `lipids` and `structures` which are `refnx` objects that contain information about the phospholipids and monolayers, and `hold_tails`, `hold_rough`, and `hold_phih` are Boolean switches to constrain the tail layer thickness, the interfacial roughness, and the volume fraction of solvent across the different measurements, in this work these were all kept as `False`. 49
- `reports/code_blocks/mutation.py` 79

A.1 The mutation step used in a classical trial method for a differential evolution algorithm, as described in Björck, "Fitting with Differential Evolution: An Introduction and Evaluation", op. cit.	79
reports/code_blocks/recombination.py	79
A.2 The recombination step used in a classical trial method for a differential evolution algorithm, as described in ibid.	79
reports/code_blocks/selection.py	80
A.3 The selection step used in a differential evolution algorithm, as described in ibid.	80

LIST OF ABBREVIATIONS

ACMW	air-contrast matched water
APM	area per molecule
cmc	critical micelle concentration
C₁₀TA⁺	<i>n</i> -decyltrimethylammonium
C₁₀TAB	<i>n</i> -decyltrimethylammonium bromide
C₁₆TAB	<i>n</i> -hexadecyltrimethylammonium bromide
CCP-SAS	collaborative computational project for small angle scattering
CPU	central processing unit
DDM	<i>n</i> -dodecyl- β -D-maltoside
DE	differential evolution
DES	deep eutectic solvent
DLS	Diamond Light Source
DM	<i>n</i> -decyl- β -D-maltoside
DMSO	dimethyl sulfoxide
DLPC	1,2-dilauroyl- <i>sn</i> -glycero-3-phosphocholine
DMPC	1,2-dimyristoyl- <i>sn</i> -glycero-3-phosphocholine
DMPG	1,2-dimyristoyl- <i>sn</i> -glycero-3-phospho-(1'-rac-glycerol)
DSPC	1,2-distearoyl- <i>sn</i> -glycero-3-phosphocholine
DPPC	1,2-dipalmitoyl- <i>sn</i> -glycero-3-phosphocholine
DPC	dodecylphosphocholine
DPD	dissipative particle dynamics
DVTD	differential vibrating tube densimetry
ESI	electronic supplementary information
ESRF	European Synchrotron Radiation Facility
ESS	European Spallation Source
GIXD	grazing-incidence X-ray diffraction
GPU	graphical processing units
hdDES	partially deuterated deep eutectic solvent
hDES	hydrogenated deep eutectic solvent
ILL	Institut Laue-Langevin
LC	Liquid-Condensed
LE	Liquid-Expanded
MCMC	Markov chain Monte Carlo
MD	molecular dynamics
MPI	message passing interface
NB	neutral buoyancy
NPT	constant number, pressure, and temperature

NR	neutron reflectometry
NVE	constant number, volume, and energy
NVT	constant number, volume, and temperature
OER	open education resource
PBC	periodic boundary condition
PC	phosphocholine
PDF	probability distribution function
PFTE	polytetrafluoroethylene
PG	phosphatidylglycerol
PME	particle mesh Ewald
PSO	particle swarm optimisation
RDF	radial distribution function
SANS	small angle neutron scattering
SAS	small angle scattering
SDS	sodium dodecyl sulfate
SLD	scattering length density
SAXS	small angle X-ray scattering
SP	surface pressure
SPC	single point charge
STFC	Science & Technology Facilities Council
ToF	time-of-flight
VMD	visual molecular dynamics
wph	water molecules per head group
WAXS	wide angle X-ray scattering
XRR	X-ray reflectometry

PHYSICAL CONSTANTS

	$\pi = 3.1415\dots$
Planck constant	$h = 6.626 \dots \times 10^{-34} \text{ Js}$
Golden ratio	$\Phi = 1.618 \dots$
dielectric permittivity of the vacuum	$\epsilon_0 = 8.854 \dots \times 10^{-12} \text{ F m}^{-1}$
charge of electron	$e = 1.602 \dots \times 10^{-19} \text{ C}$
Boltzmann constant	$k_B = 1.381 \dots \times 10^{-23} \text{ J K}^{-1}$

LIST OF SYMBOLS

a	step size	
a_0	optimum head-group area	m^2
b	scattering length	m
b	bond length	m
b_i	best candidate solution	
b_0	equilibrium bond length	m
d_h	phospholipid head layer thickness	m
d_t	phospholipid tail layer thickness	m
d_x	length of object	m
k_m	mutation constant	
l_0	length of hydrophobic tail	m
m	mass	kg
n	number of scattering vectors	
n_i	refractive index	
p	packing parameter	
p	parallel component	
q	scattering magnitude	m^{-1}
$q_{i,j}$	electronic charge	
r	displacement vector magnitude	m^{-1}
$r_{n,n+1}$	Fresnel equation coefficient	
s	serial component	
t	time	s
t_F	time-of-flight	s
$A_{1,2,3}$	dihedral constants	J
B	resultant matrix	
E_{bonded}	bonded energy	J
E_k	kinetic energy	J
$E_{\text{non-bonded}}$	non-bonded energy	J
E_{total}	total energy	J
F	some function	
I	intensity	
K_b	bond force constant	J m^{-2}
K_θ	angle force constant	J rad^{-2}
L_F	length-of-flight	m
M_n	layer matrix	
N	number of some item	
N_P	number of magnets	

N_ρ	number density	
$P(q)$	form factor	
R	reflected intensity	
$R_{1,2}$	some random number	
R_g	radius of gyration	m
R_i	incidence rate	s ⁻¹
R_s	radius of sphere	m
S	surface area	m ²
$S(q)$	structure factor	
T	temperature	K
U	uniform distribution	
V	volume	m ³
V_c	volume of hydrophobic tail	m ³
V_h	phospholipid head volume	m ³
V_n	volume of layer	m ³
V_p	volume of particle	m ³
V_t	phospholipid tail volume	m ³
a	acceleration	m s ⁻²
f	force	N
g	global best	
k_i	incident wavevector	m ⁻¹
k_f	final wavevector	m ⁻¹
m	mutant vector	
o	offspring population	
p	parent population	
q	scattering wavevector	m ⁻¹
r	displacement	m
s	personal best	
v	velocity	m s ⁻¹
x	position	m
R	particle position	m
β_c	fraction of the speed of light	
β_n	phase factor	
δ	infinitesimally small change	
ε	depth of potential well	J
ζ	figure of merit	
2θ	scattering angle	rad
θ	angle	rad
θ	some solution	
θ_0	equilibrium angle	rad
θ_c	critical angle	rad
θ_e	angle between electron and photon	rad
λ	wavelength	m
π	surface pressure	mN m ⁻¹
σ	distance at zero	m
σ_{coh}	coherent scattering cross-section	m
σ_{incoh}	incoherent scattering cross-section	m
$\sigma_{n,n+1}$	interfacial roughness	m

ϕ	scattering angle	
ϕ	dihedral angle	rad
ϕ_g	global acceleration coefficient	
ϕ_i	volume fraction of solvation	
ϕ_p	personal acceleration coefficient	
χ^2	a figure of merit	
ψ_0	wave at point 0	
ψ_i	wave at point i	
ψ_f	final scattered wave	
ω	frequency	s^{-1}
ω	initial weight	
ω_i	incident frequency	s^{-1}
ω_f	final frequency	s^{-1}
Δt	timestep	s
Θ	new solution	
Φ	incident flux	
$d\sigma(q)/d\Omega$	differential cross-section	

ABSTRACT

This work uses different coarse-graining methodologies to assist in the analysis of scattering measurements from soft matter aggregates, such as surfactant monolayers and micelles. The term ‘coarse-graining’ is used broadly in this work; to describe the coarse-graining of a classical simulation potential model, a surfactant monolayer model that consists two layers, and a severe coarse-graining methodology that describes a surfactant molecule as just a position and direction in space. In all three cases, the aim of the applied coarse-graining is to improve the methods of analysis that may be performed in the analysis of reflectometry and small angle scattering measurements.

A surfactant monolayer model, that was considerate of the chemical bond between the surfactant heads and tails, was developed for the analysis of reflectometry measurements from a phospholipid monolayer at the interface between air and a deep eutectic solvent. This model allowed for a unique insight into the structure of the monolayer at the given interface. To assess the utility of coarse-grained potential models in the analysis of neutron reflectometry, a phospholipid monolayer was simulated using three different potential models, of different particle grain-size. This allowed for a better understanding of the simulation resolution necessary to accurately and successfully apply simulation-driven analysis to reflectometry. Finally, a severely coarse-grained description of a surfactant was used in a particle swarm optimisation to try and develop a starting structure for a multiple micelle simulation, where the experimental scattering profile was the optimisation target.

Alongside the development and application of coarse-graining methodologies, the final chapter of this work describes the development of open-source software and teaching materials for the introduction of classical molecular simulation. These educational resources introduce scattering users to simulation and its utility in scattering analysis, to enable a future where simulation driven analysis may be performed accurately by all.

1

INTRODUCTION

The aim of this work is to investigate a series of different coarse graining methodologies that can be used in the analysis of scattering data from soft matter. The coarse graining used in this work includes traditional potential model coarse graining,¹ applying a layer-based coarse grained description of a surfactant monolayer to the analysis of reflectometry, and developing a severely coarse grained description of a surfactant molecule to allow the easy generation of realistic starting structures² from experimental data. From this work, I hope that those interested in using coarse grained approaches for the analysis of scattering data will be able to better understand the avenues that are open to them and the possibly pitfalls that are present.

Soft matter is an umbrella term for many different types of material. These include micelles; sub-micron sized, dynamic agglomerates of amphiphilic molecules such as surfactants or block co-polymers, colloidal solutions; where the interaction between the colloids may be controlled through chemical modification, or proteins; where the polar nature of different amino acids leads to the protein folding into a highly organised, and biologically relevant, shape. Some examples of these soft matter systems are shown in Figure 1.1. These species, initially, appear rather disparate, however, there are a few important commonalities among soft matter systems:³

- the lengths scales are intermediate between atomistic and macroscopic,⁴
- for soft matter systems the energy of a structural distortion is similar to thermal energy, so the material is in constant flux,
- this thermal motion can lead to the formation of complex, hierarchical structures due to the balance between enthalpy and entropy, this process is referred to as self-assembly.

1.1 SOFT MATTER SELF-ASSEMBLY

Soft matter self-assembly is the ability for soft matter systems to form organised structures in solution. These are of particular inter-

¹ Such as the use of the MARTINI potential model.

² For use in classical simulation.

³ R. A. L. Jones. *Soft Condensed Matter*. 2002.

⁴ typically 1×10^{-8} - 1×10^{-5} m.

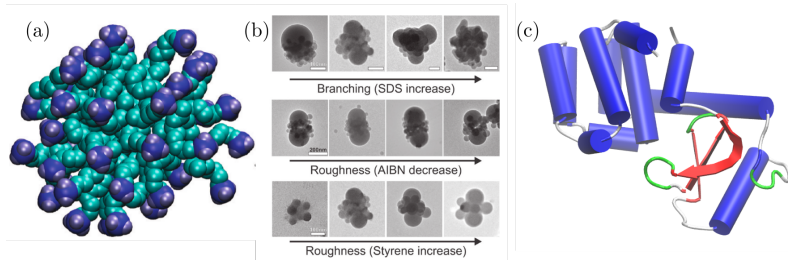


Figure 1.1: Three examples of soft matter species; (a) a 43 C₁₀TAB surfactant micelle, reprinted with permission from R. Hargreaves *et al.* *J. Am. Chem. Soc.* 133.41 (2011), pp. 16524–16536, copyright 2011 American Chemical Society, (b) the tunable interactions of colloids, reprinted with permission from D. J. Kraft *et al.* *J. Phys. Chem. B* 115.22 (2011), pp. 7175–7181, copyright 2011 American Chemical Society, and (c) generated using VMD (W. Humphrey *et al.* *J. Mol. Graph.* 14.1 (1996), pp. 33–38) from the crystal structure of T4 lysozyme D. B. Rose *et al.* *Protein Eng. Des. Sel.* 2.4 (1988), pp. 271–282.

⁵ L. L. Schramm *et al.* *Annu. Rep. Prog. Chem., Sect. C: Phys. Chem.* 99 (2003), pp. 3–48.

⁶ K. Simons *et al.* *Nat. Rev. Mol. Cell Biol.* 1 (2000), pp. 31–39.

⁷ J. Israelachvili. *Intermolecular and Surface Forces*. 2011.

⁸ D. Schmaljohann. *Adv. Drug Deliv. Rev.* 58.15 (2006), pp. 1655–1670; M. Sammalkorpi *et al.* *J. Phys. Chem. B* 113.17 (2009), pp. 5863–5870.

⁹ M. J. Rosen *et al.* *Surfactants and Interfacial Phenomena*. 2012.

¹⁰ J. Goodwin. *Colloids and Interfaces with Surfactants and Polymers*. 2009.

¹¹ Ibid.

¹² The lowest temperature at which agglomerates will form.

est industrially, where surfactant and polymer self-assembly play an import role in food, commodity, and specialty chemicals.⁵ Self-assembly processes are important from a biological perspective as it is phospholipids, a family of surface-active biomolecules, which make up the bilayers that protect cells.⁶ The structures that result from the self-assembly of soft matter species have fluid-like properties. This is due to the fact that the subunits are held together by weak forces such as the van der Waals, hydrophobic, hydrogen-bonding, and screened electrostatic interactions.⁷ This means that the structure of a self-assembled species is susceptible to changes in the local chemical environment, such as pH or salt concentration.⁸

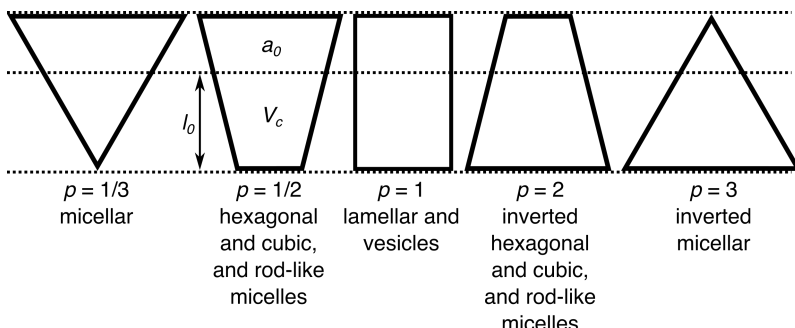
The focus of this work is on the self-assembly of surfactant molecules. Surfactant is a general term for any molecule which is “surface-active”, to say that they will interact at an interface.⁹ Surfactants are generally made up of two components; one part is highly soluble in one of the interfacial phases, while the other is not.¹⁰ Usually, surfactants consist of a hydrocarbon tail, which is hydrophobic, and some hydrophilic head group, which can be ionic or non-ionic. When surfactants are present in water, the two components will interact differently with the solvent. A hydration sphere of water molecules will form around the hydrophilic head group, effectively allowing the head group to take part in the water’s hydrogen-bonding network. Whereas, the lyophilic tail has a structure-breaking effect on the hydrogen bonding network, termed the “hydrophobic effect”. The free energy deficit of this structure-breaking can be reduced through the aggregation of these hydrophobic groups, as the van der Waals attraction between tail groups is larger than that present between tail groups and water molecules. There is a decrease in entropy from the tail organisation, however, this is offset by the entropic increase from the water structure breakup. Finally, by considering the effect of the, often charged, head groups being close together, it is thought that the majority of the charge can be screened by the presence of a counter-ion, or water molecules, bound to the head group.¹¹ This means that at low concentrations, where it is statistically unlikely for an agglomerate to form, there will be a higher concentration of surfactants at the air-water interface, and as the concentration is increased, assuming the system is above the Krafft temperature,¹²

organised structures will begin to appear.

The structures can be formed from surfactant solutions are diverse; featuring micellar, hexagonal, cubic, and lamellar mesophases. These mesophases have a significant impact on the macroscopic properties of the system, for example the liquid crystalline hexagonal phase can present interesting viscoelastic behaviour.¹³ The mesophase that is formed is dependent on the shape of the underlying surfactants. Israelachvili described this dependency in terms of the dimensionless surfactant packing parameter, p .¹⁴

$$p = \frac{V_c}{a_0 l_0}, \quad (1.1)$$

where, V_c is the volume of the hydrophobic tail, l_0 is the length of the tail, and a_0 is the optimum head group area. This parameter can be used to estimate the geometry of the resulting self-assembled structure, detailed in Figure 1.2. It is important to note that the optimum head group area accounts for the hydration sphere of the head group. A short tail surfactant, such as *n*-decyltrimethylammonium bromide,¹⁵ will have a very small packing parameter resulting in small spherical micelles. Whereas, the twin-tailed phospholipids, such as 1,2-dipalmitoyl-*sn*-glycero-3-phosphocholine,¹⁶ will have a much larger packing parameter due to the larger tail volume and length, therefore this surfactant will form a lamellar bilayer in solution.



¹³ D. Jurašin *et al.* *Soft Matter* 9.12 (2013), p. 3349; F. Cordobés *et al.* *J. Colloid Interface Sci.* 187.2 (1997), pp. 401–417.

¹⁴ Israelachvili, *Intermolecular and Surface Forces*, op. cit.

¹⁵ Commonly abbreviated to C₁₀TAB.

¹⁶ Known as DPPC.

Figure 1.2: A graphical representation of the packing parameters and information of the resulting self-assembled structure.

This work will focus on the investigation of surfactant monolayers and micellar systems. These represent interesting model systems of significant interest both technologically¹⁷ and biologically.¹⁸ Both of these systems are regularly investigated using X-ray and neutron elastic scattering techniques, with analysis performed in a model-dependent fashion.¹⁹

1.2 ANALYSIS OF SOFT MATTER SCATTERING

The use of neutron and X-ray scattering experiments for the study of soft matter is well developed, with early research into the structure of phospholipid monolayers by reflectometry methods being conducted in the late 1970s by Albrecht *et al.*²⁰ While, the work of

¹⁷ N. Anton *et al.* *Int. J. Pharm.* 398.1-2 (2010), pp. 204–209; M. Zagnoni. *Lab on a Chip* 12.6 (2012), p. 1026.

¹⁸ K. Kataoka *et al.* *Adv. Drug Deliv. Rev.* 64 (2012), pp. 37–48; H Mohwald. *Annu. Rev. Phys. Chem.* 41 (1990), pp. 441–476; S. Kewalramani *et al.* *J. Phys. Chem. Lett.* 1.2 (2010), pp. 489–495.

¹⁹ E. Pambou *et al.* *Langmuir* 31.36 (2015), pp. 9781–9789; D. W. Hayward *et al.* *Macromolecules* 48.5 (2015), pp. 1579–1591; I. Rodriguez-Loureiro *et al.* *Soft Matter* 13.34 (2017), pp. 5767–5777; G. Hazell *et al.* *J. Colloid Interface Sci.* 474 (2016), pp. 190–198.

²⁰ O. Albrecht *et al.* *J. Phys. France* 39.3 (1978), pp. 301–313.

- ²¹ O Kratky *et al.* *J. Colloid Sci.* 4.1 (1949), pp. 35–70; *et al.* *Angew. Chemie Int. Ed.* 53.43 (2014), pp. 11524–11528.
- ²³ V. Rondelli *et al.* *J. Phys. Conf. Ser.* 340 (2012), p. 012083.

²⁴ P. A. Hassan *et al.* *J. Colloid Interface Sci.* 257.1 (2003), pp. 154–162, see Section 2.2.7.

²⁵ R. A. Campbell *et al.* *J. Colloid Interface Sci.* 531 (2018), pp. 98–108; J. R. Lu *et al.* *Acta Crystallogr. A* 52.1 (1996), pp. 11–41, see Section 2.2.7.

²⁶ J. S. Pedersen. “Monte Carlo Simulation Techniques Applied in the Analysis of Small-Angle Scattering Data from Colloids and Polymer System”. In: *Neutron, X-Rays and Light. Scattering Methods Applied to Soft Condensed Matter*. 2002, pp. 381–390.

²⁷ M. Wormington *et al.* *Philos. Trans. R. Soc. London Ser. A* 357.1761 (1999), pp. 2827–2848.

²⁸ Nelson *et al.*, “Refnx: Neutron and X-Ray Reflectometry Analysis in Python”, op. cit.

²⁹ Such as molecular dynamics.

³⁰ E. Scoppola *et al.* *Curr. Opin. Colloid Interface Sci.* 37 (2018), pp. 88–100.

³¹ The historical context of this is discussed briefly in Chapter ??.

³² S. Bowerman *et al.* *J. Chem. Theory Comput.* 13.6 (2017), pp. 2418–2429.

³³ In the form of Empirical Potential Structure Refinement.

³⁴ R. Hargreaves *et al.* *J. Am. Chem. Soc.* 133.41 (2011), pp. 16524–16536.

³⁵ M. T. Ivanović *et al.* *Angew. Chemie Int. Ed.* 57.20 (2018), pp. 5635–5639.

³⁶ A. F. Miller *et al.* *Mol. Phys.* 101.8 (2003), pp. 1131–1138; P. M. Anderson *et al.* *J. Chem. Phys.* 121.17 (2004), p. 8503.

³⁷ Monte Carlo and molecular dynamics respectively.

Kratky and Porod,²¹ who used small angle X-ray scattering for the study of colloidal systems was published in 1949. Since these early works, instrumentation developments have enabled more challenging experiments to be conducted, such as time-resolved studies²² and the study of floating phospholipid bilayers.²³

However, the analysis of soft matter scattering has changed little since these early works, still typically involving the use of very coarse models. These include the shape-based modelling common in small angle scattering²⁴ and reflectometry analysis.²⁵ More sophisticated model refinements have been developed, such as the use of Monte-Carlo sampling,²⁶ differential evolution optimisation,²⁷ and Bayesian inference.²⁸ However, there has been little change in the definition of the models that unpin the analysis processes. Recently, there have been movements towards the use of atomistic modelling techniques²⁹ to augment, and assist, the analysis of soft matter scattering measurements, in a multi-modal approach.³⁰

Much of the work relating to the use of atomistic simulation for the analysis of small angle scattering measurements has been focused on the study of protein molecules in solution.³¹ This has allowed for a more profound understanding aspects of biology such as the conformational states available to protein molecules in solution.³² The uptake of atomistic simulation for the analysis of small angle scattering from systems such as micelles has been slower, in part due to the more complex conformation landscape available to these systems under standard conditions. However, the work of Hargreaves *et al.* paired atomistic simulation with total scattering measurements³³ to resolve the structure of a simple short-tail surfactant micelle.³⁴ Further, the work of Ivanović *et al.* used scattering experiments to refine the output of molecular dynamics simulations of micelles of a pre-defined size.³⁵ Both of these examples required significant computational resource; in the former case, the computational time taken was quoted as 200 days, while the later required the running of multiple simulations at different micelle sizes in order to determine the appropriate simulation.

The use of atomistic simulation for the analysis reflectometry measurements of soft matter systems began with the work of Miller *et al.* and Anderson and Wilson,³⁶ where atomistic simulations³⁷ were used to study polymer self-assembly at the oil-water interface. These simulation trajectories was then compared with experimental neutron reflectometry measurements. Dabkowska *et al.* also used atomistic simulation and neutron reflectometry measurements to study the structure of a surfactant monolayer at the air-water interface, providing the first example of a direct comparison between experimental reflectometry data and that determined from simulation.³⁸ To date, there is only one work that has used coarse-grained molecular dynamics simulation to aid in the analy-

- ³⁸ A. P. Dabkowska *et al.* *Langmuir* 30.29 (2014), pp. 8803–8811.

sis of neutron reflectometry, this is the work of Koutsoubas.³⁹ This work made use of the MARTINI coarse-grained forcefield to simulate a phospholipid bilayer, and was compared with experimental neutron reflectometry measurements.

1.3 COARSE-GRAINING OF SOFT MATTER SYSTEMS

The characteristic non-atomistic length scales associated with soft matter systems make them ideal for the application of coarse-graining protocols. Coarse-graining is where the dimensionality of a problem is reduced by the removal of certain degrees of freedom from a set. The most common method of coarse-graining is the re-parameterisation of an atomistic molecular dynamics potential model in terms of this reduced parameter space. An example of this is the MARTINI forcefield,⁴⁰ where the aim is to reparameterise the system without significant loss of chemical information.⁴¹ A result of coarse-graining is the creation a flatter potential energy landscape, as shown in Figure 2.17. The availability of coarse-grained potential models and tools for coarse-graining as allowed for very large simulations to be performed, such as the simulation of large polymeric species,⁴² phospholipid nanodiscs,⁴³ and realistic biomembranes.⁴⁴ Furthermore, these coarse-grained potential model have shown the ability to reproduce experimental measurements.⁴⁵

However, in this work I have used the term “coarse-graining” broadly to include the applications of a chemically-consistent coarse-grained monolayer model for the analysis of reflectometry data,⁴⁶ In addition to the assessment of different atomistic and coarse-grained potential models for the analysis of neutron reflectometry, building on the work of Dabkowska *et al.* and Koutsoubas.⁴⁷

1.4 OPTIMISATION METHODOLOGIES

The availability of high performance computing has increased significantly in recent years, in particular due to cloud-based infrastructures. Furthermore, highly parallelisable optimisation algorithms are now available such as the particle swarm⁴⁸ and differential evolution⁴⁹ optimisations. As mentioned above, previous work has shown that the simulation of a surfactant micelle and comparison with experimental data requires significant computational expense⁵⁰ In the interest of reducing this, and improving the applicability of high performance computing to simulation-driven analysis of small angle scattering I have investigated the use of a particle swarm optimisation (PSO) to produce a realistic, near-atomistic micelle structure based on experimental data alone. This has made use of a coarse-grained description of a surfactant molecule on two levels; one for the particle swarm optimisation

³⁹ A. Koutsoubas. *J. Phys. Chem. B* 120.44 (2016), pp. 11474–11483.

⁴⁰ This specific model is discussed in greater detail in Section 2.3.3.

⁴¹ S. J. Marrink *et al.* *J. Phys. Chem. B* 111.27 (2007), pp. 7812–7824.

⁴² P. Carbone *et al.* *J. Chem. Phys.* 128.6 (2008), p. 064904.

⁴³ M. Xue *et al.* *Biophys. J.* 115.3 (2018), pp. 494–502.

⁴⁴ S. J. Marrink *et al.* *Chem. Rev.* (2019), acs.chemrev.8b00460.

⁴⁵ E. Negro *et al.* *Soft Matter* 10.43 (2014), pp. 8685–8697; S. Nawaz *et al.* *Soft Matter* 8.25 (2012), p. 6744.

⁴⁶ This work is the focus of Chapter 3.

⁴⁷ Dabkowska *et al.*, “Modulation of Dipalmitoylphosphatidylcholine Monolayers by Dimethyl Sulfoxide”, op. cit.; Koutsoubas, “Combined Coarse-Grained Molecular Dynamics and Neutron Reflectivity Characterization of Supported Lipid Membranes”, op. cit., see Chapter 4.

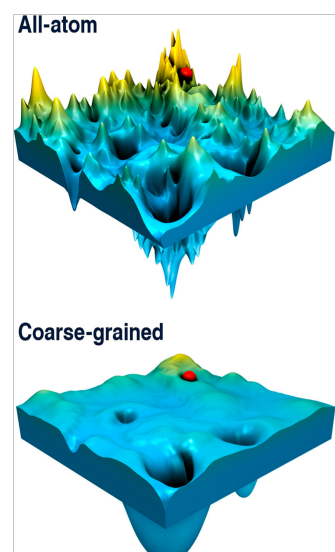


Figure 1.3: Potential energy surfaces for an all-atom vs a coarse-grained potential model, reprinted with permission of the American Chemical Society from

⁵¹ See Chapter ??.

and another for the scattering profile calculation.⁵¹.

1.5 EDUCATIONAL MATERIALS

While the development of analytical methods and infrastructure are important for the development and uptake of the simulation-driven analysis methods applied in this work, the development of informative resources is also necessary. Current experimental users of small angle scattering are typically not familiar with detailed aspects of classical simulation, however, they are often interested in applying it to assist with their analyses. Therefore, alongside traditional research applications, I have been developing open educational resources⁵² designed to introduce classical simulation techniques, and to allow users of scattering techniques to become familiar with these. The ambition being that as the availability of simulation-driven analysis for small angle scattering grows, so will the user base that is familiar with the underlying methods.⁵³

⁵² Abbreviated to OERs

⁵³ See Chapter ??.

2

THEORY

2.1 PROBING RADIATION

This work is focussed on the use of X-ray and neutron scattering to probe soft matter systems; in particular surfactant monolayers and micelles. Therefore, it is pertinent to discuss how each of these probing radiation is produced and detail the advantages of each with respect to the other.

2.1.1 Generation of X-rays

X-rays are a form of electromagnetic radiation similar to visible light, albeit with a much shorter wavelength.¹ There are four common ways to produce X-rays; three are available within the laboratory, while the other is exclusive to large scale facilities.

The three laboratory source X-ray generation techniques are the X-ray tube, the rotating anode, and the liquid jet. An X-ray tube consists of a filament and an anode within a vacuum chamber, by passing a high voltage electrical current across the filament electrons are emitted which accelerate towards the anode. On collision with the anode, the rapid deceleration results in the emission of X-rays at a characteristic wavelength based on the anode material.² The most common material for an X-ray tube anode is copper which gives off radiation with an energy of $\sim 8 \text{ keV}$.³

Another common laboratory method for the generation of X-rays is the rotating anode.⁴ In the X-ray tube, each time that an electron collides with anode there is some energy transfer, this means that over many millions of collisions the temperature of the anode can rise significantly, which can cause the anode material to melt. Resulting in a temperature-based limitation to the available X-ray flux. This lead to the development of the rotating anode, which is simply where the anode is made from a rotating wheel, such that the bombardment is spread across the whole wheel reducing the energy localisation. The use of a rotating anode can allow for an increase in the photon flux by about an order of magnitude.⁵

The final laboratory method for X-ray generation is the liquid jet source.⁶ For the liquid jet X-ray source, an electron beam is

¹ Typically 0.01-10 nm.

² H. Schnablegger *et al.* *The SAXS Guide: Getting Acquainted with the Principles*. 2017.

³ This is a wavelength of $\sim 1.5 \text{ nm}$.

⁴ Essentially an improvement on the X-ray tube.

⁵ Schnablegger *et al.*, *The SAXS Guide: Getting Acquainted with the Principles*, op. cit.

⁶ MetalJet X-Ray Source Technology. URL: <https://www.exillum.com/technology/> (Accessed 2018-12-6), Branded MetalJet by exillum.

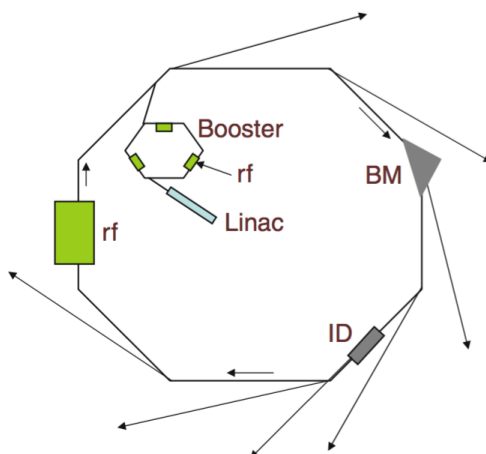
⁷ Usually an gallium or indium alloy.

⁸ Such as Diamond Light Source (DLS) or the European Synchrotron Radiation Facility (ESRF).

incident on a liquid metal sample,⁷ rather than traditional solid metal, which can dissipate heat more efficiently. This means that the electron intensity and therefore X-ray brightness, available to the liquid jet source is much greater than a rotating anode source.

The method of X-ray generation that is not available in a typical laboratory is at a synchrotron, the use of this method has the drawback that it requires access to a national or international facility.⁸ The way in which X-rays are generated at a synchrotron involves the acceleration of an electron, rather than the deceleration as with the laboratory sources. This is achieved by having relativistic electrons travel on a curve, from Newtonian mechanics it is known that travelling on a curve at constant speed is equivalent to acceleration. First the electrons are accelerated, after being produced in a linear accelerator, to near the speed of light in a booster synchrotron before injecting them into the storage ring. In the storage ring, the electrons are kept at relativistic speeds with bending magnets and straight sections making up a ring as shown in Figure 2.1. How circular the ring is depends on the number of bending magnets that make it up; for example, DLS had 48 bending magnets with 48 straight sections at the time of construction.

Figure 2.1: A schematic representation of a synchrotron radiation source, identifying the Linac, the booster ring, the radio-frequency cavities (rf), the bending magnet (BM) and the insertion device (ID). Reprinted, with permission of Springer Nature Customer Service Centre GmbH: Springer Nature, from M. C. Garcia-Gutierrez *et al.* "Bases of Synchrotron Radiation, Light Sources, and Features of X-Ray Scattering Beamlines". In: *Applications of Synchrotron Light to Scattering and Diffraction in Materials and Life Sciences*. 2009, pp. 1–22.



When an electron accelerates (or travels on a curve), Cherenkov radiation is emitted in accordance with the Cherenkov relation,

$$n_i \beta_c \cos \theta_e = 1, \quad (2.1)$$

where, n_i is the refractive index for the dielectric medium, β_c is the fraction of the speed of light at which that electron is travelling, and θ_e is the angle between the electron trajectory and the trajectory of the resulting photon.⁹ The curve is the result of a bending magnet, meaning that at each bending magnet there can be a beamline which uses the synchrotron light. The light that is given off from a bending magnet is continuous and broad, covering a wide range of the electromagnetic spectrum. The alternative to a bending magnet beamline is that which is served by an insertion device.

⁹ M. C. Garcia-Gutierrez *et al.* "Bases of Synchrotron Radiation, Light Sources, and Features of X-Ray Scattering Beamlines". In: *Applications of Synchrotron Light to Scattering and Diffraction in Materials and Life Sciences*. 2009, pp. 1–22.

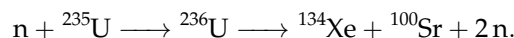
An insertion device is able to offer more specific radiation characteristics (photon energy, narrower band) than a bending magnet, and are placed on the straight sections of the synchrotron. Common insertion devices include wavelength shifters, wigglers, and undulators.

The type of insertion device that is present at both I07 and I22 at DLS is an undulator. An undulator consists of a series of magnets of opposing polarity that causes the electrons to ‘wiggle’ back and forth as shown in Figure 2.2. This results in a superposition of radiation from N_P sources, where N_P is the number of magnets, yielding quasi-monochromatic radiation. The brilliance of different X-ray sources are compared in Table 2.1, this shows the significant benefit that an undulator can offer in terms of photon brilliance.

2.1.2 Generation of neutrons

Neutrons hold an advantage over X-rays, particularly for application to the study of soft matter, due to the ability to use contrast variation to increase the quantity of information from the sample.¹⁰ However, neutrons cannot be produced safely on a laboratory scale, therefore it is always necessary to visit large scale facilities to harness neutrons for scattering experiments. These facilities come in two flavours; the reactor source and the spallation source, each offering unique benefits.

Neutron reactor sources¹¹ are currently the most common format of neutron source and are capable of producing the highest average neutron flux.¹² The High-Flux Reactor at the ILL is capable of producing a neutron flux of 1.5×10^{15} neutrons $s^{-1}cm^{-2}$.¹³ A reactor source operates on the principle of nuclear fission, where an atomic nucleus is capable of breaking down into smaller nuclei, overcoming the strong nuclear force. This often involves using uranium enriched with its fissile isotope, ^{235}U , which after the initial absorption of a stray neutron¹⁴ will undergo fission to release, on average, 2.5 daughter neutrons, an example of a possible uranium fission mechanism is:



This type of mechanism is the basis for both research, and nuclear power, reactors.¹⁵ One of the major drawbacks for reactor neutron sources is the perceived public opinion towards such facilities. Major safety concerns, such as “nuclear meltdown” and the resulting

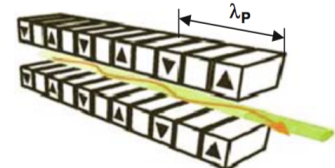


Figure 2.2: A diagram of an undulator insertion device, such as that on I07 and I22, where λ_P is the period length between opposing magnets. Reprinted, with permission of Springer Nature Customer Service Centre GmbH: Springer Nature, from Garcia-Gutierrez *et al.*, “Bases of Synchrotron Radiation, Light Sources, and Features of X-Ray Scattering Beamlines”, op. cit.

¹⁰ This is discussed in detail in Section ??.

¹¹ Such as the Institut Laue-Langevin (ILL) in Grenoble, France.

¹² The number of neutrons per second per unit area.

¹³ ILL: *Neutron for Science: Technical Characteristics*. URL: <https://www.ill.eu/reactor-environment-safety/high-flux-reactor/technical-characteristics/> (Accessed 2016-8-8).

¹⁴ Arising from a cosmic ray, or spontaneous fission.

¹⁵ D. S. Sivia. *Elementary Scattering Theory: For X-Ray and Neutron Users*. 2011.

Light source	Approximate brilliance/ photons $s^{-1}mrad^{-2}0.1\%bandwidth^{-1}$
Candle	1×10^5
X-ray tube	1×10^8
Sun	1×10^{10}
Bending magnet	1×10^{15}
Undulator	1×10^{20}

Table 2.1: A comparison of the photon brilliance from different light sources. Adapted, with permission of Oxford University Press, from D. S. Sivia. *Elementary Scattering Theory: For X-Ray and Neutron Users*. 2011.

nuclear waste, mean that reactor sources are often unpopular and therefore struggle to obtain funding required for operation.

The other form of neutron source is a spallation source, this is much less controversial as it does not require fissile materials and hence there is no risk of a nuclear disaster. The ISIS Neutron and Muon Source is an example of a spallation source, where high energy protons, 800 MeV,¹⁶ are accelerated towards a tungsten target. When the protons strike the target, they can cause the release of a series of neutrons, the first batch of neutrons are given off with too high an energy to be useful, however, less excited neutrons are given off by secondary emissions. In addition to the public perception benefit, spallation sources also offer a technological advantage in the time-of-flight¹⁷ technique. The ToF technique relies the fact that at a spallation source, it is possible to know the time at which the neutron was ejected from the target to a high level of precision and therefore it is possible to measure the time taken for the neutron to reach the instrument. Since the neutron is a particle of a finite mass, m , it is possible to correlate the velocity, \mathbf{v} , of the particle with the kinetic energy, E_k ,

$$E_k = \frac{m\mathbf{v}^2}{2}, \quad (2.2)$$

and with knowledge of the energy of the particle, its wavelength, λ , can be determined by the de Broglie relation,¹⁸

$$E = h\omega = \frac{h\mathbf{v}}{\lambda}, \quad (2.3)$$

where, h is Planck constant and ω is the neutron frequency. Therefore, the wavelength of the neutron is proportional to the inverse of the particle's velocity, and hence the time-of-flight, t_F ,

$$\lambda = \frac{h}{m\mathbf{v}} = \frac{ht_F}{mL_F}, \quad (2.4)$$

where, L_F is the distance between the target and the instrument. The fact that the neutrons can spread out in the flight from the target means that wavelength-dispersive techniques, where the neutron wavelength is measured rather than the scattering angle, are possible at spallation sources which cannot be carried out natively at reactor sources. The weakness of current spallation sources is that they have a lower average flux than reactor sources, however, the construction of the European Spallation Source¹⁹ will change this as it offers an average flux similar to that of a reactor source with the benefits of the spallation technique.

A problem that is inherent for both reactor and spallation sources is that the energy of the neutrons given off is usually too high to be used to study condensed materials, such as soft matter. This means that moderation must be used to reduce the energy of the neutrons passing through the sample. The neutrons that are considered to be optimal for the study of condensed materials are

¹⁶ ISIS – How ISIS Works. URL: <https://www.isis.stfc.ac.uk/Pages/What-does-ISIS-Neutron-Muon-Source-do.aspx> (Accessed 2018-9-25).

¹⁷ Abbreviated to ToF.

¹⁸ L. de Broglie. *Ann. Phys. (Paris)* 10.3 (1925), pp. 22–125.

¹⁹ Known as the ESS.

thermal in nature, named because their energy is approximately that of ambient temperature. Thermal neutrons are achieved by allowing the neutrons to pass through a large volume of moderator material, usually, graphite, D₂O, methane or H₂, stored at 300 K before they reach the instrument.²⁰

²⁰ Sivia, *Elementary Scattering Theory: For X-Ray and Neutron Users*, op. cit.

2.2 SCATTERING

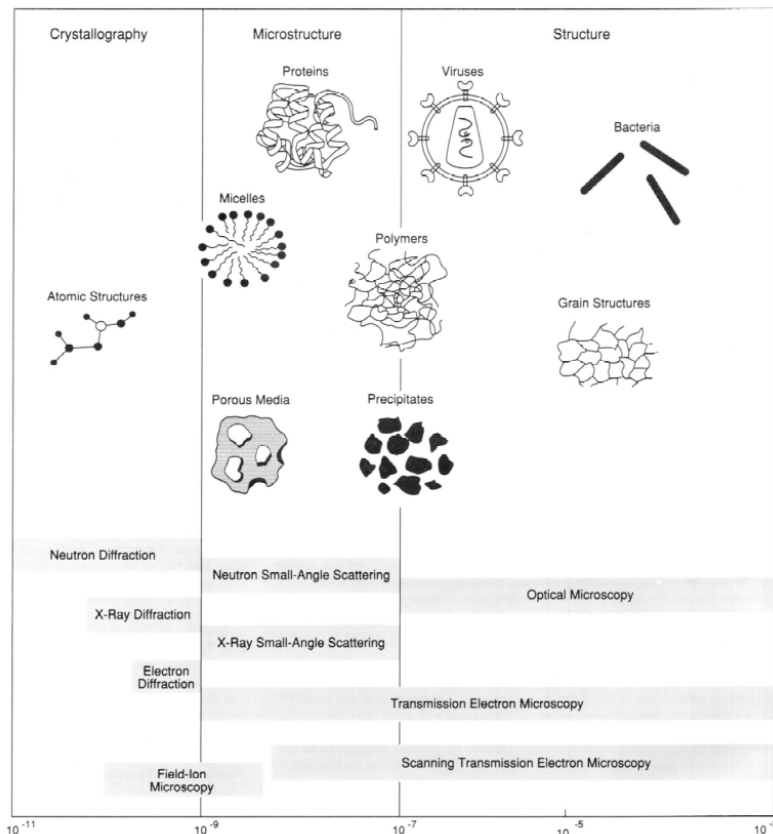


Figure 2.3: A representation of how different techniques can be used to probe various length scales. Reprinted, with permission of Oxford University Press, from D. S. Sivia. *Elementary Scattering Theory: For X-Ray and Neutron Users*. 2011.

The use of scattering techniques to probe soft condensed matter systems is commonplace. In this work, we have focussed on the use of small angle scattering²¹ and reflectometry techniques. These are particularly appropriate for application to soft condensed matter systems due to the length scales capable of being probed being similar to the persistence length of the soft condensed matter systems. The length scale covered for such techniques is from around 1-300 nm, as is shown in Figure 2.3. The focus is on the equilibrium structure(s) of a material, and therefore there is no interest in the system dynamics, meaning that exclusively elastic scattering techniques may be used, where there is no energy transfer between the probing radiation and the material. This is in contrast to inelastic scattering where energy transfer occurs; facilitating the measurement of system dynamics, such as the dynamical modes of

²¹ Generally abbreviated to SAS; with SAXS indicating the use of X-rays and SANS neutrons

²² V. Garcia Sakai *et al.* *Curr. Opin. Colloid Interface Sci.* 14.6 (2009), pp. 381–390; B. Farago. *Curr. Opin. Colloid Interface Sci.* 14.6 (2009), pp. 391–395.

²³ See Section ??.

²⁴ Not just X-rays and neutrons, but any wave.

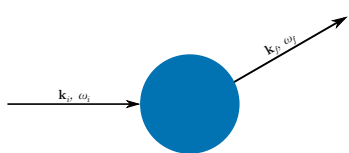


Figure 2.4: A schematic of the scattering of some probing radiation by a sample (blue circle). Adapted, with permission of Oxford University Press, from Sivia, *Elementary Scattering Theory: For X-Ray and Neutron Users*, op. cit.

²⁵ Throughout this work, units of Å⁻¹ will be wherever possible.

polymers and phospholipid bilayers²²

Both X-ray and neutron scattering techniques are discussed and used in this work. From an experimental viewpoint, there are significant differences between an X-ray scattering and a neutron scattering experiment. However, there is little variation in terms of the data analysis, where the differences are limited to; the nature of the scattering lengths²³ and the higher background that is present in the neutron scattering experiments.

2.2.1 The scattering vector

The scattering of some probing radiation,²⁴ by some sample, can be represented as shown in Figure 2.4. Since only elastic scattering is being considered, there will be no change in the frequency of the radiation, $\omega_i = \omega_f$. This means that only the wavevector, \mathbf{k} , can change, $\mathbf{k}_i \neq \mathbf{k}_f$. The difference between the incident and final wavevectors is the scattering vector, \mathbf{q} , where,

$$\mathbf{q} = \mathbf{k}_i - \mathbf{k}_f. \quad (2.5)$$

The scattering vector strictly has units of m⁻¹, however it is often more practical to use nm⁻¹ or Å⁻¹.²⁵ Since the frequency of the probing radiation does not change during an elastic scattering event, the wavelength, λ , will also not change, meaning that the moduli of the incident and final wavevectors are,

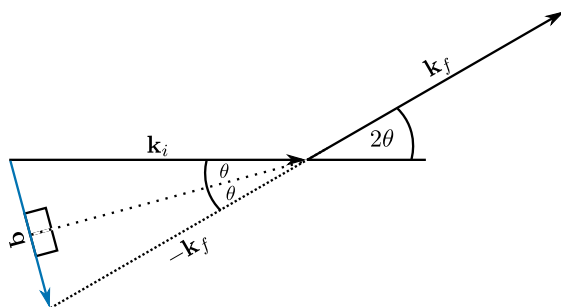
$$|\mathbf{k}_i| = |\mathbf{k}_f| = \frac{2\pi}{\lambda}. \quad (2.6)$$

This also means that only the angle will change during the elastic scattering event. The vector diagram in Figure 2.5 can be used to describe the geometry of an elastic scattering event. From this, and Equation 2.6, the value of q , where $q = |\mathbf{q}|$ can be shown as,

$$q = \frac{4\pi \sin \theta}{\lambda}. \quad (2.7)$$

However, this fails to fully capture the three dimensional nature

Figure 2.5: A vector diagram describing an elastic scattering event, where \mathbf{k}_i is the incident wavevector, \mathbf{k}_f is the final wavevector, 2θ is the scattering angle, and \mathbf{q} is the scattering vector. Adapted, with permission of Oxford University Press, from D. S. Sivia. *Elementary Scattering Theory: For X-Ray and Neutron Users*. 2011.



of the scattering event. Hence, it is necessary to describe the scattering with spherical coordinates, 2θ , and ϕ , such that the incoming

and outgoing radiation can be described as,

$$\begin{aligned}\mathbf{k}_i &= \left(0, 0, \frac{2\pi}{\lambda}\right), \\ \mathbf{k}_f &= \frac{2\pi}{\lambda}(\sin 2\theta \cos \phi, \sin 2\theta \sin \phi, \cos 2\theta),\end{aligned}\quad (2.8)$$

where, $|\mathbf{k}_f| = 2\pi/\lambda$. This allows the scattering vector to be written,

$$\mathbf{q} = \frac{4\pi \sin \theta}{\lambda}(-\cos \theta \cos \phi, -\cos \theta \sin \phi, \sin \theta). \quad (2.9)$$

For an isotropic scattering pattern, it is the magnitude of the scattering vector, q , that is measured. In practical terms, the scattering vector allows for easy comparison of measurements made at different radiation wavelengths.

The basic quantity measured in a scattering experiment is the differential cross section, $d\sigma(q)/d\Omega$. This is the fraction of particles of probing radiation that is scattered with a particular set of polar coordinates, 2θ and ϕ ,

$$\frac{d\sigma(q)}{d\Omega} = \frac{R_i(2\theta, \phi)}{NV\Phi\Delta\Omega}, \quad (2.10)$$

where, $R_i(2\theta, \phi)$ is the rate of arrival of the scattered particles at the position $2\theta, \phi$, V is the illuminated volume of the sample, Φ is incident flux, $\Delta\Omega$ is some small solid angle, and N is the number of scattering particles of interest, in the case of elastically scattered radiation, $N = N\%_{el}$, where $\%_{el}$ is the fraction of elastically scattered radiation.

2.2.2 Scattering from a single fixed particle

It is possible to describe a steady stream X-ray photons or neutrons of wavelength, λ , travelling through space as follows,

$$\psi_i = \psi_o \exp(i\mathbf{k}z), \quad (2.11)$$

where, z is the direction of travel, and the incident flux is the magnitude of the wave squared, $\Phi = |\psi_o|^2$. This wave then interacts with a single fixed particle elastically, propagating the wave radially outwards, as shown in Figure 2.6. This propagation is centred on the atom, therefore the wavevector, \mathbf{k}_f is parallel to the displacement vector, \mathbf{r} , and the following holds,

$$\exp(i\mathbf{k}_f \cdot \mathbf{r}) = \exp(ikr). \quad (2.12)$$

This final wave is no longer collimated and therefore diminishes with distance, r . Hence the final scattered wave has the form,

$$\psi_f = \psi_o b \frac{\exp(ikr)}{r}, \quad (2.13)$$

where, b is the scattering length discussed in Section ??.

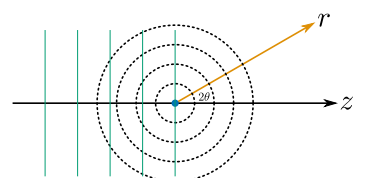


Figure 2.6: A schematic showing the propagation of the wave of probing radiation (green lines) radially outwards following the scattering event, where r is the magnitude of the displacement vector. Adapted, with permission of Oxford University Press, from ibid.

2.2.3 Scattering from multiple particles

It is important to consider how the probing radiation would interact with a real system, consisting of many particles. If the incident beam has the form of Equation 2.11, with the wavevector $\mathbf{k}_i = (0, 0, k)$, each particle, j , will contribute the following to the total scattered wave, ψ_f , made up of the scattering from all, N , atoms,

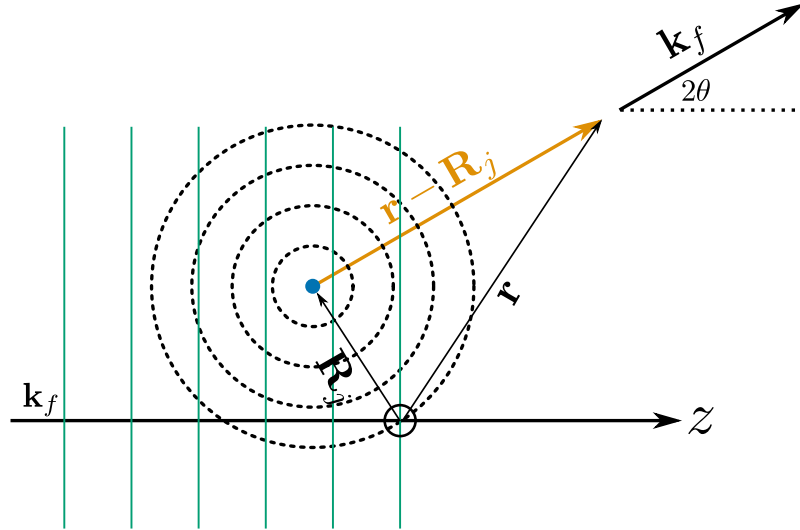
$$[\delta\psi_f]_j = \psi_o \exp(i\mathbf{k}_i \cdot \mathbf{R}_j) b_j \frac{\exp\{i\mathbf{k}_f \cdot (\mathbf{r} - \mathbf{R}_j)\}}{|\mathbf{r} - \mathbf{R}_j|}, \quad (2.14)$$

where, \mathbf{R}_j is the position of particle j , \mathbf{r} is some arbitrary position, and \mathbf{k}_f is the wavevector of the scattered wave, described graphically in Figure 2.7. This allows the total scattered wave to be defined as a summation of the contributions from the individual waves,

$$\psi_f = \psi_o \exp(i\mathbf{k}_f \cdot \mathbf{r}) \sum_{j=1}^N \left\{ b_j \frac{\exp(i\mathbf{q} \cdot \mathbf{R}_j)}{|\mathbf{r} - \mathbf{R}_j|} \right\}. \quad (2.15)$$

Equation 2.15 holds true, within the Born approximation, where the scattered wave has no impact on the incident wave and each wave is scattered only once.

Figure 2.7: A schematic showing the interaction of radiation scattered by two particles that are separated by the vector \mathbf{R}_j . Adapted, with permission of Oxford University Press, from D. S. Sivia. *Elementary Scattering Theory: For X-Ray and Neutron Users*. 2011.



The sample-detector distance is usually much larger than the typical particle size, allowing for the following approximation,

$$|\mathbf{r} - \mathbf{R}_j| = |\mathbf{r}| = r. \quad (2.16)$$

This is termed the Fraunhofer, or far-field limit, and allows Equation 2.15 to be simplified,

$$|\psi_f|^2 = \frac{\Phi}{r^2} \left| \sum_{j=1}^N b_j \exp(i\mathbf{q} \cdot \mathbf{R}_j) \right|^2. \quad (2.17)$$

In the scattering experiment, radiation is deflected elastically into a detector with a small area, δA , at the polar coordinates, 2θ and ϕ , at a rate of R_{el} ,

$$R_{\text{el}}(2\theta, \phi) = |\psi_f|^2 \delta A = \Phi \delta \Omega \left| \sum_{j=1}^N b_j \exp(\mathbf{i}\mathbf{q} \cdot \mathbf{R}_j) \right|^2, \quad (2.18)$$

where, $\delta \Omega = \delta A / r^2$. Therefore, the differential cross section, defined in Equation 2.10 can be related to the scattering from the sample as,

$$\left(\frac{d\sigma(q)}{d\Omega} \right)_{\text{el}} = \frac{1}{V} \left| \sum_{j=1}^N b_j \exp(\mathbf{i}\mathbf{q} \cdot \mathbf{R}_j) \right|^2. \quad (2.19)$$

2.2.4 Scattering length density

While it may be helpful to consider the scattering from multiple particles individually, where each particle has a scattering length, b . In practice, due to low experimental resolution at small angles, it is more common to consider the scattering length density,²⁶ of the system,

$$\text{SLD} = \frac{1}{V} \sum_{i=0}^N b_i, \quad (2.20)$$

where N is the total number of particles in the volume V . A result of this equation is the ability to rewrite Equation 2.19 as,

$$\left(\frac{d\sigma(q)}{d\Omega} \right)_{\text{el}} = \frac{1}{V} \left| \iiint_V \text{SLD} \exp(\mathbf{i}\mathbf{q} \cdot \mathbf{R}) d^3\mathbf{R} \right|^2. \quad (2.21)$$

This equation shows that the scattering differential cross-section from some object is related to the scattering length density profile of that object by a Fourier transform.

2.2.5 Model-dependent analysis

All types of scattering patterns can be analysed by two methods; model independent and model-dependent. The nature of this work means that it will focus on model-dependent analysis methods.²⁷ Model-dependent analysis has significant benefits over model-independent methods, such as improved resolution and more detailed information about the structure. However, the necessity of the inclusion of *a priori* information within model-dependent analysis may act to bias the result. While this is undesirable, these assumptions can, and should, be educated based on the chemical information present.²⁸

The scattering from the model system is determined, using technique specific methods that are discussed in detail in later sections. This is then compared with the experimental data using some figure of merit, the model is then varied to find the best possible model for the data provided.²⁹ In order to accurately reproduce

²⁶ Abbreviated to SLD.

²⁷ With the model usually being derived from some atomistic, or coarse-grained simulation.

²⁸ A. R. McCluskey *et al.* *Curr. Org. Chem.* 22.8 (2018), pp. 750–757, such as the propensity for twin-tailed phospholipid molecules to form monolayers at an air-water interface or small surfactants to form micelles in solution.

²⁹ This typically uses some optimisation algorithm to determine the best solution, the particular algorithms used in this work are discussed in Section 2.4.

³⁰ A. R. J. Nelson *et al.* *J. Appl. Crystallogr.* 46.5 (2013), pp. 1338–1346; A. R. J. Nelson. *J. Appl. Crystallogr.* 47.3 (2014), p. 1162.

the experimental measurement, it is necessary to include some instrumental resolution function, $res(q)$, in the modelling procedure. This is instrument-specific, although it may be approximated by convolving the experimental dataset with some Gaussian smearing function, the modelled intensity can then be determined from,³⁰

$$I(q) = res(q) * \frac{d\sigma(q)}{d\Omega}, \quad (2.22)$$

where, $d\sigma(q)/d\Omega$ is the differential cross-section, a measure of the number of scattering particles hitting a given solid angle of the detector.

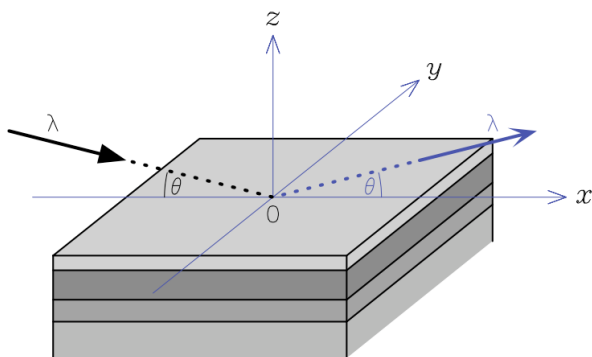
The aim of model-dependent analysis is to obtain a model for the system which agrees well with the experimentally measured scattering data while producing something that is chemically and physically relevant.

2.2.6 Reflectometry

Reflectometry involves the interaction of the probing radiation with some interface, from which the radiation is reflected. The geometry of a reflectometry experiment is shown in Figure 2.8, where the reflectometry instrument is in the horizontal configuration, ideal for the study of liquid interfaces.³¹ Reflectometry measurements give information about the structure perpendicular to the interface, the z -dimension in Figure 2.8, and therefore the analysis of reflectometry data is founded on the assumption that the layers will be completely homogenous in the plane of the interface, the xy -plane in Figure 2.8. In reality, since the layers are usually not completely homogeneous, an average is obtained for the area in the radiation beam.

³¹ Such as those investigated in Chapters 3 and 4.

Figure 2.8: A schematic showing the geometry of a typical specular reflectometry experiment from a layered sample. Reprinted, with permission of Oxford University Press, from D. S. Sivia. *Elementary Scattering Theory: For X-Ray and Neutron Users*. 2011.



A reflectometry instrument operates by measuring the intensity of specular radiation at a series of different angles, θ , or wavelengths, λ . The reflected intensity is described in terms of the q -vector³², and is defined as follows,

$$R(q) = \frac{\text{specular reflected radiation intensity at } q}{\text{incident radiation intensity}}. \quad (2.23)$$

³² Using Equation 2.7

It is clear from Equation 2.23 that the value of the measured reflectometry cannot be greater than one, as this would mean that more particles of probing radiation were being reflected than were incident.

There are two model-dependent analysis techniques that can be applied to the understanding of a reflectometry dataset. The first is the kinematic approach, which can be described with Equation 2.19, from the assumption that $q_x = 0$ and $q_y = 0$, as we are only measuring the specular scattering. This approach models the reflectometry as a function of the scattering length density profile in the z -dimension, $\text{SLD}(z)$,

$$R(q) \approx \frac{16\pi^2}{q^4} \left| \int_{-\infty}^{+\infty} \frac{d\text{SLD}(z)}{dz} \exp(-izq_z) dz \right|^2, \quad (2.24)$$

where, $d\text{SLD}(z)/dz$ is the first derivative of the scattering length density profile. However, this method has a significant problem, which can be demonstrated by applying Equation ?? to the scattering length density profile of a bare silicon substrate, which can be modelled as a Heaviside function, as shown in Figure 2.9(a),

$$\text{SLD}(z) = \begin{cases} 0, & \text{where } z < 0 \\ \text{SLD}_{\text{Si}}, & \text{otherwise} \end{cases} \quad (2.25)$$

where, SLD_{Si} is the scattering length density of pure silicon.³³ The derivative of a stepwise Heaviside function is a scaled δ -function, as shown in Figure 2.9(b),

$$\text{SLD}'(z) = \text{SLD}_{\text{Si}}\delta(z). \quad (2.26)$$

Then, as in Equation ??, the Fourier transform of this δ -function is taken,

$$\text{SLD}_{\text{Si}} \int_{-\infty}^{+\infty} \delta(z) \exp(-izq_z) dz = \text{SLD}_{\text{Si}} \exp(0) = \text{SLD}_{\text{Si}}. \quad (2.27)$$

This means that, using Equations 2.27 and ??, the reflectometry profile could be calculated from the following relationship,

$$R(q) \approx \frac{16\pi^2 \text{SLD}_{\text{Si}}^2}{q_z^4}. \quad (2.28)$$

The curve from this relationship is shown in Figure 2.9, where it is clear that the agreement with an experimental profile would be poor as $q \rightarrow 0$. It can be seen that for low values of q the calculated reflectometry is greater than 1, which violates the physical constraint imposed with Equation 2.23. This breakdown of the kinematic approach is due to the assumption present in this approach that the Born approximation³⁴ will hold. However, in the reflectometry scattering geometry, this is no longer true rendering the kinematic approach invalid.

This breakdown of the kinematic approach has led to the application of the Abelès, or Parratt, model for the reflection of light

³³ This is $2.1 \times 10^{-6} \text{ \AA}^{-2}$ for neutrons.

³⁴ Mentioned previously in Section 2.2.3.

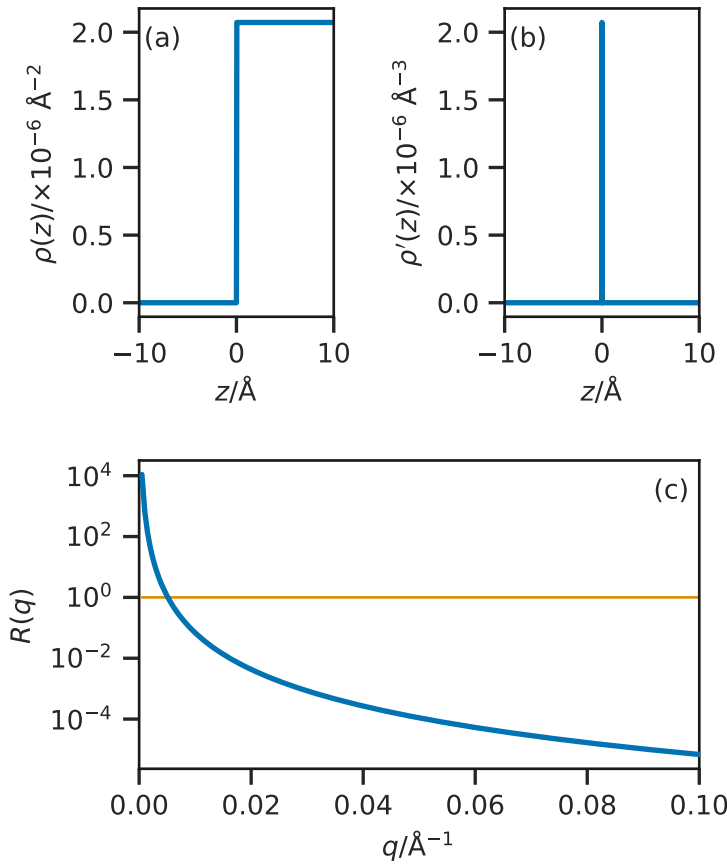


Figure 2.9: A graphical representation of the kinematic approach; (a) the Heaviside function describing the scattering length density profile of a bare silicon substrate, (b) the δ -function arising from the first derivative of the function in (a), and (c) the reflectometry profile resulting from the kinematic approach, where the orange line at $R = 1$ identifies the break down between experimental and theory in the kinematic approach. Adapted, with permission of Oxford University Press, from D. S. Sivia. *Elementary Scattering Theory: For X-Ray and Neutron Users*. 2011.

at a given number of stratified interfaces.³⁵ This method involves considering the system as a layered structure at the interfaces of which, the probing radiation can either be reflected or refracted, by some refractive index, n_i . Figure 2.10 shows this process for a system of two layers, where the layer 0 is the air or vacuum above the sample, it is clear to see how the two waves labelled r could interfere constructively or destructively depending on the thickness of layer 1, d . This means that for a single interface,³⁶ the reflectometry can be described by the Fresnel equation,

$$R(q) = \left| \frac{n_0 \sin \theta_0 - n_1 \sin \theta_1}{n_0 \sin \theta_0 + n_1 \sin \theta_1} \right|^2. \quad (2.29)$$

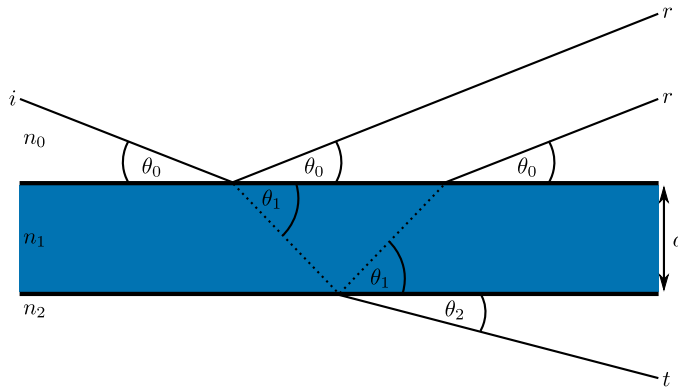
Additionally at the point of total reflection, where $\theta_0 = \theta_c$, the critical angle, there will be no transmitted wave so,

$$n_1 \sin \theta_1 = 0, \quad (2.30)$$

and therefore the reflected radiation will never be greater than 1, while the critical angle can be defined as,

$$\cos^2 \theta_c = \frac{n_1^2}{n_0^2}. \quad (2.31)$$

This is the angle below which a reflectometry profile will be measured.



³⁵ F. Abelès. *Ann. Phys.* 12.3 (1948), pp. 504–520; L. G. Parratt. *Phys. Rev.* 95.2 (1954), pp. 359–369, also known as dynamical theory.

³⁶ Such as that between layers 0 and 1 in Figure 2.10.

Figure 2.10: A schematic diagram showing the reflected (r) and transmitted (t) waves when an incident (i) wave enters an interface of thickness d , where the refractive indices of each layer are n_0 , n_1 , and n_2 . Adapted, with permission of Elsevier, from F. Foglia et al. *Curr. Opin. Colloid Interface Sci.* 20.4 (2015), pp. 235–243.

The above method can then be generalised to a structure of an arbitrary number of layers, as shown in Code Block 2.1.³⁷ For each value of q for which the reflectometry is to be calculated, the system is considered in terms of n_{\max} layers. The incident radiation beam will be refracted by each of the layers, giving wavevectors values for each layer, k_n ,

$$k_n = \sqrt{k_0^2 + 4\pi(\text{SLD}_n - \text{SLD}_0)}, \quad (2.32)$$

where, $k_0 = q/2$. The Fresnel equation coefficient between layers n and $n+1$, $r_{n,n+1}$ can then be found along with the phase factor, β_n , which is dependent on the thickness of the layer, d_n ,

$$r_{n,n+1} = \frac{k_n - k_{n+1}}{k_n + k_{n+1}}, \quad (2.33)$$

³⁷ The purpose of the Code Blocks throughout this work is to ensure transparency and reproducibility, these are written as Python functions.

$$\beta_n = k_n d_n. \quad (2.34)$$

The means that a matrix can be evaluated for each layer, M_n ,

$$M_n = \begin{bmatrix} \exp \beta_n & r_{n,n+1} \exp -\beta_n \\ r_{n,n+1} \exp \beta_n & \exp -\beta_n \end{bmatrix} \quad (2.35)$$

The resultant matrix, B , is then found as a product of the matrix from each layer,

$$B = \prod_{n=0}^{n_{\max}} M_n, \quad (2.36)$$

and from this the reflected intensity at the given value of q can be found,

$$R(q_z) = \frac{B_{1,2}}{B_{1,1}}. \quad (2.37)$$

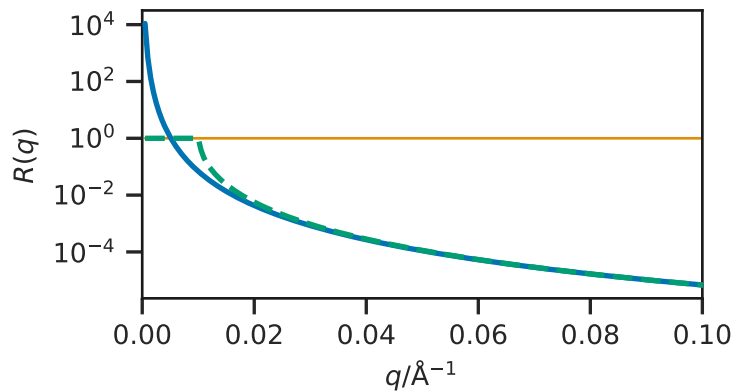
³⁸ Particularly for soft matter systems.

This algorithm models the layers as perfectly flat layers, which will not be strictly true.³⁸ This resulted in the correction term being added to Equation 2.33 to account for the roughness of the layers. This adapts Equation 2.33 to the form,

$$r_{n,n+1} = \frac{k_n - k_{n+1}}{k_n + k_{n+1}} \exp (-2k_n k_{n+1} \sigma_{n,n+1}^2), \quad (2.38)$$

³⁹ L. Nérot *et al.* *Rev. Phys. Appl. (Paris)* 15.3 (1980), pp. 761–779.
⁴⁰ That is given programmatically in Code Block 2.1.
⁴¹ Nelson *et al.*, “Refnx: Neutron and X-Ray Reflectometry Analysis in Python”, op. cit.; A. R. J. Nelson. *J. Appl. Crystallogr.* 39.2 (2006), pp. 273–276; A. V. Hughes. *RasCAL*. URL: <https://sourceforge.net/projects/rscl/> (Accessed 2016-09-14).
⁴² Y. Gerelli, *J. Appl. Crystallogr.* 49 (2016) 230–239; Y. Gerelli, J. Andò, *Crystallogr. Applic.* 46.2 (2016) 712–718 (dashed line), to determine the reflected intensity from the material with the scattering length density profile given in Figure 2.9(a). It is clear that at low q , there is a noticeable deviation between the two.

where, $\sigma_{n,n+1}$ is the interfacial roughness between layers n and $n + 1$.³⁹ This has the effect of Gaussian broadening the layers into each other, as a result. This method⁴⁰ is currently implemented in a variety of reflectometry modelling software packages, such as `refnx`, `MOTOFIT`, `RasCAL`, and `Aurore`.⁴¹ Applying this method to the scattering length density profile shown in Figure 2.9 gives the reflectometry profile shown with the dashed green line in Figure 2.11.



Code Block 2.1: An example Python code block for the Abelès method for the calculation of reflectometry, adapted from A. R. J. Nelson *et al.* *J. Appl. Crystallogr.* 52.1 (2019), pp. 193–200.

The input variables are `q_values` which are the q -vectors at which the reflected intensity should be calculated, `sld` which is the array of scattering length densities for the layers, and `d` which is the array of thicknesses for the layers. This will return an array of floats that is the same size as the `q_values` and contains the reflected intensities.

```
# Copyright 2015-2019 A. R. J. Nelson
# Australian Nuclear Science and Technology Organisation
# Licensed under the BSD 3-Clause "New" or "Revised" License

import numpy as np

def abeles(q_values, sld, d):
    R = np.zeros_like(q_values)
    kn = np.sqrt(
        q_values[:, np.newaxis] ** 2.0 / 4.0 - 4.0 * np.pi * sld
    )
    B = np.zeros((2, 2, q_values.size))
    B[0, 0, :] = 1
    B[1, 1, :] = 1
    k = kn[:, 0]
    nmax = sld.size
    for n in range(1, nmax):
        kn1 = kn[:, n]
        r = (k - kn1) / (k + kn1)
        betan = k * d[n]
        if n > 0:
            Mn = np.array([
                [np.exp(betan * 1j), r * np.exp(betan * 1j)],
                [r * np.exp(-betan * 1j), np.exp(-betan * 1j)]
            ])
        else:
            Mn = np.array([[1, r], [r, 1]])
        p0 = B[0, 0, :] * Mn[0, 0, :] + B[1, 0, :] * Mn[0, 1, :]
        p1 = B[0, 0, :] * Mn[1, 0, :] + B[1, 0, :] * Mn[1, 1, :]
        B[0, 0, :] = p0
        B[1, 0, :] = p1
        p0 = B[0, 1, :] * Mn[0, 0, :] + B[1, 1, :] * Mn[0, 1, :]
        p1 = B[0, 1, :] * Mn[1, 0, :] + B[1, 1, :] * Mn[1, 1, :]
        B[0, 1, :] = p0
        B[1, 1, :] = p1
        k = kn1
    R = (B[0, 1, :] * np.conj(B[0, 1, :])) / (
        B[0, 0, :] * np.conj(B[0, 0, :])
    )
    R[np.where(np.isnan(R))] = 1.0
    return np.real(R)
```

2.2.7 Small angle scattering

Equation 2.21 identified that the scattering differential cross-section for some object was related to the SLD by a Fourier transform, which is shown graphically in Figure 2.12. This figure shows that there is a reciprocal relationship between the size of the object and the scattered intensity, decaying significantly up to values of $2\pi/d_x$, where d_x is the size of the object. This means that in order to probe large-scale structural features that are of interest in the study of soft materials, it is necessary to consider small values of q . When considering the nature of q in Equation 2.7, it is clear that such experiments would benefit from small values of θ and large values of λ . Hence, the use of scattering at small angles.

A SAS experiment generally involves some sample being placed in the path of the probing radiation; the scattering pattern that results from this transmission is measured at some distance, as is shown in Figure 2.13 for the D22 SANS instrument of the ILL. SAS instruments are usually very large, due to the large post sample flight path that is necessary to reach the small angles being measured.⁴² Transmission SAS can provide information about the size, shape and orientation of the sample's components.⁴³ The range of q that is typically covered by a SAS instrument is usually around 2×10^{-3} – 0.5 \AA^{-1} , which corresponds to 10–3000 \AA in real-space. The neutron or X-ray detector of a SAS instrument is often two-dimensional, meaning that for an isotropic scattering profile, the detector image is radially averaged to give an $I(q)$ scattering profile. It is possible to increase the q -range of a SAS instrument

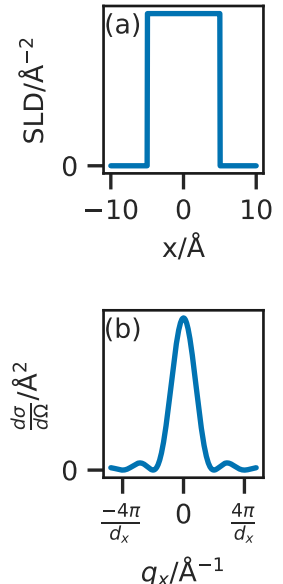


Figure 2.12: The effect of a Fourier transform (a) the scattering length density profile for some object with a width of 10 \AA , (b) the Fourier transform of this object showing the minima in the differential cross section at values of $2n\pi/10$, where n is some integer.

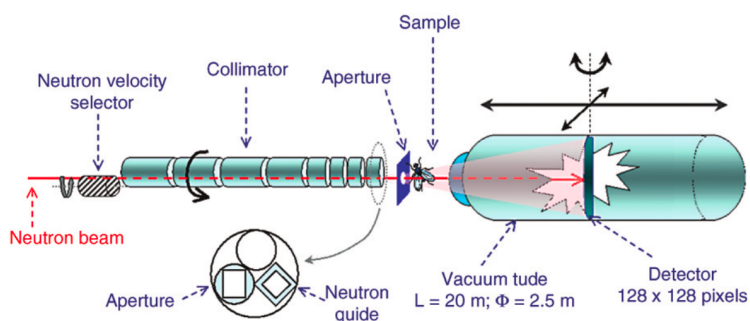
⁴² A longer flight path allows more space for angular divergence.

⁴³ B. T. M. Willis *et al.* *Experimental Neutron Scattering*. 2009.

⁴⁴ ISIS – SANS2D. URL: <https://www.isis.stfc.ac.uk/Pages/Sans2d.aspx> (Accessed 2018-9-25).

Figure 2.13: A schematic of the D22 instrument of the ILL. Reprinted with permission of Springer Nature Customer Service Centre GmbH: Springer Nature from I. Grillo. "Small-Angle Neutron Scattering and Applications in Soft Condensed Matter". In: *Soft-Matter Characterization*. 2008, pp. 723–782.

through the introduction of wide- q detector banks close to the sample or small- q detector banks further away. This allows the SANS2D instrument, at the ISIS Neutron and Muon Source, to have a total range from 2×10^{-3} - 2 \AA^{-1} .⁴⁴ Furthermore, the SANS2D instrument may leverage the ToF method discussed in Section 2.1.2 to allow for a much shorter post sample flight path than is present at D22.



⁴⁵ K. J. Edler et al. *Curr. Opin. Colloid Interface Sci.* 20.4 (2015), pp. 227–234.

A radially averaged SAS pattern can be considered as consisting of two sections that arise from the form and structure factors for the scattering species. The form factor gives information about the average shape of the scattering particle, while the structure factor is a measure of the interaction present between the objects. It is often possible to control the presence of the structure factor by changing the concentration of the sample, eventually, the concentration will be so low that all interparticle interaction is screened by the solvent.⁴⁵ This method is frequently applied in biological SAXS applications, where the interactions between the protein molecules are of less interest than the overall structure of the complex. However, with micelles, it is not always possible to remove the structure factor, as the critical micelle concentration may be higher than the minimum concentration at which the structure factor is present. It is possible to deconvolute the structure and form factors for a micellar solution by studying different concentrations, assuming that the form of the micelle is concentration independent, over the measured concentration range.

The rigorous, model-independent method for the analysis of SAS involves taking the inverse Fourier transform of the scattering profile, to give an auto-correlation function of the average particle in the system, which following a deconvolution procedure will resolve the radially averaged SLD profile. However, this is often cumbersome and has a low information density, when compared to model-dependent techniques. Additionally, if the experimental data lacks information at wide enough q to cover all features of the sample, artefacts may be present in the inverse Fourier transform of the scattering.

There are two common and straight-forward analysis proce-

dures that can be used to give an understanding of the scattering species structure. The first is the Guinier approximation, which is used in the determination of the radius of gyration, R_g , of the scattering species at “infinite dilution”. This scattering law is only valid at very small values of q , where $q < R_g^{-1}$,⁴⁶

$$\ln[I(q)] = \ln[I(0)] - \left(\frac{R_g^2}{3}\right)q^2. \quad (2.39)$$

This relationship allows the radius of gyration to be found by plotting the scattering profile transformed into $\ln[I(q)]$ vs. q^2 , and evaluating the gradient at low q . The Guinier plot for the scattering from a sphere with a radius of 20 Å is shown in Figure 2.14, where the radius of gyration correlates with the radius of the sphere, R_s , as follows,

$$R_g = \sqrt{\frac{3}{5}} R_s. \quad (2.40)$$

The Guinier analysis is very common in the study of proteins by SAS, as it allows for the determination of the protein size in the native, solution phase.⁴⁷ Another common analysis of SAS data comes in the form of Porod’s law, which states that for large values of q , the scattering intensity becomes proportional to Sq^{-4} , where S is the surface area of the sample. This means that by plotting $I(q)q^4$ vs. q and extrapolating to $q \rightarrow \infty$, it is possible to determine the external surface area of the system.⁴⁸ Using the surface area, it is then possible to qualitatively determine the “roughness” of the system based on the relation of the surface area to the particle size.

⁴⁶ Sivia, *Elementary Scattering Theory: For X-Ray and Neutron Users*, op. cit.

⁴⁷ S. Skou et al. *Nat. Protoc.* 9.7 (2014), pp. 1727–1739.

⁴⁸ Willis et al., *Experimental Neutron Scattering*, op. cit.

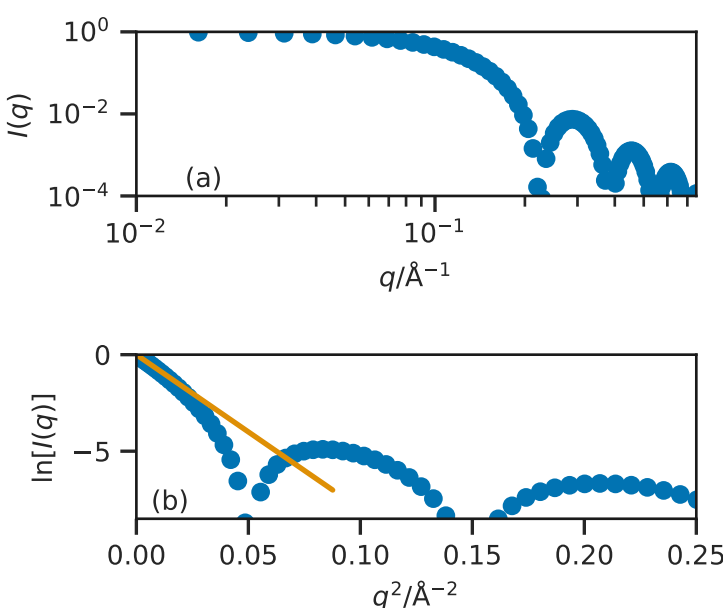


Figure 2.14: The Guinier plot, (a) the ideal scattering profile from a sphere of radius 20 Å, (b) the associated Guinier plot, with a straight line (orange) at low- q showing the radius of gyration to be ~ 15.5 Å.

In the calculation of a SAS pattern, both the structure and form factors will contribute. Therefore, when we model the pattern, the

⁴⁹ When the system is centrosymmetric, the differential cross-section has the following form.⁴⁹

$$\frac{d\sigma(q)}{d\Omega} = N_p \Delta SLD^2 V_p^2 P(q) S(q), \quad (2.41)$$

where N_p is the number density of the particles, ΔSLD is the difference in scattering length density between the particles and the solvent, V_p is the particle volume, $P(q)$ is the particle form factor and $S(q)$ is the structure factor.

2.3 CLASSICAL SIMULATION

While the currently applied traditional methods for the analysis of experimental scattering data discussed previously are popular. There is growing interest in the use of multi-modal analysis methods that leverage classical simulation to assist in the analysis of scattering data.⁵⁰ This would involve the simulation of the chemical system in order to educate the analysis of the experimental data. These systems, especially when the materials being simulated are soft in nature, are often highly complex and typically cover large length scales. Classical simulation, particularly in combination with coarse-grained potential models, can feasibly enable the simulation of these methods.

In order to simulate a complexity of a real chemical system, it is necessary to model the electrons of the molecules and their interactions. This is usually achieved using quantum mechanical calculations, where the energy of the system is calculated by finding some approximate solution to the Schrödinger equation. However, quantum mechanical calculations are very computationally expensive and are realistically limited to hundreds of atoms. In order to simulate a soft matter system such as a phospholipid monolayer or polymer nanoparticles, it is necessary to simplify the calculation being performed. This leads to the use of classical simulations, where parameterised analytical functions are used to represent the potential energy of the system. Classical simulations are used substantially in this work, in terms of molecular dynamics simulations.⁵¹ Therefore, it is necessary to introduce the underlying theory on which this method is defined.

2.3.1 Potential models

Potential modelling is a more computationally efficient method for the calculation of the potential energy of a chemical system. A potential model consists of a series of mathematical functions that depend on the atomic positions, \mathbf{r} . Each of the functions represents the potential energy of a different interaction for a given atom. Broadly, these interactions can be split into bonded and non-bonded, such that the total energy may be described as follows,

⁵⁰ Ivanović *et al.*, "Temperature-Dependent Atomic Models of Detergent Micelles Refined against Small-Angle X-Ray Scattering Data", *op. cit.*; Scoppola *et al.*, "Combining Scattering and Computer Simulation for the Study of Biomolecular Soft Interfaces", *op. cit.*; Dabkowska *et al.*, "Modulation of Dipalmitoylphosphatidylcholine Monolayers by Dimethyl Sulfoxide", *op. cit.*; J. S. Hub. *Curr. Opin. Struct. Biol.* 49 (2018), pp. 18–26.

⁵¹ Molecular dynamics (MD) is discussed in detail in Section 2.4.

$$E_{\text{total}}(r) = \sum_{\text{bonded pairs}} E_{\text{bonded}}(r) + \sum_{\text{atom pairs}} E_{\text{non-bonded}}(r). \quad (2.42)$$

The total potential energy is then the sum of the potential energy for each of the individual atoms.

The bonded terms are used to describe different aspects of chemical bonds. These typically consist of bond stretches, angle bends and dihedral torsions, these interactions have the following mathematical form,⁵²

$$\begin{aligned} E_{\text{bonded}}(b, \theta, \phi) = & \sum_{\text{bonds}} K_b(b - b_0)^2 + \sum_{\text{angles}} K_\theta(\theta - \theta_0)^2 \\ & + \sum_{\text{dihedrals}} \frac{1}{2} \{ A_1 [1 + \cos(\phi)] \\ & + A_2 [1 - \cos(2\phi)] + A_3 [1 + \cos(3\phi)] \}, \end{aligned} \quad (2.43)$$

where, K_b and b_0 , K_θ , θ_0 , and A_1 , A_2 , and A_3 are interaction dependent parameters for the bonds, angles, and dihedrals respectively, while b , θ , and ϕ are the bond lengths, the size of the angles, and the size of the dihedrals that depend on the atom positions.⁵³ It can be seen that both the bond stretch and angle bend have harmonic functions, whereas the dihedral consists of a more complex multiple cosine functions.

The non-bonded terms are a series of functions that describe the potential energy of intermolecular interactions, such as electrostatics and London dispersion forces. The potential energies of the short-range interactions are usually modelled as a combination of the attractive London dispersion interaction and the repulsive exchange forces that arise from the Pauli exclusions principle.⁵⁴ These are often forms such as shown below for the Lennard-Jones potential model,⁵⁵

$$\begin{aligned} E_{\text{non-bonded}}(r) = & E_{\text{repulsive}} + E_{\text{attractive}} \\ = & \frac{A}{r^{12}} - \frac{B}{r^6} = 4\epsilon \left[\left(\frac{\sigma}{r} \right)^{12} - \left(\frac{\sigma}{r} \right)^6 \right] \end{aligned} \quad (2.44)$$

where, r is the distance between two particles, A and B are interaction dependent parameters, and σ and ϵ are simple reformations of these parameters,

$$A = 4\epsilon\sigma^{12} \quad B = 4\epsilon\sigma^6. \quad (2.45)$$

Figure 2.15 shows each component of the Lennard-Jones potential model for atoms of argon.⁵⁶ The Lennard-Jones potential model is not the only form that may be used for the modelling of the short-range non-bonded interactions, others such as the Buckingham and Morse potentials exist.⁵⁷ In each case, there is a short ranged repulsive interaction to describe the electrostatic repulsion between

⁵² These forms are specific to the OPLS2005 potential model (J. L. Banks *et al.* *J. Comput. Chem.* 26.16 (2005), pp. 1752–1780), other potential models may have different functions.

⁵³ The values for the interaction dependent parameters are determined as outlined in Section 2.3.2.

⁵⁴ A. R. Leach. *Molecular Modelling: Principles and Applications*. 1996.

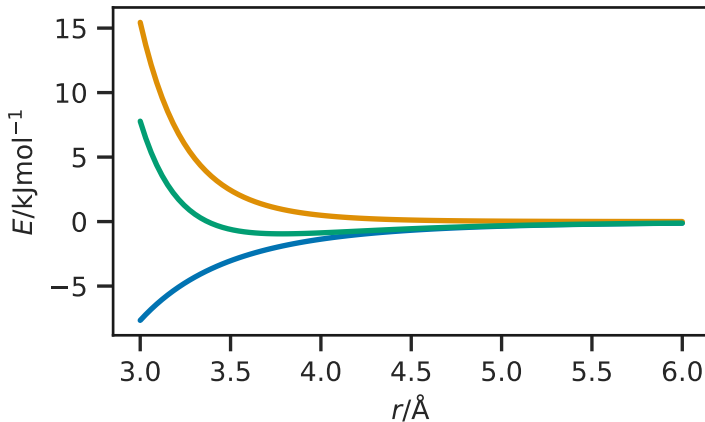
⁵⁵ J. E. Lennard-Jones. *Proc. Royal Soc. Lond. A.* 106.738 (1924), pp. 463–477.

⁵⁶ Using parameters for A and B determined in A. Rahman. *Phys. Rev.* 136 (2A 1964), A405–A411.

⁵⁷ R. A. Buckingham. *Proc. Royal Soc. Lond. A.* 168.933 (1938), pp. 264–283; P. M. Morse. *Phys. Rev.* 34.1 (1929), pp. 57–64.

the electron clouds, and a longer range attractive component that represents dispersion interactions. However, the Lennard-Jones model has been used heavily in this work.

Figure 2.15: The form of each component; attractive (blue), repulsive (orange), of the Lennard-Jones potential model (green) for argon, using parameters in A. Rahman. *Phys. Rev.* 136 (2A 1964), A405–A411.



While the short-range interactions can be accounted for by a function such as the Lennard-Jones potential model, the potential energy of the long-range electrostatic interactions are usually modelled, more consistently, using Coulomb's law for classical electrostatic interaction between point particles,⁵⁸

$$E_{\text{Coulomb}}(r) = \frac{1}{4\pi\epsilon_0} \frac{q_i q_j e^2}{r^2}, \quad (2.46)$$

where, r is the distance between the two particles, ϵ_0 is the dielectric permittivity of the vacuum, e is the charge of the electron, and q_i and q_j are the electronic charges on each of the particles. It is clear that when q_i and q_j have the opposite signs Coulomb's law is always attractive. The fact that Equation 2.46 contains a factor of r^2 indicates that this is a much longer range interaction than those modeled with the Lennard-Jones model, make the Coulomb potential more complex to compute.⁵⁹

An example of a very large classical simulation would be ~ 3 million atoms.⁶⁰ However, this is still only 1.8×10^{-16} mol which is not remotely realistic as a simulation of a "real" system. A common method to allow for the apparent simulation of a much larger system is the use of periodic boundary conditions.⁶¹ This is where a boundary condition is applied to the edges of the simulation cell, such as to mimic an infinite system, such that the simulation cell is surrounded by identical images of itself, this is shown pictorially in Figure 2.16. Using the PBC means that atomic diffusion is conserved as when an atom reaches the edge of the simulation cell, it will appear on the other side as though it came from the adjacent periodic cell. The use of a periodic boundary condition is particularly powerful in the simulation of homogenous systems, such as

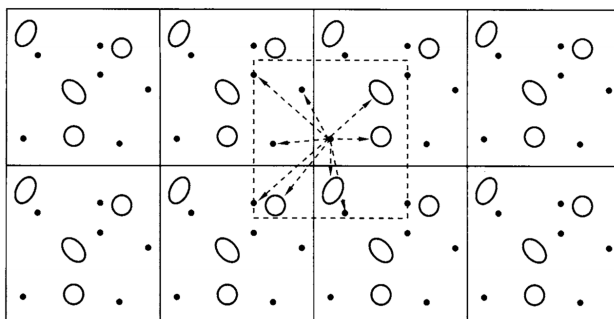
⁵⁸ C. A. Coulomb. *Histoire de l'Académie Royale des Sciences*. Imprimerie Royale (1788), pp. 569–577; C. A. Coulomb. *Histoire de l'Académie Royale des Sciences*. Imprimerie Royale (1788), pp. 578–611.

⁵⁹ D. Frenkel et al. *Understanding Molecular Simulation: From Algorithms to Applications*. 1996.

⁶⁰ J. Gumbart et al. *Structure* 17.11 (2009), pp. 1453–1464.

⁶¹ Abbreviated to PBC.

liquids.



The cut-off is another important factor for classical simulation, this is the distance after which the energy between two particles is considered to be zeros. Therefore, for distances greater than the cut-off, it is not necessary to calculate the energy between the two particles as it is taken to be zero.⁶² Code Block 2.2 gives an example of some code that could be used to calculate the Lennard-Jones energy of an atomistic system, where both the periodic boundary condition and the energy cut-off distance are considered.

```
import numpy as np

def lj_energy(coordinates, cell, cut_off, A, B):
    energy = np.zeros((coordinates.shape[0]))
    for i in range(coordinates.shape[0] - 1):
        for j in range(i + 1, coordinates.shape[0]):
            d = coordinates[j] - coordinates[i]
            d = d % cell
            r = np.sqrt(np.sum(np.square(d)))
            if r > cut_off:
                continue
            else:
                energy[i] += A / np.power(r, 12) - B / np.power(r, 6)
                energy[j] += A / np.power(r, 12) - B / np.power(r, 6)
    return energy
```

The use of the PBC may be problematic for systems containing long-range interactions, such as classical electrostatics, due to the fact that the range of the electrostatic interaction may be much greater than the size of half of the simulation cell, which can be taken to be the energy cut-off distance. In order to avoid truncation artefacts, the Ewald summation is often used for the calculation of the electrostatic contribution to the potential energy.⁶³ The Ewald summation involves performing the summation of the contributing interaction energies in reciprocal space rather than in real space as is the case for the short-range interactions. Most modern molecular dynamics simulation software packages implement the Ewald summation using a particle mesh Ewald (PME) method.⁶⁴

2.3.2 Parameterisation

Section 2.3.1 introduced the idea of potential models that may be used to evaluate the potential energy of a given system, requiring much less time than methods that rely on the use of quantum mechanics. However, for these methods to be effective, it is important

Figure 2.16: A graphical representation of the periodic boundary conditions. Reprinted, with permission of Elsevier, from D. Frenkel *et al. Understanding Molecular Simulation: From Algorithms to Applications*. 1996.

⁶² This leads to an increase in the computational efficiency.

Code Block 2.2: Code that may be used to generate the Lennard-Jones energy for a given atomistic system, which accounts for the periodic boundary condition and the energy cut-off distance. The input variables are `coordinates` which is an array of floats describing the position of the N particles, `cell` which are the unit cell vectors, `cut_off` which is potential energy cut-off, and `A` and `B` which are the Lennard-Jones potential parameters. This returns an array with the energy for each particle.

⁶³ P. P. Ewald. *Ann. Phys.* 369.3 (1921), pp. 253–287.

⁶⁴ U. Essmann *et al. J. Chem. Phys.* 103.19 (1995), pp. 8577–8593.

that the potential models used are able to model the system under study accurately. This is achieved initially by selecting the correct potential model for a given interaction, and then by ensuring that the interaction-dependent parameters are accurate for a given interaction. The method of obtaining such parameters is referred to as “parameterising” the model. Model parameterisation is important for all types of potential models, for example it is necessary to determine the equilibrium bond length b_0 and the force constant K_b for a given covalent bonds, or the partial electrostatic charge that is present on a carbonyl oxygen atom when it interacts with the hydrogen atom from a neighbouring hydroxyl group.

Parameterisation of a potential model is usually achieved by fitting the potential model functions to energetic data obtained using a higher accuracy technique.⁶⁵ We will not dwell on the details of potential model parameterisation,⁶⁶ however, it is important to note that the parameters used in MD simulation are not absolute and depend heavily on the merits of the parameterisation method.

In this work, we have focused heavily on the use of off-the-shelf potential models, to ensure the easy replicability of the work. Off-the-shelf potential models are those that are determined to be applied to a wide range of chemical systems. An example includes the OPLS potential model which was parameterised by comparison to quantum mechanical measurements and crystallographic data.⁶⁷ While these off-the-shelf potential models are useful for their ease-of-use, it is noted that often these forcefields may require optimisation for the particular system.

2.3.3 Coarse-graining

The atomistic simulation of very large systems, such as multiple surfactant micelles or large phospholipid monolayers, require a huge number of atoms. While computational efficiency improvements such as the PBC or the energy cut-off distance are able to reduce the time taken to simulate these systems, it is often still not possible to produce physically meaningful simulations,⁶⁸ without including some other efficiency improvements.

This has led to the use of coarse-graining of molecules in simulations. This is the definition of super-atoms, in the place of groups of atoms, known as “beading”, some examples are shown for the MARTINI force field⁶⁹ in Figure 2.17. Each of the super-atoms must correspond to the chemistry of the underlying atoms. For example the MARTINI potential model, introduces five different apolar, beads to represent the polarity of the carbon atoms that make up the super-atom. Additionally, there are thirteen other super-atom types that can be used to model polar, nonpolar, and charged atomic groups.

In addition to the computational benefit of having fewer particles in the simulation,⁷⁰ there is also the opportunity to increase

⁶⁵ These may be quantum mechanical calculations or experimental methods.

⁶⁶ This is discussed in detail in many textbooks such as J. Harvey. *Computational Chemistry*. 2018; Leach, *Molecular Modelling: Principles and Applications*, op. cit.

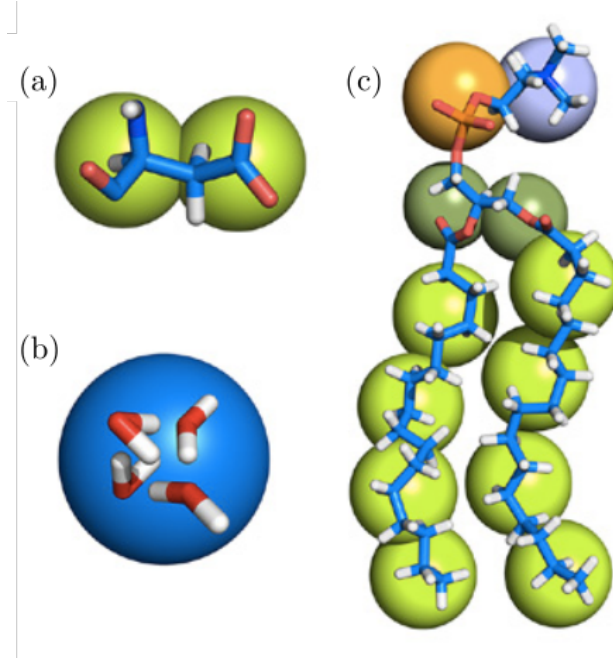
⁶⁷ W. L. Jorgensen *et al.* *J. Am. Chem. Soc.* 110.6 (1988), pp. 1657–1666.

⁶⁸ In particular for emergent properties that depend on large system sizes and long simulation times.

⁶⁹ Marrink *et al.*, “The MARTINI Force Field: Coarse Grained Model for Biomolecular Simulations”, op. cit.

⁷⁰ Therefore requiring fewer integrations of the equations of motion

Figure 2.17: Three examples of the MARTINI coarse-graining mechanism for (a) aspartic acid, (b) a water cluster, and (c) a molecule of DPPC. Reprinted with permission of the Institute of Physics, from K. Pluhackova *et al.* *J. Phys. Condens. Matter* 27.32 (2015), p. 323103.



the timestep length for the simulation.⁷¹ This can be achieved as the highest frequency vibrations that must be modelled in the system are integrated out. For example, another coarse-grained model called the united atom potential model, where the hydrogen atoms have been integrated out, the timestep may be larger than for the same all-atom system as it is no longer necessary to model the high-frequency C–H bond.

The technique of coarse-graining a molecule can range from the integration of the hydrogen atoms into the heavier atoms to which they are bound, all the way to the treatment of entire molecules as a single “bead”, with the inclusion of an implicit solvent. The parameterisation of a coarse-grained potential model is carried out in much the same way as discussed in Section 2.3.2 for all-atom potential models. The coarse-grained parameters are determined by comparison with a higher-resolution technique.⁷²

⁷¹ K. Pluhackova *et al.* *J. Phys. Condens. Matter* 27.32 (2015), p. 323103.

⁷² Often this is all-atom molecular dynamics simulations.

2.4 OPTIMISATION & SAMPLING METHODS

In this work, computational modelling methods have been applied to important scattering problems. The aim of many modelling problems is to optimise a series of parameters such that a minimum in some parameter-dependent metric is found. While, in other circumstances, the aim is to sample the parametric search-space of a particular problem. The problem of parameter optimisation and sampling is a massive area of mathematics and computer science and is it not possible to introduce the whole field. Therefore, I will introduce two optimisation methods and two sampling methods that are applied within this work.

Both optimisation algorithms in this work are population-based,

⁷³ G. Wu *et al.* *Swarm Evol. Comput.* 44 (2019), pp. 695–711.

making use of a population of candidate solutions. These populations of candidate solutions often have knowledge of the state of each other through some interaction method. The interaction method is often used to characterise the algorithms, into evolutionary algorithms and swarm intelligence algorithms.⁷³ These population methods are usually more efficient at finding the global minimum for a given search space, than a single candidate method.

2.4.1 Differential evolution

Differential evolution (DE) is a common, iterative optimisation algorithm, that was first applied to the analysis of reflectometry and diffraction data by Wormington *et al.*⁷⁴ Since then, it has proven very popular for the optimisation of reflectometry data and is included in many common analysis programs.⁷⁵ The DE algorithm is designed to more ably determine the global minimum of a particular function.⁷⁶

DE is an example of a genetic algorithm, one that is designed to mimic the evolution processes observed in biology.⁷⁷ The method consists of two vectors, the parent population, \mathbf{p} , the offspring population, \mathbf{o} . These vectors are of a dimension ($i \times j$), where i is the number of variables being optimised and j is the number of candidate solutions being used. The offspring population vector is created through some trial methods.⁷⁸

A classical trial method consists of two stages, mutation and recombination. The mutation stage involves performing some mutation on the parent population to create a mutant vector, \mathbf{m} , analogous to the mutation in biological evolutionary theory. The magnitude of the mutation is dependent on the mutation constant, k_m ,

$$\mathbf{m}_{i,j} = b_i + k_m(\mathbf{p}_{i,R1} - \mathbf{p}_{i,R2}), \quad (2.47)$$

where b_i is the best candidate solution in the parent population, and $\mathbf{p}_{i,R1}$ and $\mathbf{p}_{i,R2}$ are randomly chosen members of the parent population. The mutation constant can be considered as a control variable for the size of the search radius, with a large k_m corresponding to a larger search radius.

The recombination step creates the offspring population vector by taking a sample from either the parent population or mutant vectors with some frequency, which depends on the recombination constant, k_r ,

$$\mathbf{o}_{i,j} = \begin{cases} \mathbf{m}_{i,j}, & \text{where } X < k_r \\ \mathbf{p}_{i,j}, & \text{otherwise} \end{cases} \quad (2.48)$$

where, $X \sim U[0, 1]$. The recombination constant controls the progress of the algorithm as it impacts the frequency with which mutation is introduced into the offspring population vector.

The final stage is to compare the offspring and parent population vectors, in the selection stage to create the new parent population for the next iteration. The selection stage comprises of using

⁷⁴ Wormington *et al.*, "Characterization of Structures from X-Ray Scattering Data Using Genetic Algorithms", op. cit.

⁷⁵ Björck, "Fitting with Differential Evolution: An Introduction and Evaluation", op. cit.; M. Björck *et al.* *J. Appl. Crystallogr.* 40.6 (2007), pp. 1174–1178; Nelson, "Co-Refinement of Multiple-Contrast Neutron/X-Ray Reflectivity Data Using MOTOFIT", op. cit.; Nelson *et al.*, "Refnx: Neutron and X-Ray Reflectometry Analysis in Python", op. cit.; F. Ott. *SimulReflec*. URL: <http://www-l1b.cea.fr/prism/programs/simulreflec/simulreflec.html> (Accessed 2019-3-4); P. A. Kienzle *et al.* *NCNR Reflectometry Software*. URL: <http://www.ncnr.nist.gov/reflpak> (Accessed 2018-3-4).

⁷⁶ Storn *et al.*, "Differential Evolution – A Simple and Efficient Heuristic for Global Optimization over Continuous Spaces", op. cit.

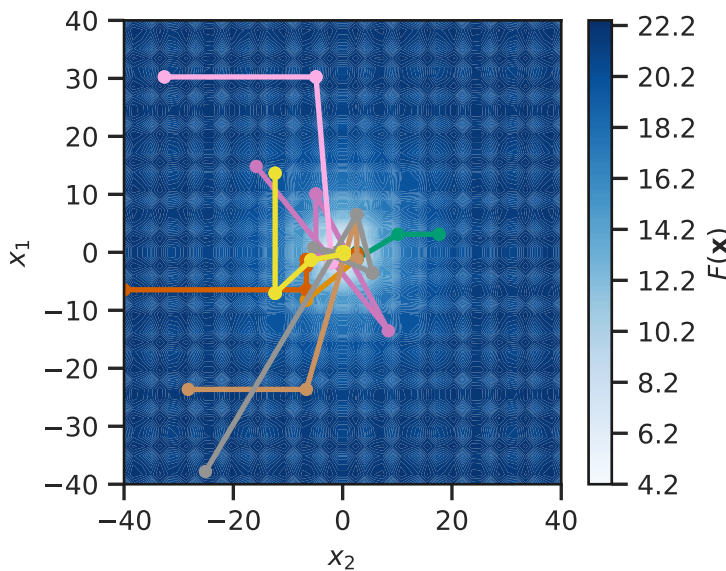
⁷⁷ J. H. Holland. *Adaptation in Natural and Artificial Systems*. 1992.

⁷⁸ Many of these exist however we will discuss a simple classical trial method, details of other methods may be found in Björck, "Fitting with Differential Evolution: An Introduction and Evaluation", op. cit.

some figure of merit, ζ , to choose between the subunit from the offspring or parent population vector. In our example, that figure of merit may be the agreement between some experimental data and our model, or for the example in Figure 2.18 it is the value of the Ackley function,⁷⁹ which we are trying to minimise.⁸⁰

$$\mathbf{p}_{*,j} \leftarrow \begin{cases} \mathbf{o}_{*,j}, & \text{where } \zeta_{\mathbf{o}_{*,j}} < \zeta_{\mathbf{p}_{*,j}} \\ \mathbf{p}_{*,j}, & \text{otherwise} \end{cases} \quad (2.49)$$

where, the $*$ notation indicates all objects in the given population, and $\zeta_{\mathbf{o}_{*,j}}$ and $\zeta_{\mathbf{p}_{*,j}}$ are the figures of merit for the offspring and population candidate solutions respectively.



⁷⁹ D. H. Ackley. "A Connectionist Machine for Genetic Hillclimbing". PhD. Michigan, US: University of Michigan, 1987. 260 pp.

⁸⁰ The Ackley function is a common function used for assessing the utility of global optimisation functions.

Figure 2.18: An example of a differential evolution (DE) algorithm as applied to an Ackley function, where $a = 20$, $b = 0.2$, and $c = 2\pi$. The mutation and recombination constant in this implementation are both 0.5. Each different coloured line represents a different candidate solution. The optimisation was stopped after 100 iterations had run.

It is noted that it is often the case,⁸¹ that there should be some bounds applied to the variables within the populations. However, the DE algorithm may disregard these bounds due to the nature of the mutation step. Therefore, it is common in DE algorithms, where bounds must be set, that if the search space moves outside that expected it is necessary to reinitialise the parameter. An implementation of the DE algorithm is given programmatically in Code Block 2.3,⁸² where this reinitialisation is achieved by obtaining a new random number within the given bounds.

2.4.2 Particle swarm

Particle swarm optimisation⁸³ is a type of swarm intelligence population-based optimisation method. This optimisation method was originally developed by Kennedy, Eberhart, and Shi.⁸⁴ Particle swarm methods are particularly suitable for the optimisation, and

⁸¹ In particular for the optimisation of experimental data.

⁸² Additional Code Blocks showing the mutation, recombination, selection steps may be found in Appendix A.

⁸³ Abbreviated to PSO.

⁸⁴ Kennedy *et al.*, "Particle Swarm Optimization", op. cit.; Shi *et al.*, "A Modified Particle Swarm Optimizer", op. cit., the initial purpose of the algorithm was to simulate social organisms such as bird flocks.

```

import numpy as np
import mutation as mut
import recombination as recomb
import selection as sel

def differential_evolution(population, f, km, kr, bounds, max_iter):
    history = np.array([population])
    best = population[:, np.argmin(f(population))]
    i = 0
    while i < max_iter:
        mutant = mut.mutation(population, best, km)
        offspring = recomb.recombination(population, mutant, kr)
        offspring[
            np.where(offspring >= bounds[1])
            | np.where(offspring < bounds[0])
        ] = np.random.uniform(bounds[0], bounds[1], 1)
        selected = sel.selection(population, offspring, f)
        history = np.append(history, selected)
        history = np.reshape(
            history, (i + 2, population.shape[0], population.shape[1])
        )
        population = np.array(selected)
        best = population[:, np.argmin(f(population))]
        i += 1
    return history

```

Code Block 2.3: An example of a simple implementation for a DE algorithm as described in M. Björck. *J. Appl. Crystallogr.* 44.6 (2011), pp. 1198–1204. The input variables are `population` which is an array of floats containing the initial parent population, `f` which is the figure of merit function to be minimised, `km` which is the mutation constant, `kr` which is the recombination constant, `bounds` which is an array of floats giving the minimum and maximum values for the variables, and `max_iter` which is the maximum number of iterations that should be performed. This will return `history` which is a history of the variables that are being fit during the DE algorithm.

sampling, of parametric search-spaces with a large number of similar minima. Therefore, I believe that it will be useful for the study of the self-assembly of soft matter materials.⁸⁵

These methods consist of a population vector, similar to that described for the differential evolution, that moves around the parametric search-space. The motions of these “particles” are influenced by the positions of the other particles in the vector.⁸⁶ It is anticipated that this will lead the swarm to optimise the function under investigation.

Particles in the swarm are under the influence of two elastic forces. The first attracts the particle to the best location in the search-space that the particular particle has found, while the other attracts the particle to the best search-space location found by any particle of the swarm. The magnitudes of these forces are randomised but modulated by a pair of acceleration coefficients; ψ_p that influences the attraction towards the personal best location and ψ_g that influences the attraction to the global best location. The position of a particle changes between iterations of the algorithm based on the following relation,

$$\mathbf{p}_{*,j} \leftarrow \mathbf{p}_{*,j} + \mathbf{v}_{*,j}, \quad (2.50)$$

where, $\mathbf{p}_{*,j}$ is the position of the particle, and $\mathbf{v}_{*,j}$ is the velocity of the particle. This velocity is determined as shown below,

$$\mathbf{v}_{*,j} \leftarrow \omega \mathbf{v}_{*,j} + \psi_g R1(\mathbf{g}_* - \mathbf{p}_{*,j}) + \psi_p R2(\mathbf{s}_{*,j} - \mathbf{p}_{*,j}), \quad (2.51)$$

where, ω a constant known as the interia weight, $R1 \sim U[0, 1]$ and $R2 \sim U[0, 1]$ are random numbers, \mathbf{g}_* is the best position occupied by any particle in the swarm and $\mathbf{s}_{*,j}$ is the person best for the particle j .

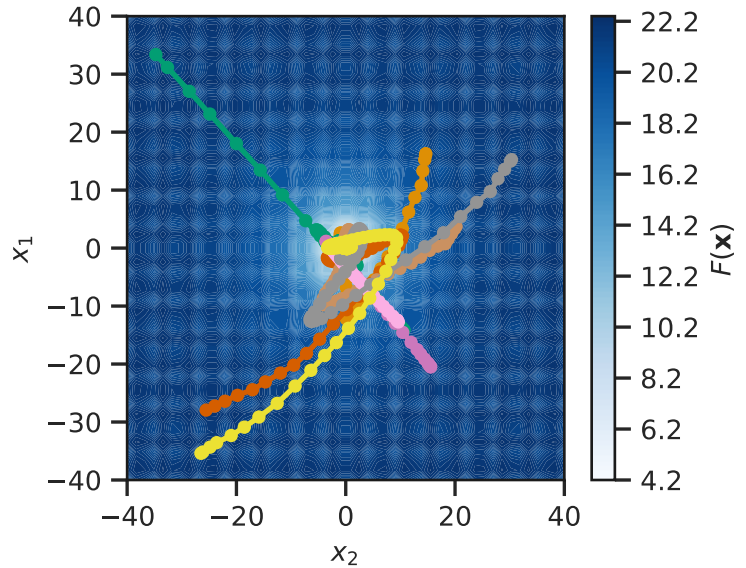
Figure 2.19 shows an example of the particle swarm optimisation in action, applied to the Ackley function.⁸⁷ Code Block 2.4 shows a functional programmatic implementation of a particle swarm optimisation algorithm.

⁸⁵ This is the focus of Chapter ??.

⁸⁶ Poli, “Analysis of the Publications on the Applications of Particle Swarm Optimisation”, op. cit.

⁸⁷ Ackley, “A Connectionist Machine for Genetic Hillclimbing”, op. cit.

Figure 2.19: An example of a particle swarm optimisation as applied to an Ackley function, where $a = 20$, $b = 0.2$, and $c = 2\pi$. For the particle swarm, the following parameters were used $\omega = 0.9$, $\psi_g = 0.05$, and $\psi_p = 0.05$. Each different coloured line represents a different candidate solution. The optimisation was stopped after 100 iterations had run.



Code Block 2.4: An example of the particle swarm optimisation algorithm from R. Poli. *J. Artif. Evol. Appl.* 2008 (2008), pp. 1–10. The input variables are `position` which is the initial position vector, `f` which is the figure of merit function to be minimised, `omega` which is the interia weight, `psig` which is the global acceleration constant, `psip` which is the personal acceleration constant, and the `max_iter` which is the maximum number of iterations that should be performed. This will return the `history` which is a history of the variables that are being fit during the PSO.

```
import numpy as np

def particle_swarm(position, f, omega, psig, psip, max_iter):
    history = np.array([position])
    velocity = np.zeros_like(position)
    g_best = position[:, np.argmin(f(position))]
    p_best = np.array(position)
    i = 0
    while i < max_iter:
        for j in range(velocity.shape[1]):
            velocity[:, j] = (
                omega * velocity[:, j]
                + psig * np.random.rand() * (g_best - position[:, j])
                + psip
                * np.random.rand()
                * (p_best[:, j] - position[:, j])
            )
        position[:, j] = position[:, j] + velocity[:, j]
        history = np.append(history, position, axis=0)
        history = np.reshape(
            history, (i + 2, position.shape[0], position.shape[1])
        )
        test_g_best = position[:, np.argmin(f(position))]
        if f(test_g_best) < f(g_best):
            g_best = test_g_best
        test_p_best = np.array(position)
        for j in range(position.shape[1]):
            if f(test_p_best[:, j]) < f(p_best[:, j]):
                p_best[:, j] = test_p_best[:, j]
        i += 1
    return history
```

⁸⁸ Abbreviated to MCMC.

⁸⁹ W. Krauth. *Statistical Mechanics: Algorithms and Computations*. Oxford Master Series in Statistical, Computational, and Theoretical Physics 13. 2006.

⁹⁰ D. S. Sivia *et al.* *Data Analysis: A Bayesian Tutorial*. 2006.

⁹¹ This is the name given to the uncertainties in the parameters fitted in the modelling process.

⁹² W. Gilks *et al.* *Markov Chain Monte Carlo in Practice*. Chapman & Hall/CRC Interdisciplinary Statistics. 1995.

⁹³ Metropolis *et al.*, "Equation of State Calculations by Fast Computing Machines", op. cit.; Hastings, "Monte Carlo Sampling Methods Using Markov Chains and Their Applications", op. cit.

⁹⁴ K. Levenberg. *Quart. Appl. Math.* 2.2 (1944), pp. 164–168; D. W. Marquardt.

J. Soc. Indust. Appl. Math. 11.2 (1963), pp. 97–109. An example of the Metropolis-Hastings MCMC algorithm from N. Metropolis *et al.* *J. Chem. Phys.* 21.6 (1953), pp. 1087–1092;

W. K. Hastings. *Biometrika* 57.1 (1970), pp. 97–109. The input variables are *theta* which is an array of floats giving the initial values for the variables, *f* which is the figure of merit function to be minimised, *a* which is the step size for the changes, *data* which is the experimental data, *iterations* which is the number of accepted iterations to obtain, and *nburn* which is the number of accepted iterations to ignore in the burn-in phase. This will return the *history* which is a history of the variables that are being fit during the PSO.

2.4.3 Markov chain Monte-Carlo

Markov chain Monte Carlo⁸⁸ is a sampling methodology, derived from direct sampling Monte-Carlo.⁸⁹ The aim of an MCMC algorithm is to sample a probability distribution, when parameters are described in terms of their degree of probability.⁹⁰ Similar to MD, in practical terms, MCMC should not be used on a system that is not already optimised, as its purpose is probability distribution sampling rather than minimisation. Generally, the approach would be to optimise using, for example, one of the approaches described above, then to use MCMC or molecular dynamics to sample the appropriate search-space. For example, in this work MCMC is used following the optimisation of a reflectometry model using a differential evolution algorithm, to quantify the inverse uncertainties of the model.⁹¹ In addition to being able to give information about the inverse uncertainties, MCMC also offers a more complete understanding of the correlations present between the different parameters,⁹² as the interactions between the parameter variation has been quantified.

The aim of MCMC is to only sample configurations of a given function that are within the experimental uncertainty. Figure 2.20 shows an example of the possible output that may be obtained from the application of an MCMC sampling method. This was generated using a Metropolis-Hastings MCMC algorithm,⁹³ shown in Code Block 2.5. Initially, a Levenberg–Marquardt algorithm⁹⁴ was used to optimise the positions and integral of the two Gaussian functions that make up the data. The MCMC was used to sample the values that were within the experimental uncertainty.

```
import numpy as np

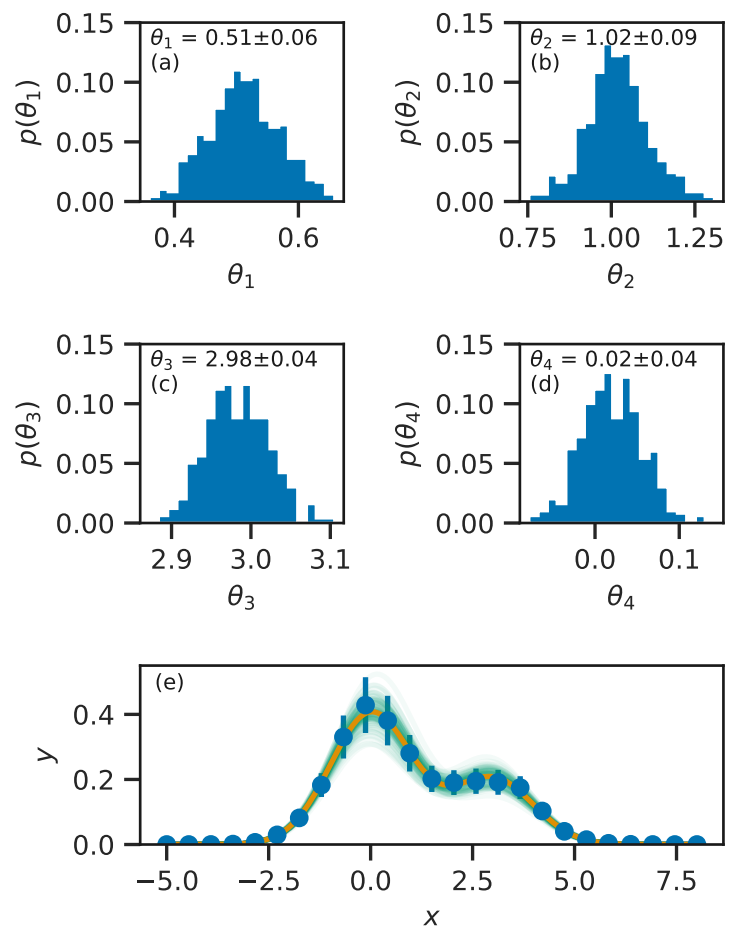
def mcmc(theta, f, a, data, iterations, nburn):
    accepted = np.array([])
    calc_y = f(data[0], theta)
    chi2 = np.sum(np.square((data[1] - calc_y) / data[2]))
    i = 0
    while i < iterations:
        new_theta = theta + a * np.random.randn(theta.size)
        new_calc_y = f(data[0], new_theta)
        new_chi2 = np.sum(np.square((data[1] - new_calc_y) / data[2]))
        prob = np.exp((-new_chi2 + chi2) / 2)
        n = np.random.rand()
        if n < prob:
            i += 1
            theta = new_theta
            chi2 = new_chi2
            if i > nburn:
                accepted = np.append(accepted, theta)
                accepted = np.reshape(
                    accepted, (i - nburn, theta.size))
    return accepted
```

Once an optimised solution, θ , is obtained, the figure of merit is calculated, in Code Block 2.5 this is the agreement between the model and the experimental data, χ^2 , where,

$$\chi^2 = \sum \frac{(y_{\text{exp}} - y_{\text{calc}})^2}{dy_{\text{exp}}}, \quad (2.52)$$

and y_{exp} is the experimental data, and dy_{exp} the uncertainty in the experimental data, while y_{calc} is the model solution. Some random

Figure 2.20: An example of a four variable (two nearby Gaussian functions of different sizes with added random noise and some fractional uncertainty) problem probed using a MCMC method, using values of $a = 0.1$, θ_1 and θ_2 correspond to the integral of the Gaussian function, while θ_3 and θ_4 indicate their positions; (a)-(d) histograms of the probability distribution function for each of the variables, and (e) the data (blue circles), the optimised solution (orange line), and a series of probable solutions (green lines) showing the variability present in the data uncertainty.



perturbation is then applied to the optimised solution,

$$\Theta = \theta + aR, \quad (2.53)$$

where $R \sim N(0, 1)$ and a is the step size. A new χ^2 is found for Θ , and the probability that this transition will occur is found,

$$p = \exp\left(\frac{-\chi^2(\Theta) + \chi^2(\theta)}{2}\right). \quad (2.54)$$

This probability is then compared with a random number $n \sim U[0, 1]$, and if n is less than the probability, the new solution is stored,

$$\theta \leftarrow \Theta. \quad (2.55)$$

This process is repeated until some desired number of samples has been obtained. It should be noted that in the event on a poorly optimised initial value of θ , it may be necessary to ‘burn’⁹⁵ the first series of solutions while the MCMC algorithm settles into the search-space.

2.4.4 Molecular dynamics

Section 2.3 introduced classical potential models as a method for the evalution of the interaction energy of a given chemical system. Any of the optimisation methods discussed above could be used alongside these classical potential models to find an energy minimum structure for the system or to sample the potential energy landscape. However, it is often the case that we are interested in a dynamically relevant structure at a given temperature for some system. This is where molecular dynamics simulations are a useful and important tool.

The aim of a molecular dynamics simulation is to probe the positions, velocities, and accelerations on each of the atoms, or coarse-grained particles, as a simulation progresses. The acceleration on a given particle, \mathbf{a} is defined by the force on that particle, \mathbf{f} , in agreement with Newton’s second law of motion,

$$\mathbf{f} = m\mathbf{a}, \quad (2.56)$$

where, m is the mass of the particle. In order to determine the acceleration on the particle, it is necessary to know the force on that particle. The force, f , is a function of the potential energy, E , as found from a classical potential, of that atom,

$$f(r) = \frac{-\delta E_{\text{total}}(r)}{\delta r}, \quad (2.57)$$

⁹⁵ The force is the negative of the first derivative of the energy with respect to the atomic configuration.

where, r is the configuration of the atoms.⁹⁶ The force found from Equation 2.57 is a scalar, however, we are interested in the force vector in Equation 2.56. To determine the force in a given direction, it is necessary to find the product of the force, f , and the unit vector in that direction,

$$\mathbf{f}_x = f\hat{\mathbf{r}}_x, \quad \text{where } \hat{\mathbf{r}}_x = \frac{\mathbf{r}_x}{|\mathbf{r}|}, \quad (2.58)$$

where r_x is the atomic configuration in the x -dimension, and $|\mathbf{r}|$ is the magnitude of the atomic configuration vector.

The potential model, which we define for a given system, allows for the calculation of the acceleration on each particle in that system. The next step is to use this acceleration to iterate through the trajectory of our system. This is achieved by applying Newtonian equations of motion, for example in the Velocity-Verlet algorithm.⁹⁷

$$\mathbf{x}(t + \Delta t) = \mathbf{x}(t) + \mathbf{v}(t)\Delta t + \frac{1}{2}\mathbf{a}(t)\Delta t^2, \quad (2.59)$$

$$\mathbf{v}(t + \Delta t) = \mathbf{v}(t) + \frac{1}{2}[\mathbf{a}(t) + \mathbf{a}(t + \Delta t)]\Delta t, \quad (2.60)$$

where, \mathbf{x} is the position the particle \mathbf{v} is the particle's velocity, and \mathbf{a} is the particle's acceleration, while t is current simulation time and Δt is the timestep. These equations constitute the Velocity-Verlet algorithm,

1. calculate the force, and therefore the acceleration, on each particle,⁹⁸
2. find the position of the particle after some timestep,⁹⁹
3. determine the new velocity for each particle, based on the average acceleration at the current and new positions,¹⁰⁰
4. overwrite the old acceleration values with the new ones,
5. go to 1.

Following an equilibration period, this algorithm may be iterated as many times as is required to obtain sufficient statistics for the measurement quantity of interest, e.g. particle positions for structural techniques such as elastic scattering.

The above analytical process is known as the integration step, and the Velocity-Verlet is the integrator. If the size of the timestep Δt is too large, the step size for a given iteration will not be accurate, as the forces on the atoms will change too significantly during it. Therefore, the values of the timestep is usually on the order of 10×10^{-15} s.¹⁰¹ This means that in order to simulate a single nanosecond of "real-time" molecular dynamics, the integrator must be solved one million times. This can be slow for very large systems, leading to an interest in coarse-grained simulations that result in fewer particles to determine the forces for, but also enable to use of larger timesteps,¹⁰² for example, the use of a MARTINI potential model allows for an upto twenty times increase in the timestep compared to an all-atom model.

The above discussion ignored two aspects that are necessary to run a molecular dynamics simulation, both of which are associated with the original configuration of the system; the original particle positions and velocities. The particle positions are usually taken from some library, for example for the simulation of a

⁹⁷ W. C. Swope *et al.* *J. Chem. Phys.* 76.1 (1982), pp. 637–649.

⁹⁸ Using Equations 2.56 & 2.57.

⁹⁹ Using Equation 2.59.

¹⁰⁰ Using Equation 2.60.

¹⁰¹ femtoseconds.

¹⁰² R. E Rudd *et al.* *Phys. Rev. B* 58.10 (1998), R5893–R5896; E. Brini *et al.* *Soft Matter* 9.7 (2013), pp. 2108–2119, so fewer, faster integration steps must be solved.

¹⁰³ RCSB PDB: Protein Data Bank.
URL: <http://www.rcsb.org>

(Accessed 2018-1-28).
¹⁰⁴ Jmol: An Open-Source Java Viewer
for Chemical Structures in 3D. URL:
<http://www.jmol.org/>

(Accessed 2018-1-28).
¹⁰⁵ L. Martínez *et al.* *J. Comput. Chem.* 30.13 (2009), pp. 2157–2164.

¹⁰⁶ This can be much longer than could
be reasonably simulated.

protein, often the protein data bank¹⁰³ is a useful resource. Small molecules may be configured by hand using graphical programs such as Jmol.¹⁰⁴ These small molecules may be built into complex, multicomponent structures using software such as the Packmol package.¹⁰⁵ The importance of this initial structure cannot be overstated, for example, if the initial structure in a molecular dynamics simulation is unrepresentative of the equilibrium structure, it may take a large amount of simulation time before the equilibrium structure is obtained.¹⁰⁶

The initial particle velocities are obtained in a much more general fashion. They are selected randomly, and then scaled such that the kinetic energy, E_k , of the system agrees with a defined temperature, T ,

$$E_k = \sum_{i=1}^N \frac{m_i |\mathbf{v}_i|^2}{2} = \frac{3}{2} N k_B T, \quad (2.61)$$

where, m_i and \mathbf{v}_i are the masses and velocities of the particles, N is the number of particles, and k_B is the Boltzmann constant.

The above algorithm details a simulation that makes use of an NVE ensemble.¹⁰⁷ However, this is not the only simulation ensemble that is available, within this work two other ensembles have been used extensively,

- the NVT (canonical) ensemble; this is similar to the NVE ensemble except the simulation temperature is controlled via a thermostat,
- the NPT (isothermal-isobaric); this ensemble is similar to the NVT ensemble, however, the system volume is allowed to vary while the overall system pressure is held constant using a barostat.

¹⁰⁷ A simulation where the number of particles (N), the volume of the system (V), the energy of the system (E) are all kept constant.

¹⁰⁸ Using Equation 2.61.

¹⁰⁹ H. C. Andersen. *J. Chem. Phys.* 72.4 (1980), pp. 2384–2393; S. Nosé. *J. Chem. Phys.* 81.1 (1984), pp. 511–519; H. J. C. Berendsen *et al.* *J. Chem. Phys.* 81.8 (1984), pp. 3684–3690; W. G. Hoover. *Phys. Rev. A* 31.3 (1985), pp. 1695–1697.

¹¹⁰ A. R. McCluskey *et al.* *J. Open Source Educ.* 1.2 (2018), pp. 19–21; A. R. McCluskey *et al.* *Arm61/Pylj: Pylj-1.1.0*. 2018. URL: <http://doi.org/10.5281/zenodo.1403828>; Discussed in detail in Chapter ??.

¹¹¹ G. Bussi *et al.* *J. Chem. Phys.* 126.1 (2007), p. 014101.

Thermostating involves controlling the kinetic energy of the particles¹⁰⁸ such that the simulation temperature is kept at a predefined value. There are a variety of methods for thermostating a molecular dynamics simulation, such as the Andersen, Nosé-Hoover, or Berendsen methods.¹⁰⁹ However, the most straightforward to describe, and that implemented in the *pylj* software¹¹⁰ is a velocity rescaling.¹¹¹ This is where the velocities for a random subset of the particles, \mathbf{v}_i are adapted based on the following relation,

$$\mathbf{v}_i \leftarrow \mathbf{v}_i \sqrt{\frac{T_{\text{target}}}{\bar{T}}} \quad (2.62)$$

where, T_{target} is the target temperature, and \bar{T} is the average simulation temperature.

The use of a barostat to control the simulation pressure usually involves varying the simulation cell parameters and the distances between the particles. This would in a similar way to thermostating, where the simulation dimensions are scaled by a value in an

effort to control the pressure. The barostating methods are similar to the thermostating methods with Andersen, Nosé-Hoover, and Berendsen methods. However, there is also the Parrinello-Rahman barostat which allows for independent control of the different cell dimensions giving control of stress in addition to pressure.¹¹²

These optimisation and sampling methods were used in a variety of different applications within this work, firstly differential evolution optimisation and MCMC sampling are used in Chapter 3 in the study of a chemically-consistent modelling approach to X-ray and neutron reflectometry analysis. Molecular dynamics simulation are investigated as a possible tool to assist in the analysis of reflectometry in Chapter 4. Finally, the particle swarm optimisation is applied for the efficient determination of a micelle structure for fitting small angle scattering data in Chapter ??.

¹¹² M. Parrinello *et al.* *J. Appl. Phys.* 52.12 (1981), pp. 7182–7190.

3

CHEMICALLY CONSISTENT MODELLING OF X-RAY AND NEUTRON REFLECTOMETRY

ABSTRACT

The work discussed in this chapter is the first example of the use of a chemically-consistent reflectometry model to co-refine X-ray reflectometry measurements at different surface pressures. This was coupled with a differential evolution optimisation and Markov chain Monte Carlo sampling methodology in order to rationalise the model inverse uncertainties and correlations. This chemically-consistent modelling approach was applied to the study of phospholipid monolayers at the air-deep eutectic solvent interface, which required that the head and tail group volumes were not constrained. By co-refining multiple experimental datasets, it was possible to accurately model the experimental data without these constraints present.

CONTEXT

This project offers a severe method of coarse-graining for the analysis of neutron and X-ray reflectometry data. The system is coarse-grained to represent a head group and a tail group of a phospholipid species. There is a chemical constraint present in the model, such that the number of head groups must be equal to the number of pairs of tail groups. However, there is no potential model considered beyond this “bonded” interaction. Additionally, this modelling approach is applied again in Chapter 4, as an example of the cutting edge of traditional modelling, against which the classical simulation-driven methods are compared. The specific application of this modelling approach grew from a collaboration with experimental colleagues working on self-assembly in deep eutectic solvents. Therefore, this chemical system will be briefly introduced in Section 3.1. However, the main focus of this chapter will be the modelling methodology

3.1 INTRODUCTION

3.1.1 Deep eutectic solvents

¹ Abbreviated to DES.

² E. L. Smith *et al.* *Chem. Rev.* 114.21 (2014), pp. 11060–11082; Y. Dai *et al.* *Anal. Chim. Acta* 766 (2013), pp. 61–68.

³ O. S. Hammond *et al.* *Green Chem.* 18.9 (2016), pp. 2736–2744; O. S. Hammond *et al.* *J. Phys. Chem. B* 121.31 (2017), pp. 7473–7483; C. F. Araujo *et al.* *Phys. Chem. Chem. Phys.* 19.27 (2017), pp. 17998–18009.

⁴ A. Pandey *et al.* *Phys. Chem. Chem. Phys.* 16.4 (2014), pp. 1559–1568.

⁵ Smith *et al.*, “Deep Eutectic Solvents (DESs) and Their Applications”, op. cit.

⁶ S. Zahn *et al.* *ChemPhysChem* 17.21 (2016), pp. 3354–3358.

⁷ B. D. Ribeiro *et al.* *ACS Sustain. Chem. Eng.* 3.10 (2015), pp. 2469–2477; D. J. G. P. van Osch *et al.* *Green Chem.* 17.9 (2015), pp. 4518–4521.

⁸ A. Sanchez-Fernandez *et al.* *Phys. Chem. Chem. Phys.* 18.48 (2016), pp. 33240–33249; T. Arnold *et al.* *Langmuir* 31.47 (2015), pp. 12894–12902; Y.-T. Hsieh *et al.* *Langmuir* 34.35 (2018), pp. 10270–10275; M. K. Banjare *et al.* *RSC Adv.* 8.15 (2018), pp. 7969–7979.

⁹ S. J. Bryant *et al.* *Soft Matter* 12.6 (2016), pp. 1645–1648; S. J. Bryant *et al.* *Langmuir* 33.27 (2017), pp. 6878–6884; M. G. Gutiérrez *et al.* *Langmuir* 25.10 (2009), pp. 5509–5515.

¹⁰ L. Sapir *et al.* *J. Phys. Chem. A* 120.19 (2016), pp. 3253–3259.

¹¹ A. Sanchez-Fernandez *et al.* *Phys. Chem. Chem. Phys.* 19.13 (2017), pp. 8667–8670.

¹² Mohwald, “Phospholipid and Phospholipid-Protein Monolayers at the Air-Water Interface”, op. cit.; Kewalramani *et al.*, “Effects of Divalent Cations on Phase Behavior and Structure of a Zwitterionic Phospholipid (DMPC) Monolayer at the Air-Water Interface”, op. cit.

¹³ Dai *et al.*, “Natural Deep Eutectic Solvents as New Potential Media for Green Technology”, op. cit.; Hammond *et al.*, “Resilience of Malic Acid Natural Deep Eutectic Solvent Nanostructure to Solidification and Hydration”, op. cit.

¹⁴ F. Graner *et al.* *J. Phys. II France* 5.2 (1995), pp. 313–322.

¹⁵ S. P. Weinbach *et al.* *J. Phys. Chem.* 97.20 (1993), pp. 5200–5203; O. M. Magnussen *et al.* *Nature* 384 (1996), pp. 250–252; H. Kraack *et al.* *Science* 298.5597 (2002), pp. 1404–1407.

Deep eutectic solvents¹ are a class of green, sustainable liquids that may be obtained from the combination of ionic species with compounds capable of acting as hydrogen bond donors, such as sugar, alcohols, amines, and carboxylic acids.² The resulting extensive hydrogen bonding network is capable of stabilising both species, such that the eutectic mixture will remain liquid at room temperature.³ Using different precursor materials can allow for the ability to tune the resulting solvent’s physicochemical properties, such as polarity,⁴ viscosity and surface tension,⁵ network charge,⁶ and hydrophobicity.⁷ Recently DES have also been shown to exhibit a “solvophobic” effect through the promotion of surfactant micelle formation,⁸ phospholipid bilayer formation,⁹ and the ability to stabilise non-ionic polymer¹⁰ and protein conformations.¹¹

Phospholipid monolayers at the air/water interface have been widely studied as simplistic models for biological membranes. As such, they have been used to gain insight into many biological processes that are technologically and medically relevant. For example, investigations at the air/salt-water interface have identified the importance that interactions between charged phospholipid head groups and ions present in solution have on the structure, monolayer packing and stability.¹² However, the native environment for phospholipids in-vivo is far from simple aqueous solutions. In fact, it has been suggested¹³ that DES might form within the crowded cellular environment and could assist in solubilizing biological species in an intermediate environment between that of the hydrophobic phospholipid tail groups and the highly polar water-rich regions, thereby assisting survival under extreme conditions such as freezing temperatures and drought where the water content of the cells is restricted.

This chapter presents the first observation of phospholipid monolayer at an air-DES interface. Furthermore, this is one of a few examples of a phospholipid monolayer at the interface between air and a non-aqueous solvent, with only formamide noted previously.¹⁴ Langmuir monolayers of non-phospholipidic surfactant molecules have also been noted at air-formamide and air-mercury interfaces.¹⁵ In these previous works, the authors noted that the non-aqueous surface had an effect on the overall structure of the monolayer, but little was said about the underlying mechanism.

3.1.2 Optimisation and sampling in reflectometry analysis

The analysis of reflectometry data usually involves the use of some model-dependent methodology. Therefore it is necessary to optimise the difference between our model, and the experimental dataset. Analytical methods, such as the gradient descent method

are not usually suitable for application to the optimisation of a reflectometry model, as these are only capable of optimisation to local minima, which would require accurate prior knowledge of the model structure.¹⁶ Despite the analytical nature of the Maximum entropy (MaxEnt) optimisation method, this showed some success in the optimisation of reflectometry models, due in part to the ability of this optimisation to produce of a large number of solutions.¹⁷ However, this approach is computationally intensive and therefore it is unusual to apply it instead of other more efficient methods. Some aspects of the MaxEnt methods were replicated in the work of Sivia *et al.*, which employed Bayesian probability theory to rationalise the model selection.¹⁸

The use of analytic methods became less favoured as more frequently stochastic methods were used, these offer a more pragmatic solution to the local minima problem. Stochastic methods are those that utilise inherently random behaviour to determine a global minimum. The groove tracking method of Zhou and Chen,¹⁹ was one of the first examples of a stochastic optimisation process applied to the analysis of reflectometry data. This randomly varied the SLD of the layers in the model using a Monte Carlo approach. A similar approach used a simulated annealing approach, with a “temperature” factor that decreased as the number of iterations increased,²⁰ however, this approach is still subject to the local minima problem as the probability of move acceptance decreased over time.

Both these Monte Carlo based approaches and the analytic methods previously discussed make the same perturbations to the fitted parameters during processing. However, this is the cause of the propensity to converge to a local minimum. This led to the application of genetic algorithm-derived methods for the optimisation of reflectometry models, beginning with the works of de Haan and Drijkoningen²¹ and Dane *et al.*²² These methods are designed to stochastically sample an entire search-space, and therefore are more able to overcome the local minima issues and determine the vicinity of a global minimum. Following this initial application, genetic algorithms were used frequently in the optimisation of reflectometry models²³ In particular, the work of Wormington *et al.*²⁴ showed the applicability of the differential evolution method towards reflectometry model optimisation, which resulted in the inclusion of such methods in many common reflectometry analysis software packages.²⁵

The use of Markov chain Monte Carlo (MCMC) methods to probe the probability distribution functions of the fitting parameters of a reflectometry model have also grown in popularity.²⁶ This is due to the inclusion of MCMC methods in common analysis software packages such as Refl1D.²⁷ These methods enable the user to better understand the inverse uncertainties of the model. Additionally, they enable the quantification of the correlation be-

¹⁶ M. R. Lovell *et al.* *Curr. Opin. Colloid Interface Sci.* 4.3 (1999), pp. 197–204.

¹⁷ M. Geoghegan *et al.* *Phys. Rev. E* 53.1 (1996), pp. 825–837; D. G. Bucknall *et al.* *Physica B* 241–243 (1997), pp. 1071–1073.

¹⁸ Geoghegan *et al.*, “Experimental Study of Surface Segregation and Wetting in Films of a Partially Miscible Polymer Blend”, op. cit.; D. S. Sivia *et al.* *Physica D* 66.1–2 (1993), pp. 234–242; D. S. Sivia *et al.* *Physica B* 248.1–4 (1998), pp. 327–337; D. S. Sivia *et al.* *Physica B* 173.1–2 (1991), pp. 121–138.

¹⁹ Xiao-Lin Zhou *et al.* *Physical Review E* 47.5 (1993), pp. 3174–3190; X.-L. Zhou *et al.* *Phys. Rep.* 257 (1995), pp. 223–348.

²⁰ K. Kunz *et al.* *Macromolecules* 26.16 (1993), pp. 4316–4323.

²¹ V.-O. de Haan *et al.* *Physica B* 198.1–3 (1994), pp. 24–26.

²² A. D. Dane *et al.* *Physica B* 253.3–4 (1998), pp. 254–268.

²³ A. Ulyanenkov *et al.* *Physica B* 283 (2000), pp. 237–241; A. Ulyanenkov *et al.* *J. Phys. D* 38 (10A 2005), A235–A238; E. Politsch *et al.* *J. Appl. Crystallogr.* 35.3 (2002), pp. 347–355; Wormington *et al.*, “Characterization of Structures from X-Ray Scattering Data Using Genetic Algorithms”, op. cit.

²⁴ Idem, “Characterization of Structures from X-Ray Scattering Data Using Genetic Algorithms”, op. cit.

²⁵ Björck, “Fitting with Differential Evolution: An Introduction and Evaluation”, op. cit.; Björck *et al.*, “GenX: An Extensible X-Ray Reflectivity Refinement Program Utilizing Differential Evolution”, op. cit.; Nelson, “Co-Refinement of Multiple-Contrast Neutron/X-Ray Reflectivity Data Using MOTOFIT”, op. cit.; Nelson *et al.*, “Reflnx: Neutron and X-Ray Reflectometry Analysis in Python”, op. cit.; Ott, *SimulReflec*, op. cit.; Kienzle *et al.*, *NCNR Reflectometry Software*, op. cit.

²⁶ D. L. Gil *et al.* *J. Phys. D* 45.23

²⁸ Nelson, "Co-Refinement of Multiple-Contrast Neutron/X-Ray Reflectivity Data Using MOTOFIT", op. cit.

²⁹ Storn *et al.*, "Differential Evolution – A Simple and Efficient Heuristic for Global Optimization over Continuous Spaces", op. cit.; E. Jones *et al.* *SciPy: Open Source Scientific Tools for Python*. URL: <http://www.scipy.org> (Accessed 2019-3-4).

³⁰ D. Foreman-Mackey *et al.* *Publ. Astron. Soc. PAc.* 125.925 (2013), pp. 306–312.

³¹ The history of this modelling is introduced well in Campbell *et al.*, "Structure of Surfactant and Phospholipid Monolayers at the Air/Water Interface Modeled from Neutron Reflectivity Data", op. cit.

³² K. Wojciechowski *et al.* *Langmuir* 32.35 (2016), pp. 9064–9073; K. Wojciechowski *et al.* *BBA - Biomembranes* 1858.2 (2016), pp. 363–373.

³³ F. Foglia *et al.* *Langmuir* 30.30 (2014), pp. 9147–9156; G. Bello *et al.* *BBA - Biomembranes* 1858.2 (2016), pp. 197–209.

³⁴ Campbell *et al.*, "Structure of Surfactant and Phospholipid Monolayers at the Air/Water Interface Modeled from Neutron Reflectivity Data", op. cit.

³⁵ C. W. McConlogue *et al.* *Langmuir* 13.26 (1997), pp. 7158–7164; D. Small. *J. Lipids Res.* 25 (1984), pp. 1490–1500.

³⁶ As is discussed in Section 3.3.

³⁷ C. M. Hollinshead *et al.* *Langmuir* 25.7 (2009), pp. 4070–4077.

tween parameters, important in ensuring that the model applied is suitably constrained such as to reduce the cross-correlation present between parameters.²⁸

This work applies a differential algorithm²⁹ to the optimisation of the reflectometry model. The search-space, available within the experimental uncertainty of the data is then sampled using MCMC, as implemented in emcee,³⁰ to understand the parameter probability distributions and quantify the inter-parameter correlations.

3.1.3 Chemically-consistent modelling

The use of chemically-consistent modelling is common in the fitting of X-ray and neutron reflectometry measurements from phospholipid monolayers to obtain structural insights.³¹ While it is possible to model the neutron reflectometry from a phospholipid monolayer with a single layer model,³² the use of at least two layers; representing the head and tail groups is more commonplace.³³ Even when two layers are utilised, it is often the case that the volumes of the head and tail groups, V_i , are used as constraints in the modelling process, as the SLD of a layer may be determined as follows,

$$\text{SLD}_i = \frac{b_i}{V_i} (1 - \phi_i) + \text{SLD}_s(\phi_s) \quad (3.1)$$

where, b_i is the scattering length of the head or tail, ϕ_i is the volume fraction of solvation by the solvent, SLD_s is the solvent scattering length density, and i indicates either the head or tail layer. However, as noted by Campbell *et al.*,³⁴ this method often fails to account for the compaction of the carbon chains under elevated surface pressures,³⁵ which may lead to a volume reduction of up to ~15 %. Furthermore,³⁶ the use of a constrained head group volume may also influence the result of the modelling process in situations where the volume is poorly defined.

Equation 3.1 enables the use of chemical-inference in the modelling approach for reflectometry data. This allows for the co-refinement of neutron reflectometry data where different isotopic-contrasts of the phospholipid species or solvent have been used. This is possible based on the expectation that the effect of contrast variation on the structure and chemistry of the monolayer will be negligible, and therefore the same values of all parameters in the fitting, except b_i and SLD_s may be constrained between the different measurements.³⁷ In this work, similar logic was applied, with the assumption that the volume of the head and tail groups is constant across different surface pressures, while the phospholipid phase is the same. This means that, for this system, all of the fitted parameters may be constrained aside from the tail thickness, head solvation, and interfacial roughness, across the different surface pressure measurements. This is the first time that such a methodology has been applied to the analysis of X-ray reflectometry and

neutron reflectometry,³⁸ additionally, it is believed that this ability to co-refine XRR measurements enables a greater understanding of the structure than that possible from a single measurement.

3.2 EXPERIMENTAL

My role in this work was entirely on the analysis of the measurements and the development of the chemically-consistent model.³⁹ However, it is necessary to briefly discuss the materials and experimental methods used to enable a complete understanding of the context of the work.

3.2.1 Materials

Choline chloride (99 %, Sigma-Aldrich), glycerol (99 %, Sigma-Aldrich), d₉-choline chloride (99 %, 98 % D, CK Isotopes), and d₈-glycerol (99 %, 98 % D, CK Isotopes) were used in the preparation of the DES. This is achieved by mixing a 1:2 ratio of choline-chloride and glycerol and heating at 80 °C until a homogeneous, transparent liquid is formed.⁴⁰ This was then stored under a dry atmosphere to reduce the amount of water dissolved in the solvent.

The limited availability of deuterated precursors lead to only a fully protonated (hDES) and a partially deuterated (hdDES) being prepared and used in the neutron reflectometry measurements. The partially deuterated subphase was prepared using the following mixtures of precursors: 1 mol of 0.38 mol fraction of h-choline-chloride/0.62 mol fraction of d-choline-chloride; and 2 mol of 0.56 mol fraction of h-glycerol/0.44 mol fraction of d-glycerol.

The water content of the DES was assessed before and after each experiment by Karl-Fisher titration (Mettler Toledo DL32 Karl-Fischer Coulometer, Aqualine Electrolyte A, Aqualine Catholyte CG A) and found to be always below 0.3 wt %. This was taken to be a negligible amount and would not have a considerable impact on the DES characteristics.⁴¹

1,2-dipalmitoyl-*sn*-glycero-3-phosphocholine (C₁₆ tails, >99 %), 1,2-dimyristoyl-*sn*-glycero-3-phosphocholine (C₁₄ tails, >99 %), and the sodium salt of 1,2-dimyristoyl-*sn*-glycero-3-phospho-(1'-rac-glycerol) (C₁₄ tails, >99 %)⁴² were obtained from Avanti Polar Lipids and 2-dilauroyl-*sn*-glycero-3-phosphocholine (C₁₂ tails, >99 %)⁴³ was obtained from Sigma Aldrich and all were used without further purification. Deuterated versions of DPPC (d₆₂-DPPC, >99 %, deuterated tails-only) and DMPC (d₅₄-DMPC, >99 %, deuterated tails-only) were obtained from Avanti Polar Lipids and used without further purification. These phospholipids were dissolved in chloroform solution (0.5 mg mL⁻¹) at room temperature. PC indicates where the phospholipid molecule contains a phosphocholine head group, while PG indicates a phosphatidyl-glycerol head group, the chemical structures of these can be seen in

³⁸ Abbreviated to XRR and NR respectively.

³⁹ The experimental measurements were designed and conducted by Drs Tom Arnold, Andrew Jackson, Adrian Sanchez-Fernandez, and Prof. Karen Edler, with the assistance of Dr Richard Campbell.

⁴⁰ Smith *et al.*, "Deep Eutectic Solvents (DESs) and Their Applications", op. cit.

⁴¹ Hammond *et al.*, "Liquid Structure of the Choline Chloride-Urea Deep Eutectic Solvent (Reline) from Neutron Diffraction and Atomistic Modelling", op. cit.; Hammond *et al.*, "Resilience of Malic Acid Natural Deep Eutectic Solvent Nanostructure to Solidification and Hydration", op. cit.

⁴² Abbreviated to DPPC, DMPC, and DMPG respectively.

⁴³ Abbreviated to DLPC.

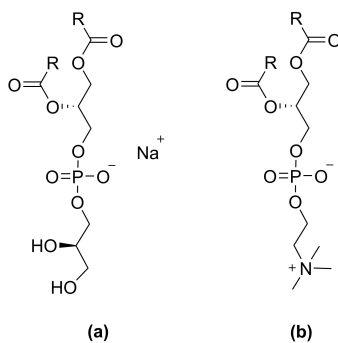


Figure 3.1: The two phospholipid forms investigated in this work, where R indicates the hydrocarbon tail; (a) phosphatidylglycerol (PG), (b) phosphocholine (PC).

⁴⁴ Abbreviated to PTFE

Figure 3.1.

In the XRR experiment, the sample was prepared in-situ using the standard method for the spreading of insoluble monolayers on water. A certain amount of the phospholipid solution was spread on the liquid surface. Following the evaporation of the chloroform, it is assumed that the resulting system is a subsurface of solvent with a monolayer of the phospholipid at the interface. The surface concentration is then controlled by opening and closing the polytetrafluoroethylene⁴⁴ barriers of a Langmuir trough. To reduce the volume used in the NR experiments, a small Delrin adsorption trough was used that did not have controllable PTFE barriers. Therefore, although the surface concentration was nominally the same as for the XRR, the lack of precise control meant that it was determined to be inappropriate to co-refine the XRR and NR contrasts together.

3.2.2 Methods

The XRR measurements were carried out at the I07 beamline at the Diamond Light Source, with a photon energy of 12.5 keV using the double-crystal deflector system.⁴⁵ The reflected intensity was measured for a q range of 0.018–0.7 Å⁻¹. The data were normalised with respect to the incident beam and the background was measured from off-specular reflection and subsequently subtracted. All of the samples were allowed at least one hour to equilibrate and preserved under an argon atmosphere. XRR data were collected for each of the phospholipids, DLPC, DMPC, DPPC, and DMPG at four surface pressures each,⁴⁶ as measured with an aluminium Wilhelmy plate; measurements were conducted at 7 and 22 °C. An aluminium Wilhelmy plate was used over a traditional paper due to the low wettability of paper by the DES.

The NR experiments were performed on the FIGARO instrument at the Institut Laue-Langevin using time-of-flight methods.⁴⁷ Data were collected at two incident angles; 0.62 and 3.8°, providing a q range from 0.005–0.18 Å⁻¹. Two surface pressures for each phospholipid and contrast were measured.⁴⁸ As with the XRR measurements, the samples were given at least one hour to equilibrate, kept under an inert atmosphere. All measurements were conducted at 22 °C.

3.3 DATA ANALYSIS

XRR and NR methods have a well documented history for the analysis of the structure of phospholipid monolayers at the air-water interface.⁴⁹ Typically these have involved using a model-dependent analysis method, however, the modelling approaches have varied significantly in the number of layers used, the shape of the layers, the use of interfacial roughness, the parameterisation of constraints

⁴⁶ DLPC: 20, 25, 30 and 35 mN m⁻¹, DMPC: 20, 25, 30 and 40 mN m⁻¹, DPPC: 15, 20, 25 and 30 mN m⁻¹, DMPG: 15, 20, 25 and 30 mN m⁻¹.

⁴⁷ R. A. Campbell *et al.* *Eur. Phys. J. Plus* 126.11 (2011), p. 107.

⁴⁸ DMPC: 20 and 25 mN m⁻¹, DPPC: 15 and 20 mN m⁻¹.

⁴⁹ Mohwald, "Phospholipid and Phospholipid-Protein Monolayers at the Air-Water Interface", op. cit.; Kewalramani *et al.*, "Effects of Divalent Cations on Phase Behavior and Structure of a Zwitterionic Phospholipid (DMPC) Monolayer at the Air-Water Interface", op. cit.; T. M. Bayerl *et al.* *Biophys. J.* 57.5 (1990), pp. 1095–1098; S. J. Johnson *et al.* *Biophys. J.* 59.2 (1991), pp. 289–294; L. A. Clifton *et al.* *Phys. Chem. Chem. Phys.* 14.39 (2012), p. 13569; C. A. Helm *et al.* *EPL* 4.6 (1987), pp. 697–702; J. Daillant,

employed, and even the method by which the reflectometry profile was calculated from the model. Recently, an evaluation of the applicability of different models for surfactant and phospholipid monolayers using NR outlined a view of “best practice”.⁵⁰ However, frequently the constraints employed in the modelling process include the head and tail volume for the phospholipid head and tail groups. These values are taken from a variety of other techniques, some examples are shown in Table 3.1.

Table 3.1 provides a general consensus that the volume of the PC head group is 320–360 Å³, while the PG head group is 289–291 Å³. However, these values were all determined from experiments⁵¹ or simulations⁵² where the head group was interacting with water molecules. It is not clear if this will influence the volume that it occupies, and if that volume will change in the presence of a non-aqueous solvent.⁵³ The charged nature of the zwitterionic and anionic phospholipid head groups may have different interactions with the polar, but neutral water and the charged DES.⁵⁴ Additionally, it is known that, on water, increased surface pressures and the associated Liquid-Expanded to Liquid-Condensed phase transition will lead to a compression of the phospholipid tail volume, compared to the values in Table 3.1,⁵⁵ and that this compaction has not necessarily been accounted for in the literature.⁵⁶

These factors meant that it was necessary to develop a model that was appropriate for the phospholipid chemistry while applying as much of the “best practice” from Campbell *et al.*⁵⁷ as possible, and ensuring that the head and tail group volumes were not constrained parameters. The lack of having these normally constrained parameters meant that it was necessary to consider methods by which the reflectometry measurements could be co-refined, in a similar fashion to contrast variation co-refinement in neutron reflectometry. This could be achieved by the co-refinement of reflectometry measurements at different surface pressures, as the model was appropriate for the phospholipid chemistry, and the different surface pressures were in the same phase.⁵⁸ Therefore the head and tail group volumes will remain constant, and only the surface concentration and tail thickness will vary.

The chemically-constrained model that has been used in this work was implemented in the Python library `refnx`.⁵⁹ The software enables the inclusion of custom model classes that feed parameters into the Abelès model.⁶⁰ Our chemically-consistent model class can be seen in Code Block 3.1, and is shared under a CC BY-SA 4.0 license in the ESI for the associated publication.⁶¹ In order to ensure that the phospholipid chemistry was consistent both within the phospholipid molecule and across the different surface pressures, Code Block 3.2 was implemented.

The chemically-consistent model⁶² consisted of two layers that define the phospholipid monolayer; the head layer at the interface with the solvent and the tail layer at the air interface. The head

⁵⁰ Campbell *et al.*, “Structure of Surfactant and Phospholipid Monolayers at the Air/Water Interface Modeled from Neutron Reflectivity Data”, op. cit.

⁵¹ W.-J. Sun *et al.* *Phys. Rev. E* 49.5 (1994), pp. 4665–4676; N. Kučerka *et al.* *Eur. Biophys. J.* 33.4 (2004), pp. 328–334; P. Balgavý *et al.* *Acta Phys. Slovaca* 51.1 (2001), pp. 53–68; J. Pan *et al.* *BBA - Biomembranes* 1818.9 (2012), pp. 2135–2148.

⁵² R. S. Armen *et al.* *Biophys. J.* 75.2 (1998), pp. 734–744; N. Kučerka *et al.* *J. Phys. Chem. B* 116.1 (2012), pp. 232–239.

⁵³ Such as the DES considered herein.

⁵⁴ A. Sanchez-Fernandez *et al.* *Soft Matter* 14.26 (2018), pp. 5525–5536.

⁵⁵ D. Marsh. *Chem. Phy. Lipids* 163.7 (2010), pp. 667–677; Small, “Lateral Chain Packing in Lipids and Membranes”, op. cit.

⁵⁶ Campbell *et al.*, “Structure of Surfactant and Phospholipid Monolayers at the Air/Water Interface Modeled from Neutron Reflectivity Data”, op. cit.

⁵⁷ Ibid.

⁵⁸ Liquid-Condensed (LC) for DPPC and Liquid-Expanded (LE) for DMPC, DLPC, and DMPG.

⁵⁹ Nelson *et al.*, “Refnx: Neutron and X-Ray Reflectometry Analysis in Python”, op. cit.; Nelson *et al.*, *Refnx v0.1.2*, op. cit.

⁶⁰ Abelès, “Sur La Propagation Des Ondes Électromagnétiques Dans Les Milieux Stratifiés”, op. cit.; Parratt, “Surface Studies of Solids by Total Reflection of X-Rays”, op. cit., discussed in detail in Section 2.2.6.

⁶¹ A. R. McCluskey *et al.* *Lipids_at_airdes (Version 1.0)*. 2019. URL: <http://doi.org/10.5281/zenodo.2577796>.

⁶² That is outlined in Code Block 3.1.

Table 3.1: Phospholipid component volumes extracted from different literature sources. V_t corresponds to the total phospholipid volume, V_i to the tail group volume, V_h to the head group volume, MD to molecular dynamics simulations, WAXS to wide-angle X-ray scattering, NB to neutral buoyancy, and DVTD to differential vibrating tube densimetry. The values for DPPC are from R. S. Armen et al. *Biophys. J.* 75.2 (1998), pp. 734–744; W.-J. Sun et al. *Phys. Rev. E* 49.5 (1994), pp. 4665–4676, and N. Kučerka et al. *Eur. Biophys. J.* 33.4 (2004), pp. 328–334; P. Balgavý et al. *Acta Phys. Slovaca* 51.1 (2001), pp. 53–68 respectively, the values for DMPC are from R. S. Armen et al. *Biophys. J.* 75.2 (1998), pp. 734–744 and N. Kučerka et al. *Eur. Biophys. J.* 33.4 (2004), pp. 328–334; P. Balgavý et al. *Acta Phys. Slovaca* 51.1 (2001), pp. 53–68 respectively, the values for DLPC are from R. S. Armen et al. *Biophys. J.* 75.2 (1998), pp. 734–744 and N. Kučerka et al. *Eur. Biophys. J.* 33.4 (2004), pp. 328–334; P. Balgavý et al. *Acta Phys. Slovaca* 51.1 (2001), pp. 53–68 respectively, the values for DMPG are from J. Pan et al. *BBA - Biomembranes* 1818.9 (2012), pp. 2135–2148, and the values for POPG are from N. Kučerka et al. *J. Phys. Chem. B* 116.1 (2012), pp. 232–239.

Phospholipid	DPPC		DMPC		DLPC		DMPG		POPG
$V_t/\text{\AA}^3$	1287.3 ± 25.5	1148 ± 2	1268.2 ± 32.1	1172.5 ± 25.1	1155.4 ± 30.0	1057.7 ± 24.7	1046.6 ± 28.0	1011.4	1203
$V_i/\text{\AA}^3$	966.4 ± 5.4	829 ± 4	924.7 ± 17.6	851.5 ± 5.0	815.9 ± 15.5	736.8 ± 4.6	707.1 ± 13.5	720.4	914
$V_h/\text{\AA}^3$	320.9 ± 20.1	319 ± 6	339.5 ± 14.5	320.9 ± 20.1	339.5 ± 14.5	320.9 ± 20.1	339.5 ± 14.5	291.0	289
Method	MD	WAXS	NB	MD	NB	MD	NB	DVTD	MD
T/°C	50	24	30	50	30	50	30	20	25

```

import numpy as np
from refnx.analysis import possibly_create_parameter as pcp
from refnx.analysis import Parameters
from refnx.reflect import Component

class VolMono(Component):
    def __init__(self, vol, b, d_h, c_length, name=""):
        super(VolMono, self).__init__()
        t_t = 1.54 + 1.265 * c_length
        self.vol = [
            pcp(vol[0], "{}-V_h".format(name)),
            pcp(vol[1], "{}-V_t".format(name)),
        ]
        self.realb = [
            pcp(b[0].real, name="{}-b_h".format(name)),
            pcp(b[1].real, name="{}-b_t".format(name)),
        ]
        self.imagb = [
            pcp(b[0].imag, name="{}-ib_h".format(name)),
            pcp(b[1].imag, name="{}-ib_t".format(name)),
        ]
        self.d = [
            pcp(d_h, name="{}-d_h".format(name)),
            pcp(t_t * 0.8, name="{}-d_t".format(name)),
        ]
        self.phi = [
            pcp(0.5, name="{}-phi_h".format(name)),
            pcp(0.0, name="{}-phi_t".format(name)),
        ]
        self.sigma = pcp(3.0, name="{}-sigma".format(name))
        self.name = name

    @property
    def slabs(self):
        layers = np.zeros((2, 5))
        layers[0, 0] = self.d[1]
        layers[0, 1] = self.realb[1] * 1.0e16 / self.vol[1]
        layers[0, 2] = self.imagb[1] * 1.0e16 / self.vol[1]
        layers[0, 3] = self.sigma
        layers[0, 4] = self.phi[1]
        layers[1, 0] = self.d[0]
        layers[1, 1] = self.realb[0] * 1.0e16 / self.vol[0]
        layers[1, 2] = self.imagb[0] * 1.0e16 / self.vol[0]
        layers[1, 3] = self.sigma
        layers[1, 4] = self.phi[0]
        return layers

    @property
    def parameters(self):
        """
        Returns
        -------
        Parameter, array_like
            An array of the parameters in the fitting.
        """
        p = Parameters(name=self.name)
        p.extend([
            self.vol[0],
            self.vol[1],
            self.realb[0],
            self.realb[1],
            self.imagb[0],
            self.imagb[1],
            self.d[0],
            self.d[1],
            self.phi[0],
            self.phi[1],
            self.sigma,
        ])
    )

```

Code Block 3.1: The chemically-consistent model class that was implemented in `refnx` A. R. J. Nelson *et al.* *J. Appl. Crystallogr.* 52.1 (2019), pp. 193–200; A. R. J. Nelson *et al.* *Refnx v0.1.2. 2019.* URL: <http://doi.org/10.5281/zenodo.2552023>. The input variables are `vol` which is an array of floats containing the initial values for the head and tail group volumes, `b` which is the calculated scattering length for the head and tail groups, `d_h` which is the initial value for the thickness of the head group region, `c_length` which is the number of carbon atoms in the phospholipid tail, `str` which is the name to be given to the object. The `slabs` function will return an array of floats representing the scattering length density profile.

```

def set_constraints(
    lipids,
    structures,
    hold_tails=False,
    hold_rough=False,
    hold_phih=False,
):
    i = 0
    lipids[i].phi[0].constraint = 1 - (
        lipids[0].vol[0] / lipids[0].vol[1]
    ) * (lipids[i].d[1] / lipids[i].d[0])
    lipids[i].sigma.constraint = structures[i][-1].rough
    for i in range(1, len(lipids)):
        lipids[i].vol[0].constraint = lipids[0].vol[0]
        lipids[i].vol[1].constraint = lipids[0].vol[1]
        lipids[i].d[0].constraint = lipids[0].d[0]
        if hold_tails:
            lipids[i].d[1].constraint = lipids[0].d[1]

```

Code Block 3.2: The `set_constraints` that was used to impose chemical-consistency on the phospholipid monolayer structure.. The input variables are `lipids` and `structures` which are `refnx` objects that contain information about the phospholipids and monolayers, and `hold_tails`, `hold_rough`, and `hold_phih` are Boolean switches to constrain the tail layer thickness, the interfacial roughness, and the volume fraction of solvent across the different measurements, in this work these were all kept as `False`.

groups have a scattering length that can be calculated from a summation of the X-ray or neutron atomic scattering lengths, b_h , and a volume, V_h . These groups make up a layer of a given thickness, d_h , which has some interfacial roughness, σ_h , within which some volume fraction of solvent may penetrate, ϕ_h . The tail layer is defined in the same way, however, the tail thickness, d_t , is constrained such that it can be no greater than the maximum extended length for the phospholipid tail,⁶³ which is given in Table 3.2, and that no solvent may penetrate into the layer.⁶⁴ Therefore, the SLD may be determined as discussed in Equation 3.1. Based on the work of Campbell *et al.*,⁶⁵ a single value for the interfacial roughness was fitted for all of the interfaces, including the subphase,⁶⁶ as there is only a single phospholipid molecule type present in each monolayer. Therefore, any capillary wave roughness at the air-DES interface is carried conformally through the layers. The interfacial roughness was constrained to be greater than 3.3 Å, in agreement with previous work.⁶⁷

⁶³ This is defined as the Tanford length, t_t from C. Tanford. *The Hydrophobic Effect: Formation of Micelles and Biological Membranes*. 1980.

⁶⁴ Such at $\phi_t = 0$.

⁶⁵ Campbell *et al.*, "Structure of Surfactant and Phospholipid Monolayers at the Air/Water Interface Modeled from Neutron Reflectivity Data", op. cit.

⁶⁶ i.e. $\sigma_t = \sigma_h = \sigma_s$.

⁶⁷ Sanchez-Fernandez *et al.*, "Micelization of Alkyltrimethylammonium Bromide Surfactants in Choline Chloride Glycerol Deep Eutectic Solvent", within the chemically-consistent model. op. cit.

Values for t_t were taken from the Tanford formula (C. Tanford. *The Hydrophobic Effect: Formation of Micelles and Biological Membranes*. 1980), and the SLD values for the DES from A. Sanchez-Fernandez *et al.* *Phys. Chem. Chem. Phys.* 18.48 (2016), pp. 33240–33249.

Component	b_t/fm	b_h/fm	$t_t/\text{\AA}$	SLD/ 10^{-6}\AA^{-2}
X-ray				
DPPC	6827	4635	20.5	–
DMPC	5924	4635	18.0	–
DLPC	5021	4635	15.5	–
DMPG	5924	4694	18.0	–
Air	–	–	–	0
DES	–	–	–	10.8
Neutron				
$d_{54}\text{-DMPC}$			18.0	–
$d_{62}\text{-DPPC}$			20.5	–
h-DES	–	–	–	0.43
hd-DES	–	–	–	3.15

The constraints implemented in Code Block 3.2 involved two aspects. The first was to ensure that the number density of head groups and pairs of tail groups was kept the same. This was achieved with the following relation,⁶⁸

$$\phi_h = 1 - \left(\frac{d_t V_h}{V_t d_h} \right). \quad (3.2)$$

The second aspect was to enforce chemically-consistent constraints across the measurements that were conducted at different surface pressures. This was achieved by constraining the head and tail group volumes and the head layer thickness such that they do not vary between the different surface pressure measurements.

The justification for constraining the tail volume is built on the assumption that the phospholipids remain in the same phase. On water, this may be demonstrated with a Langmuir isotherm. However, it was not possible to collect consistent Langmuir isotherm measurements.⁶⁹ Instead, grazing incidence X-ray diffraction was used to confirm the phases of DMPC and DPPC at 30 mN m⁻¹.

⁶⁸ L. Braun *et al.* *Adv. Colloid Interface Sci.* 247 (2017), pp. 130–148.

⁶⁹ Due to the high viscosity of the DES.

Figure 3.2 shows the grazing-incidence X-ray diffraction⁷⁰ data from different phospholipids at different temperatures. Unfortunately, all the patterns show a weak artefact due to scattering from the Teflon trough. However, there are clear $(2, 0)$ diffraction peaks in the GIXD pattern for DPPC at 22 °C and DMPC at 7 °C indicating that both phospholipids are in the LC phase. This peak was also present at other surface pressures (data not shown). The peak position corresponded well with that found for DPPC in water.⁷¹ DMPC at 22 °C showed no evidence of a diffraction peak indicating the presence of the LE phase. It was assumed that DLPC and DMPG were also in the LE phase as there is no reason for the phase behaviour of these systems to differ significantly from that of DMPC at room temperature.

⁷⁰ Abbreviated to GIXD.

⁷¹ E. B. Watkins *et al.* *Phys. Rev. Lett.* 102, 23 (2009), pp. 238101–238104.

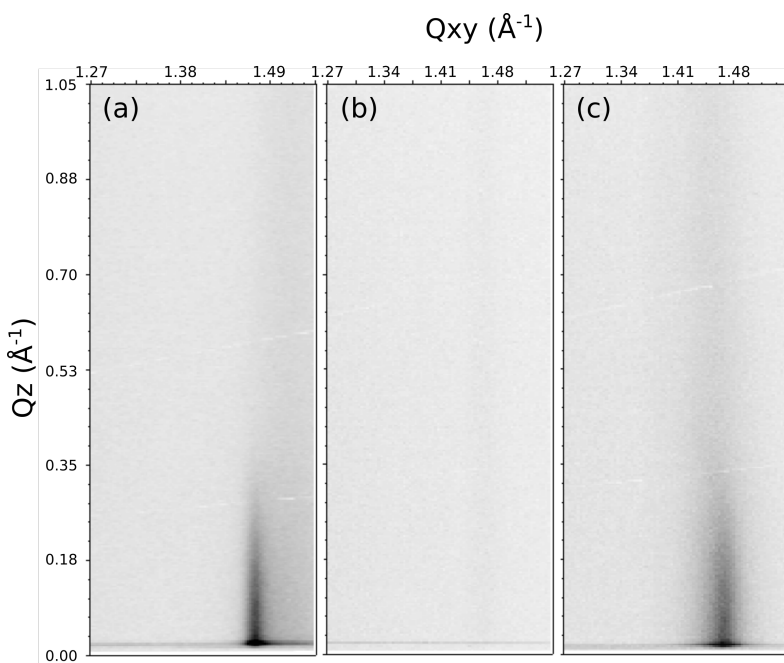


Figure 3.2: The GIXD patterns, where Q_z is the scattering vector normal to the interface and Q_{xy} is that in the plane of the interface; (a) DPPC at 30 mN m^{-1} and 22 °C, (b) DMPC at 30 mN m^{-1} and 22 °C, and (c) DMPC at 30 mN m^{-1} and 7 °C. Note that Q is equivalent to q .

Initially, this chemically-consistent modelling approach was applied only to the XRR data. The tail layer thickness and interfacial roughness were allowed to vary independently across the surface pressures, while the other parameters were constrained as discussed above or held constant to the values given in Table 3.2. For each co-refinement of four XRR measurements, there were, in total, eleven degrees of freedom. Throughout all of the analyses, the intensity scale factor was allowed to vary freely, while the background was constrained to the intensity at the largest q -value.

Following this, the head and tail group volumes, and the head layer thickness that were found from the XRR analysis were used as fixed variables for the refinement of the NR measurements. This reduced the number of fitted parameters in the NR data to two, namely the thickness of the tail layer, d_t , and the interfacial roughness, $\sigma_{t,h,s}$, for the co-refinement of two datasets. Table 3.2

also presents details of the scattering lengths and SLDs used for the NR refinement. Again, the intensity scale factor was allowed to vary freely and the background constrained to the intensity at the largest q -value.

In both the XRR and the NR analysis, the refinement of the chemically-consistent model to the experimental data involved the transformation of the reflectometry calculated from the model and the data into Rq^4 -space, such that the contribution of the Fresnel decay was removed.⁷² The model was then optimised using the differential evolution method that is available within the `scipy` library.⁷³ This refined the parameters to give the best fit to the data. Markov chain Monte Carlo (MCMC) was then used to probe the search-space available to each parameter, given the experimental uncertainty of the data. The MCMC sampling method used was Goodman & Weare's Affine Invariant Ensemble⁷⁴ as implemented in the `emcee` package.⁷⁵ This enabled the determination of the probability distribution for each of the parameters, and therefore the quantification of their inverse uncertainty, given the uncertainty in the experimental data. A Shapiro-Wilk test⁷⁶ was used to determine if the probability distribution function⁷⁷ fitted to a normal distribution and therefore could be considered to have symmetric confidence intervals. If the PDF failed the test the value was quoted with asymmetric confidence intervals, compared with the symmetric confidence intervals given for those that passed the Shapiro-Wilk test. It is important to note that the PDFs and therefore the determined confidence intervals are not true confidence intervals, and account only for the uncertainty that is present in the data.⁷⁸ In addition to determining parameter confidence intervals, it was also possible to use these probability distributions to understand the correlations present between the parameters and the impact this has on the fitting process. The correlation was quantified using the Pearson correlation coefficient,⁷⁹ a common statistical definition for the level of correlation present between two variables. The Pearson correlation coefficient can have values that range from -1 to 1 , with a value of -1 corresponding to a complete negative correlation⁸⁰, while a value of 1 corresponds to a complete positive correlation⁸¹, a value of 0 indicates no correlation between the two variables. The MCMC sampling involved 200 walkers that were used for 1000 iterations, following a burn-in of 200 iterations.

⁷² Gerelli, "Aurore: New Software for Neutron Reflectivity Data Analysis. Corrigendum", op. cit.

⁷³ Jones *et al.*, *SciPy: Open Source Scientific Tools for Python*, op. cit.

⁷⁴ J. Goodman *et al.* *Comm. App. Math. Comp. Sci.* 5 (2010), pp. 65–80.

⁷⁵ Foreman-Mackey *et al.*, "Emcee : The MCMC Hammer", op. cit.

⁷⁶ S. S. Shapiro *et al.* *Biometrika* 52.3-4 (1965), pp. 591–611, this is a commonly test to assess the normality of a distribution.

⁷⁷ Abbreviated to PDF.

⁷⁸ Therefore, they do not account for systematic uncertainty in the measurement technique.

⁷⁹ K. Pearson. *Proc. Royal Soc. Lond.* 58 (1895), pp. 240–242.

⁸⁰ An increase in one variable is associated with a decrease in the other.

⁸¹ An increase in one variable is associated with a similar increase in the other.

3.4 RESULTS & DISCUSSION

3.4.1 X-ray reflectometry

The chemically-consistent model was co-refined across XRR measurements at all four surface pressures for each phospholipid. The resulting XRR profiles and associated SLD profiles are shown in Figure 3.3. Table 3.3 gives the parameters for each of the phospho-

lipids at the second highest surface pressure measured, as well as the details of ϕ_h , as determined from Equation 3.2.⁸²

⁸² The parameters at the other surface pressures may be found in Appendix ??.

Phospholipid SP/mN m ⁻¹	DPPC	DMPC	DLPC	DMPG	Table 3.3: The best-fit values, and associated 95 % confidence intervals for each of the varying parameters
25	30	30	25	25	⁸² For each phospholipid at the second highest surface pressure measured from XRR. The values of ϕ_h were obtained from the appropriate use of Equation 3.2. Surface pressure has been abbreviated to SP.
$V_t/\text{\AA}^3$	765.31 ± 0.38	718.76 ± 0.54	625.50 ± 3.70	734.00 ± 0.58	
$V_h/\text{\AA}^3$	322.00 ± 0.24	339.53 ± 0.27	331.38 ± 0.81	329.96 ± 0.34	
$d_h/\text{\AA}$	$12.70^{+0.03}_{-0.03}$	$13.21^{+0.04}_{-0.04}$	11.00 ± 0.13	13.95 ± 0.03	
$d_t\text{\AA}$	16.83 ± 0.01	13.72 ± 0.01	9.51 ± 0.06	12.24 ± 0.01	
$\sigma_{t,h,s}/\text{\AA}$	4.31 ± 0.00	3.86 ± 0.00	4.16 ± 0.04	3.81 ± 0.00	
$\phi_h \times 10^{-2}$	44.23 ± 0.22	50.94 ± 0.25	54.20 ± 1.10	60.57 ± 0.17	

Following the structural determination of the monolayer from the XRR measurements. NR was used to confirm the values of the head and tail group volumes that had been determined. The resulting NR profiles and associated SLD profiles, at both surface pressures measured can be found in Figure 3.4. Table 3.4 gives the parameters as determined from the NR measurements, along with ϕ_h as determined from Equation 3.2.

3.4.2 Effect of compression on the monolayer thickness

From Tables ??, ??, 3.3, ??, and 3.4, we can see that, as expected and shown in previous work at the air-water interface,⁸³ the thickness of the tail layer increases as the number of carbon atoms in the tail chain increases. Furthermore, the thickness of the tail layers determined here agrees well with values found for water-analogues; $13.72 \pm 0.01 \text{ \AA}$ at 30 mN m^{-1} in DES compared with 15.8 \AA at 30 mN m^{-1} in water for DMPC, and $16.91 \pm 0.01 \text{ \AA}$ at 30 mN m^{-1} in DES compared with 16.7 \AA at 40 mN m^{-1} in water for DPPC.

⁸³ Mohwald, "Phospholipid and Phospholipid-Protein Monolayers at the Air-Water Interface", op. cit.; D. Vaknin *et al.* *Biophys. J.* 59.6 (1991), pp. 1325–1332.

The variation of the tail layer thickness in the models with surface pressure is given for each phospholipid in Figure 3.5. For all of the phospholipids, as the surface pressure increases, the thickness of the tail layer also increases to a point before plateauing; for DPPC this occurs at 20 mN m^{-1} , DMPC at 30 mN m^{-1} , and for DMPG and DLPC can be assumed to be at higher pressures than those studied. This relationship of increasing tail layer thickness with increasing surface pressure has been noted previously for DMPC⁸⁴ and DPPC⁸⁵ at the air-water interface. This can be easily understood as the angle of the tail group with respect to the surface normal decreasing as the surface pressure increases.

⁸⁴ Bayerl *et al.*, "Specular Reflection of Neutrons at Phospholipid Monolayers. Changes of Monolayer Structure and Headgroup Hydration at the Transition from the Expanded to the Condensed Phase State", op. cit.

Phospholipid SP/mN m ⁻¹	DPPC	DPPC	DMPC	DMPC
15	20	20	25	
$d_t\text{\AA}$	12.67 ± 0.13	15.43 ± 0.08	14.81 ± 0.13	$17.98^{+0.01}_{-0.03}$
$\sigma_{t,h,s}/\text{\AA}$	4.77 ± 0.16	$3.31^{+0.04}_{-0.01}$	3.47 ± 0.15	$3.30^{+0.02}_{-0.00}$
$\phi_h \times 10^{-2}$	58.04 ± 0.44	48.86 ± 0.26	47.06 ± 0.48	$35.71^{+0.11}_{-0.03}$

⁸⁵ Geng *et al.*, "Structure of Surface-tension Phospholipid Monolayers at the Air-Water Interface Modelled from Neutron Reflectivity Data", at surface pressure from NR. The values of ϕ_h were obtained from the appropriate use of Equation 3.2.

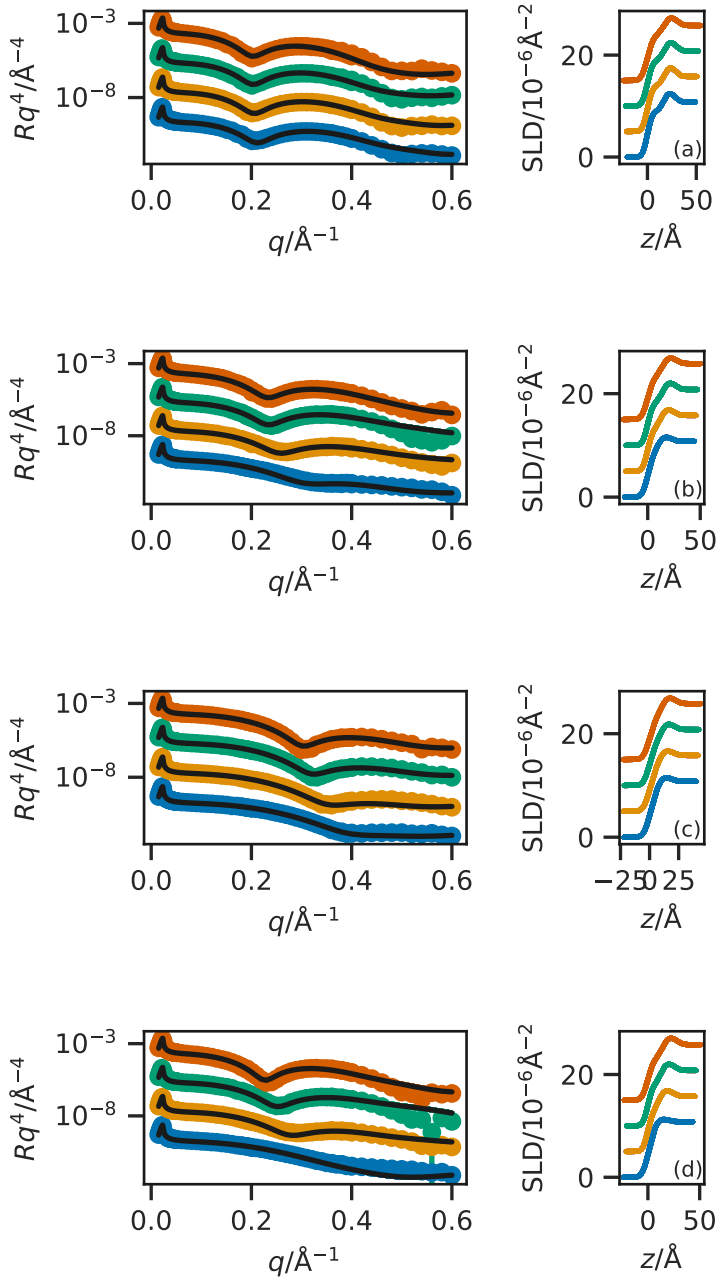


Figure 3.3: The XRR profiles (left) and SLD profiles (right) for each of the four phospholipids; (a) DPPC, (b) DMPC, (c) DLPC, and (d) DMPG, at the four measured surface pressures; increasing in surface pressure from blue, orange, green to red. The different surface pressure XRR profiles have been offset in the y -axis by two orders of magnitude and the SLD profiles offset in the y -axis by $5 \times 10^{-6} \text{\AA}^{-2}$, for clarity.

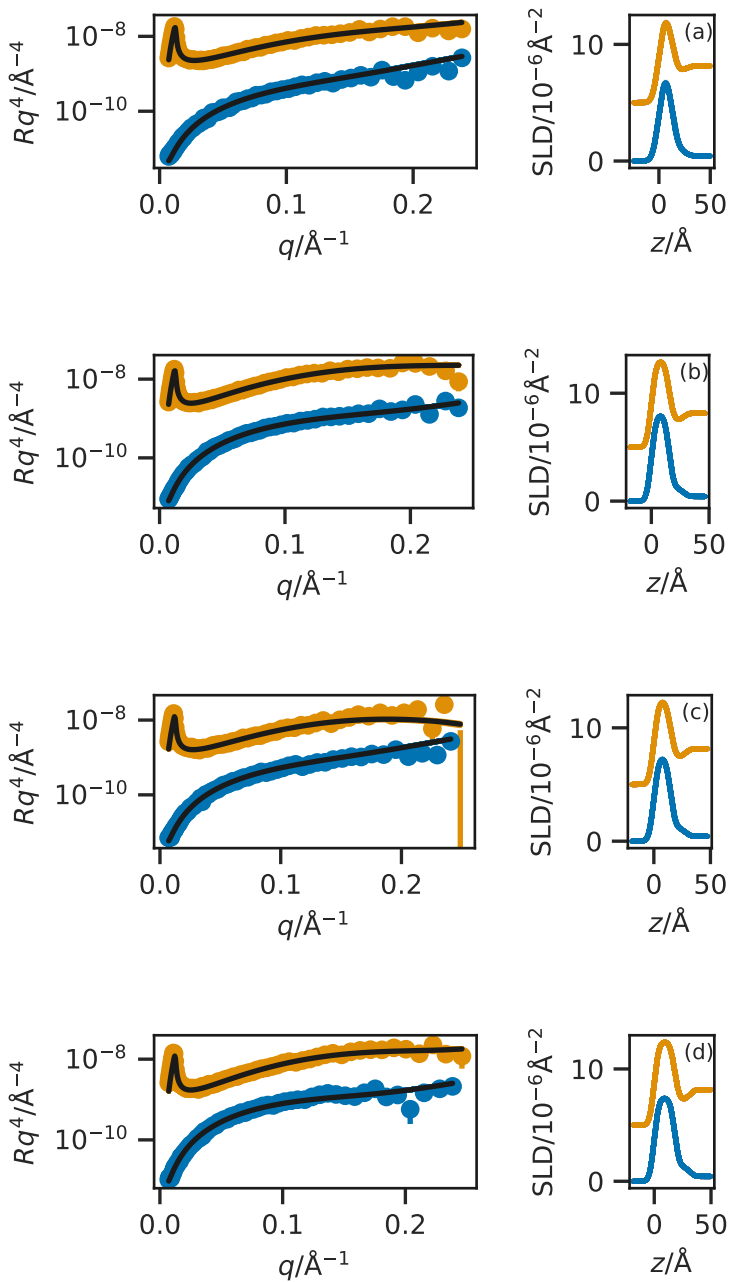


Figure 3.4: The NR profiles (left) and SLD profiles (right) for each of the four phospholipids; (a) DPPC at 15 mN m^{-1} , (b) DPPC at 20 mN m^{-1} , (c) DMPC at 20 mN m^{-1} , and (d) DMPC at 25 mN m^{-1} , where the blue data indicates the h-DES contrast, while the orange is the hd-DES. The different surface pressure XRR profiles have been offset in the y -axis by an order of magnitude and the SLD profiles offset in the y -axis by $5 \times 10^{-6} \text{ \AA}^{-2}$, for clarity.

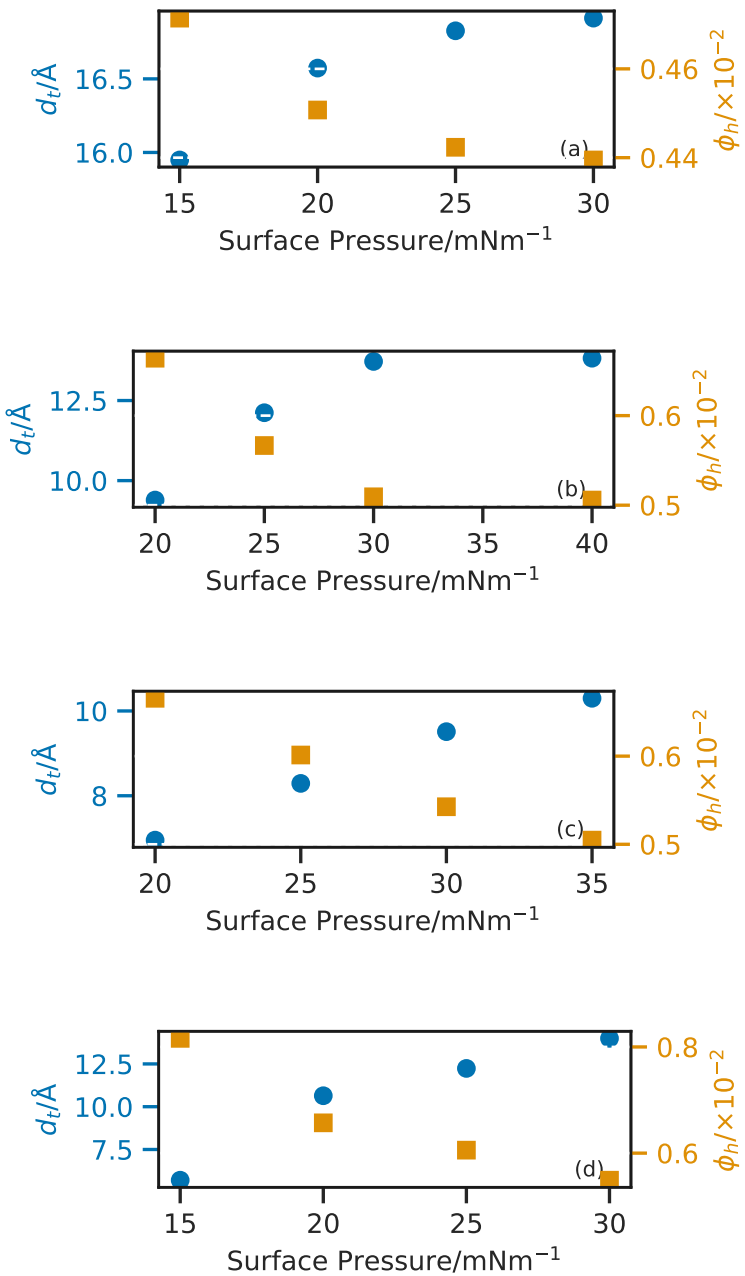


Figure 3.5: The variation of tail layer thickness, d_t , (blue circles) and head group solvation, ϕ_h , (orange squares) with surface pressures for each of the four phospholipids; (a) DPPC, (b) DMPC, (c) DLPC, and (d) DMPG.

3.4.3 Effect of compressure on solvent fraction

In Figure 3.5, it is clear that for all four phospholipids, as the surface pressure is increased there is a corresponding reduction in the volume fraction of solvent in the phospholipid head layer. This can be rationalised by considering that when the surface pressure is increased, there is a corresponding increase in surface concentration, hence the free volume available to the solvent is less. A similar effect has been observed when increasing the surface pressure from 11 mN m^{-1} to 31 mN m^{-1} for a mixed DMPC/DMPG monolayer at the air-water interface.⁸⁶

3.4.4 Effect of compression on the phospholipid tail component volumes

It can be seen from comparing Table 3.1 with Tables ??, ??, 3.3, and ?? that the volumes of the phospholipid tails are substantially lower in the current measurement than found previously, by other techniques. It is unlikely that this is a result of the DES subphase, due to the solvophobic nature of these tail groups. However, a similar reduction has been shown previously,⁸⁷ where it was rationalised by the compaction of the monolayer at elevated surface pressure. In that work, the optimal value for the tail group volume of DPPC was found to be 772 \AA^3 at a surface pressure of 35 mN m^{-1} , which agrees well with the value of $765.31 \pm 0.38 \text{ \AA}^3$ found in this work at surface pressures of $15, 20, 25$ and 30 mN m^{-1} . The reduction in tail volume was found to be between 8-12 % for DPPC, DMPC, DLPC when compared with the literature sources at 24 and 30°C . This is close to the maximum compression of 15 % noted by Small.⁸⁸ DMPG shows a small increase in the tail volume when compared with the literature value, albeit at a higher temperature. However, this value agrees well with that found for DMPC which shares the same tail structure.

3.4.5 Solvent effect on the phospholipid head group volume

Tables ??, ??, 3.3, and ?? give the best-fit values for the head group volumes for each of phospholipids investigated. Ths three phospholipids with the PC head group are consistent, giving values of $\sim 330 \text{ \AA}^3$, regardless of the tail group. This agrees well with the values found for the same head component in water, shown in Table 3.1. Interestingly, the head group volume determined for the PG containing phospholipid is similar to that for the PC head group, with a value of $329.96 \pm 0.34 \text{ \AA}^3$. The PG head group volume in water from either DMPG using differential vibrating tube densimetry⁸⁹ or POPG using molecular dynamics simulations,⁹⁰ is noticeably smaller. This indicates that there may be some effect arising from the solvation of the PG component in the choline chloride:glycerol DES. However, this has only been shown for a single

⁸⁶ Bayerl *et al.*, "Specular Reflection of Neutrons at Phospholipid Monolayers. Changes of Monolayer Structure and Headgroup Hydration at the Transition from the Expanded to the Condensed Phase State", op. cit.

⁸⁷ Campbell *et al.*, "Structure of Surfactant and Phospholipid Monolayers at the Air/Water Interface Modeled from Neutron Reflectivity Data", op. cit.

⁸⁸ Small, "Lateral Chain Packing in Lipids and Membranes", op. cit.

⁸⁹ Pan *et al.*, "Molecular Structures of Fluid Phase Phosphatidylglycerol Bilayers as Determined by Small Angle Neutron and X-Ray Scattering", op. cit.

⁹⁰ Kučerka *et al.*, "Scattering Density Profile Model of POPG Bilayers As Determined by Molecular Dynamics Simulations and Small-Angle Neutron and X-Ray Scattering Experiments", op. cit.

PG-lipid at the air-DES interface.

The major difference between the two head groups of the phospholipid is that the PG is present as a sodium salt, whereas the PC is zwitterionic. When in solution the anionic PG head is expected to associate with cations in solution, as it does in water⁹¹ where such interactions depend on a variety of factors including the ionic strength. In the case of a DES, the environment is inherently ionic and therefore the interaction of an anionic phospholipid head may be more complex. As well as interacting with this sodium, the head is likely to interact with the choline cations, similar to behaviour reported previously for surfactant micelles.⁹² The extent of interaction with each of the cations is unclear, but regardless it seems likely that the solvation of the PG head is improved in the DES relative to water. This better solvation would explain the apparent increase in the volume of the PG head since it would result in a swelling of this group through its strong interactions with the solvent. In the case of PC, the proximity of a local cation within the molecule results in the same folding of the head group seen in water because this interaction is less transient than the equivalent interactions with the solvent.

3.4.6 Analysis of neutron reflectometry

The ability to fit NR data in Figure 3.4 indicated that the values found for the head and tail groups are consistent between the pair of measurements for the same systems. It is clear that again stable monolayers of the phospholipids are forming at the air-DES interface and that the volumes determined by XRR measurements are robust enough to be used in the modelling of NR data. Furthermore, as shown in Table 3.4, the trends observed with increasing surface pressure in the XRR models, pertaining to a responsive increase in tail thickness and a decrease in solvent concentration in the head layer are consistent with that found with the NR analysis.

3.4.7 Utility of Markov chain Monte Carlo sampling

The use of MCMC sampling enabled the inverse uncertainties for each of the fitted parameters to be determined as a confidence interval from the PDFs. The PDFs for DLPC are shown in Figure 3.6.⁹³ These confidence intervals are useful for understanding the probability of the given value, however as discussed in Section 3.3 these intervals only represent the uncertainty in the experimental data and do not account for systematic uncertainty present in the measurement method.

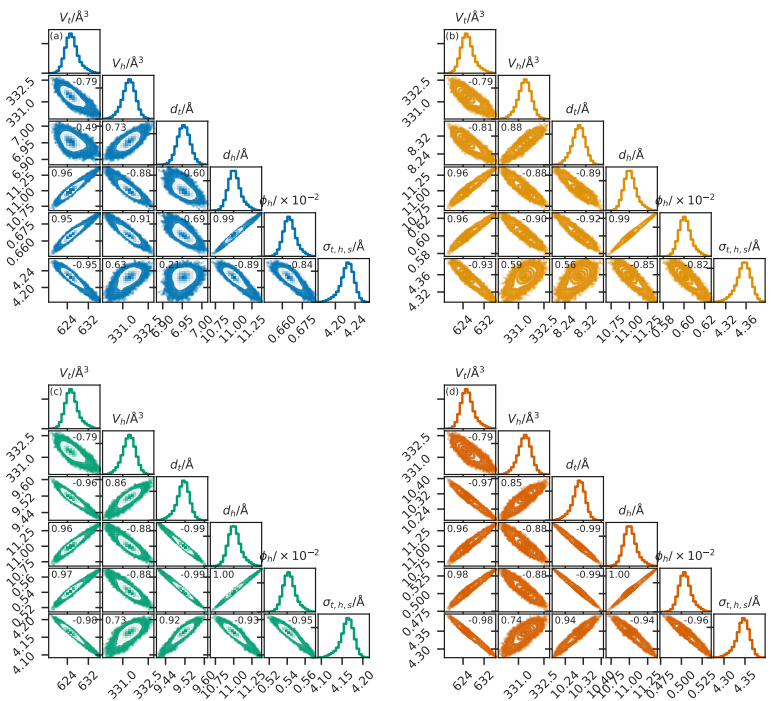
The sums of the magnitudes of the Pearson correlation coefficients for each PC-containing phospholipids at each surface pressures are given in Figure 3.7. From this figure, it is clear that there is a relationship between the phospholipid and the correlation present in the reflectometry model due to the skewed

⁹¹ D. Grigoriev *et al.* *J. Phys. Chem. B* 103.6 (1999), pp. 1013–1018.

⁹² A. Sanchez-Fernandez *et al.* *Phys. Chem. Chem. Phys.* 20.20 (2018), pp. 13952–13961.

⁹³ Those for the other phospholipid-XRR and NR measurements can be found in Appendix ??.

Figure 3.6: The probability distribution functions from the chemically-consistent modelling of DLPC; (a) at 20 mN m⁻¹, (b) at 25 mN m⁻¹, (c) at 30 mN m⁻¹, (d) at 35 mN m⁻¹. The Pearson correlation coefficient for each pair of parameters is given in the top corner of each two-dimensional PDF.



two-dimensional probability distribution. This is the effect of the reduction in the phospholipid length from DPPC to DLPC, and that a corresponding decrease is not observed for the interfacial roughness. Therefore, the boundary between phospholipid head and tail layers is less well defined.⁹⁴ Furthermore, the magnitude of the Pearson correlation between the head and tail thicknesses increases with increasing tail length; from -0.89 for DPPC, to -0.92 for DMPC, to -0.99 for DLPC, each at 30 mN m⁻¹. Indicating that as the phospholipid tail length decreases, the negative correlation between the head and tail layers increases to the point for DLPC where the two variables are almost completely correlated and the boundary between the head and the tail is nearly nonexistent due to the magnitude of the interfacial roughness.

⁹⁴ As can be observed by investigating the SLD profiles in Figure 3.3.

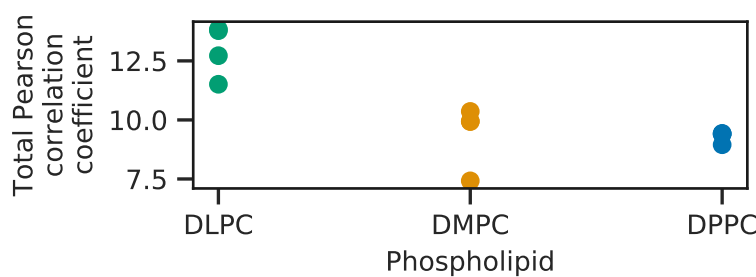


Figure 3.7: The sum of the magnitudes for each of the Pearson correlation coefficients for each of the PC-containing lipids.

There is also a substantial positive correlation present for all of

⁹⁵ Which can be as much as 78 % solvent by volume.

the datasets between the phospholipid head layer thickness and the volume fraction of solvent in the head layer. This correlation can be rationalised as a result of the SLD of the solvent and the head layer⁹⁵ being similar, and therefore the boundary between the head layer and the solvent is also poorly defined. A significant correlation such as this is unavoidable, without considering the use of many neutron contrasts for both the phospholipid and the solvent, due to the highly solvophilic nature of the head groups.

3.5 CONCLUSIONS

Stable PC and PG lipid monolayers were observed and characterised on an ionic solvent surface. Until the emergence of ionic liquids and DES, only a limited number of molecular solvents exhibited the ability to promote self-assembly and only water and formamide among those had previously demonstrated the formation of phospholipid monolayers at the air-liquid interface.⁹⁶

For the first time, a physically and chemically-consistent reflectometry modelling approach was used to co-refine XRR measurements at different surface pressures. This enabled modelling without the need to constrain the head and tail group volumes, enabling these parameters to vary freely to account for any variation occurring due to the elevated surface pressures used or the presence of a non-aqueous solvent, compared to the commonly applied literature values. This allows a significant difference in the PG head group volume to be observed; having a larger volume than observed for the same system in water. This suggests that the transfer of phospholipids to a DES is not just a simple substitution of the subphase. In this specific case, we have proposed an explanation based on the dissociation of the PG head group salt and the subsequent interaction with the DES.

Finally, MCMC sampling was used to understand the inverse uncertainties present in the modelling parameters, enabling a confidence interval to be quoted alongside the most probable value. The use of MCMC sampling also allowed the quantification of the correlations between the parameters of the chemically-consistent model. This shows the significant correlations between the head layer thickness and the volume fraction of solvent, and the head layer thickness and the tail layer thickness that becomes more prominent for short-tailed phospholipids. The quantification of these correlations gives us a better understanding of the uncertainties on the parameters and can be rationalised based on the chemistry of the monolayers.

⁹⁶ Mohwald, "Phospholipid and Phospholipid-Protein Monolayers at the Air-Water Interface", op. cit.; Graner *et al.*, "Phospholipidic Monolayers on Formamide", op. cit.

4

APPLYING ATOMISTIC AND COARSE-GRAINED SIMULATION TO REFLECTOMETRY ANAL- YSIS

ABSTRACT

The use of molecular simulation to aid in the analysis of neutron reflectometry measurements has become commonplace. However, reflectometry is a tool to probe large-scale structures, and therefore the use of all-atom simulation may be irrelevant. This work presents the first direct comparison between the reflectometry profiles obtained from different all-atom and coarse-grained molecular dynamics simulations and the reflectometry profiles from a chemically-consistent layer-based modelling method. We find that systematic limitations reduce the efficacy of the MARTINI potential model, while the Berger united-atom and Slipids all-atom potential models agree similarly well with the experimental data. The chemically-consistent layer model gives the best agreement, however, the higher resolution simulation-dependent methods produce an agreement that is comparable.

CONTEXT

This chapter builds on the previous chapter, by using the traditional, highly coarse-grained, chemically-consistent layer-based model as a point of comparison with classical molecular simulations that use a variety of simulation grain-sizes, from the coarse-grained MARTINI potential model, to the all-atom Slipids. Therefore, the analysis in this chapter applies significantly more constraints on the system, however, the constraints are built on substantial underlying chemistry, given their grounding in the potential models. It is hoped that this work will provide an advisory document to those interested in applying classical simulation to the analysis of their neutron reflectometry experiments. Furthermore, the simulations are used to advise on ways that the chemically-consistent models may be improved in the future. It is noted again

that the focus of this chapter is the methodological developments, rather than the particular chemical system to which they are applied.

4.1 INTRODUCTION

The use of a traditional, layer-based model approach¹ is a powerful tool to understand the structure of complex systems such as biomimetic bacterial membranes² and polymeric energy materials.³ These layers structures are typically defined by the underlying chemistry of the system. However, there has been growing interest in the use of molecular dynamics simulations to inform the development of these layer structures. This is due to the fact that the equilibrium structures for soft matter interfaces, that are often of interest in reflectometry studies, are accessible on all-atom simulation timescales.⁴ However, there has been no work that directly compares different levels of simulation coarse-graining in order to assess the required resolution for the accurate reproduction of a given neutron reflectometry profile.

Simulation-driven multi-modal analysis has been applied previously, either by the calculation of the SLD profile from the simulation or by the full determination of the reflectometry profile. In the former case, the calculated SLD profile may be compared with the SLD profile determined from the use of a traditional analysis method. Bobone *et al.* used such a method to study the antimicrobial peptide trichogin GA-IV within a supported phospholipid bilayer.⁵ A four-layer model consisting of the hydrated SiO₂ layer, an inner phospholipid head-region, a phospholipid tail-region, and an outer phospholipid head region was used in the Abelès matrix formalism. The SLD profile from the MD simulations agreed well with that fitted to the reflectometry data from the layer model.

The reflectometry profile was determined explicitly from the classical simulation in the works of Miller *et al.* and Anderson and Wilson.⁶ In these studies, an amphiphilic polymer at the oil-water interface was simulated by Monte Carlo and MD respectively, and the neutron reflectometry profile was found by splitting the simulation cell into a series of small layers and treating these layers with the Abelès formalism. There was good agreement between the experimental and calculated reflectometry, for low interfacial coverages of the polymer. Another study that has made a direct comparison between the atomistic simulation-derived reflectometry data and those measured experimentally includes that of Darré *et al.*⁷ In this work, NeutronRefTools was developed to produce the neutron reflectometry profile from an MD simulation. The particular system studied was a supported DMPC phospholipid bilayer, with good agreement found between the simulation-derived profile and the associated experimental measurements. However, the nature of the support required that a correction for the head group hydration be imposed to achieve this agreement.

Koutsoubas used the MARTINI coarse-grained representation of a DPPC phospholipid bilayer to compare with experimental reflectometry.⁸ This work shows that the parameterisation of the

¹ As is outlined in Chapter 3.

² R. D. Barker *et al.* "Neutron Reflectivity as a Tool for Physics-Based Studies of Model Bacterial Membranes". In: *Biophysics of Infection*. 2016, pp. 261–282.

³ S. Khodakarimi *et al.* *J. Mater. Sci. Mater. Electron.* 27.1 (2016), pp. 182–190.

⁴ Scoppola *et al.*, "Combining Scattering and Computer Simulation for the Study of Biomolecular Soft Interfaces", op. cit.

⁵ S. Bobone *et al.* (*BBA - Biomembranes* 1828.3 (2013), pp. 1013–1024).

⁶ Miller *et al.*, "Monte Carlo Simulations of an Amphiphilic Polymer at a Hydrophobic/Hydrophilic Interface", op. cit.; Anderson *et al.*, "Molecular Dynamics Simulations of Amphiphilic Graft Copolymer Molecules at a Water/Air Interface", op. cit.

⁷ L. Darré *et al.* *J. Chem. Theory Comput.* 11.10 (2015), pp. 4875–4884.

⁸ Koutsoubas, "Combined Coarse-Grained Molecular Dynamics and Neutron Reflectivity Characterization of Supported Lipid Membranes", op. cit.

⁹ A. V. Hughes *et al.* *Acta Crystallogr. D* 72.12 (2016), pp. 1227–1240.

MARTINI water bead was extremely important in the reproduction of the reflectometry data, as the non-polarisable water bead would freeze into crystalline sheets resulting in artefacts in the reflectometry profiles calculated. The work of Hughes *et al.* studied again a DPPC phospholipid bilayer system,⁹ albeit an all-atom representation, that was compared with a supported DPPC phospholipid bilayer system measured with polarised neutron reflectometry. The SLD profile found from MD simulation was varied to better fit the experimental measurement, resulting in good agreement. Additionally, the ability to vary the SLD profile was used to remove an anomalous difference present in the SLD, that arose when the MD simulations were merged with an Abelès layer model. This was done to account for regions present in the experiment that were not modelled explicitly.

In all the examples discussed so far, there is no direct comparison between the reflectometry profile determined from simulation and that from the application of a traditional modelling approach. Indeed, the only example,¹⁰ where a direct comparison was drawn is the work of Dabkowska *et al.*¹¹ This work compares the reflectometry profile from a DPPC monolayer at the air-water interface containing dimethyl sulfoxide molecules with a similar molecular dynamics simulation using the CHARMM potential model. The use of multimodal analysis allowed the determination of the position and orientation of dimethyl sulfoxide molecules at a particular region within the monolayer.

The previously mentioned work of Koutsoubas involved the use of the MARTINI coarse-grained force field to simulations the DPPC bilayer system.¹² The use of atomistic simulation for soft matter systems, such as a phospholipid bilayer, is undesirable as this requires a huge number of atoms to be simulated, due to the large lengths scales involved. The purpose of simulation coarse-graining is to reduce the number of particles over which the forces must be integrated, additionally by removing the higher frequency bond vibrations, the simulation timestep can also be increased.¹³ Together, these two factors enable an increase in both simulation size and length. The use of the MARTINI 4-to-1 coarse-grained and the Berger united atom¹⁴ potential models are particularly pertinent for the application to phospholipid simulations as both were developed with this specific application in mind.¹⁵

The MARTINI potential model involves integrating the interactions of every four heavy atoms¹⁶ into beads of different chemical nature. This potential model attempts to simplify the interactions of phospholipid and protein molecules significantly by allowing for only eighteen particle types, defined by their polarity, charge, and hydrogen-bond acceptor/donor character, which are discussed in detail in the work of Marrink *et al.*¹⁷ This coarse-grained potential model was initially developed for the simulation of a phospholipid bilayer, and proteins held within and therefore is parameterised

¹⁰ To the author's knowledge.

¹¹ Dabkowska *et al.*, "Modulation of Dipalmitoylphosphatidylcholine Monolayers by Dimethyl Sulfoxide", op. cit.

¹² Koutsoubas, "Combined Coarse-Grained Molecular Dynamics and Neutron Reflectivity Characterization of Supported Lipid Membranes", op. cit.

¹³ Pluhackova *et al.*, "Biomembranes in Atomistic and Coarse-Grained Simulations", op. cit.

¹⁴ Where hydrogen atoms are integrated into the heavier atoms to which they are bound.

¹⁵ Marrink *et al.*, "The MARTINI Force Field: Coarse Grained Model for Biomolecular Simulations", op. cit.; O. Berger *et al.* *Biophys. J.* 72.5 (1997), pp. 2002–2013.

¹⁶ Larger than hydrogen.

¹⁷ Marrink *et al.*, "The MARTINI Force Field: Coarse Grained Model for Biomolecular Simulations", op. cit.

well under these conditions. It has successfully been used to simulate a wide range of systems, such as DNA nucleotides,¹⁸ the micellisation of zwitterionic and nonionic surfactants,¹⁹ and the self-assembly of ionic surfactants.²⁰

Increasing the simulation resolution gives an united-atom potential mode, where all of the hydrogen atoms are integrated into the heavier atoms to which they are bound. One of the most popular united-atom potential models for phospholipid simulations is that developed by Berger *et al.*²¹ The Berger parameters were optimised to reproduce phospholipid density and area per phospholipid, the latter of which is often an important parameter for the understanding of reflectometry profiles. Since it's inception, this potential model has proven one of the most commonly used and resilient sets of phospholipid parameters, with the original paper being cited 1500 times at the time of writing. Applications of this potential model have mostly been focussed on the simulation of membrane-bound proteins in a phospholipid bilayer.²²

The Slipid²³ potential model was developed in 2012 by Jämbeck and Lyubartsev,²⁴ where the potential model was again designed to reproduce the structure of a phospholipid bilayer. The authors optimised the average area per phospholipid, the thermal expansivity, and contractivity, among other structural and thermodynamic parameters. This included comparing the X-ray reflectometry profiles of the phospholipid bilayers with those measured experimentally. In later work, additional parameters were optimised to agree well with experimental values.²⁵ Similar to the application of the Berger potential model, the Slipid potential model has been applied to the study of membrane-protein bound systems, such as the modulation of ion transfer.²⁶ However, it has also been used for the study of water diffusion within phospholipid membranes.²⁷

It is clear that there is substantial interest in the use of classical simulation, and coarse-graining, for the analysis of neutron reflectometry data. However, there has been no work to investigate whether the use of atomistic simulations gives more detail than is required to reproduce the reflectometry profile accurately or to assess whether the application of a coarse-grained representation is suitable to aid in analysis. This chapter presents the comparison of three MD simulations of different potential models, with different degree of coarse-graining; namely the Slipid all-atom,²⁸ Berger united-atom,²⁹ and MARTINI coarse-grained potential models. Marrink *et al.*, "The MARTINI Force Field: Coarse Grained Model for Biomolecular Simulations", op. cit. This comparison offers a fundamental insight into the simulation resolution that is necessary to reproduce experimental neutron reflectometry measurements. Furthermore, the highest resolution simulations are used to suggest possible adjustments that may be made to the traditional, layer models that are commonly used to analyse these measurements.

¹⁸ J. J. Uusitalo *et al.* *J. Chem. Theory Comput.* 11.8 (2015), pp. 3932–3945.

¹⁹ S. A. Sanders *et al.* *J. Chem. Phys.* 132.11 (2010), p. 114902.

²⁰ S. Wang *et al.* *Langmuir* 31.4 (2015), pp. 1262–1271.

²¹ Berger *et al.*, "Molecular Dynamics Simulations of a Fluid Bilayer of Dipalmitoylphosphatidylcholine at Full Hydration, Constant Pressure, and Constant Temperature", op. cit.

²² D. P. Tieleman *et al.* *J. Phys. Condens. Matter* 18.28 (2006), S1221–S1234; A. Cordoní *et al.* *J. Chem. Theory Comput.* 8.3 (2012), pp. 948–958.

²³ A shortening of Stockholm Lipids, after the University at which the potential model was developed.

²⁴ J. P. M. Jämbeck *et al.* *J. Phys. Chem. B* 116.10 (2012), pp. 3164–3179.

²⁵ J. P. M. Jämbeck *et al.* *J. Chem. Theory Comput.* 8.8 (2012), pp. 2938–2948; J. P. M. Jämbeck *et al.* *J. Chem. Theory Comput.* 9.1 (2013), pp. 774–784.

²⁶ E. Segala *et al.* *J. Med. Chem.* 59.13 (2016), pp. 6470–6479.

²⁷ Y. von Hansen *et al.* *Phys. Rev. Lett.* 111.11 (2013), pp. 118103–118105.

²⁸ Jämbeck *et al.*, "Derivation and Systematic Validation of a Refined All-Atom Force Field for Phosphatidylcholine Lipids", op. cit.

²⁹ Berger *et al.*, "Molecular Dynamics Simulations of a Fluid Bilayer of Dipalmitoylphosphatidylcholine at Full Hydration, Constant Pressure, and Constant Temperature", op. cit.

4.2 METHODS

4.2.1 Neutron reflectometry measurements

³⁰ Hollinshead *et al.*, “Effects of Surface Pressure on the Structure of Distearoylphosphatidylcholine Monolayers Formed at the Air/Water Interface”, op. cit., full details of the experimental methods used can be found in that publication.

³¹ Abbreviated to DSPC.

³² The different lipid constants are abbreviated to h-DSPC, d₁₃-DSPC, d₇₀-DSPC, and d₈₃-DSPC respectively.

³³ Abbreviated to D₂O and ACMW respectively.

The neutron reflectometry measurements analysed in this chapter were published previously by Hollinshead *et al.*³⁰ These measurements concern the study of a monolayer of 1,2-distearoyl-sn-phosphatidylcholine³¹ at the air-water interface. The neutron reflectometry measurements were conducted on seven isotopic contrasts of the phospholipid and water. These contrasts were made up from four phospholipid types; fully-hydrogenated phospholipid, head-deuterated phospholipid, tail-deuterated phospholipid, and fully-deuterated phospholipid,³² were paired with two water contrasts; fully-deuterated water and air-contrast matched water,³³ where D₂O and H₂O are mixed such that the SLD is zero. The pairing of the fully-hydrogenated phospholipid with ACMW was not performed, due to the lack of scattering available from such a system. Measurements were conducted at four different surface pressures; 20, 30, 40 and 50 mN m⁻¹. Table 4.1 outlines the shorthands used to refer to the different contrast pairings in this work.

Table 4.1: The different contrasts of phospholipid monolayer and water investigated.

Shorthand	Phospholipid contrast	Water contrast
h-D ₂ O	h-DSPC	D ₂ O
d ₁₃ -D ₂ O	d ₁₃ -DSPC	D ₂ O
d ₁₃ -ACMW	d ₁₃ -DSPC	ACMW
d ₇₀ -D ₂ O	d ₇₀ -DSPC	D ₂ O
d ₇₀ -ACMW	d ₇₀ -DSPC	ACMW
d ₈₃ -D ₂ O	d ₈₃ -DSPC	D ₂ O
d ₈₃ -ACMW	d ₈₃ -DSPC	ACMW

4.2.2 Molecular dynamics simulations

³⁴ Jämbek *et al.*, “Derivation and Systematic Validation of a Refined All-Atom Force Field for Phosphatidylcholine Lipids”, op. cit.

³⁵ H. J. C. Berendsen *et al.* *J. Phys. Chem.* 91.24 (1987), pp. 6269–6271, abbreviated to SPC.

³⁶ S. Miyamoto *et al.* *J. Comput. Chem.* 13.8 (1992), pp. 952–962; B. Hess. *J. Chem. Theory Comput.* 4.1 (2008), pp. 116–122.

³⁷ Berger *et al.*, “Molecular Dynamics Simulations of a Fluid Bilayer of Dipalmitoylphosphatidylcholine at Full Hydration, Constant Pressure, and Constant Temperature”, op. cit.

³⁸ It is noted that these timesteps are shorter than those typically used for both forcefields, and that timesteps of up to 2 fs have been applied previously.

³⁹ Marrink *et al.*, “The MARTINI Force Field: Coarse Grained Model for Biomolecular Simulations”, op. cit.

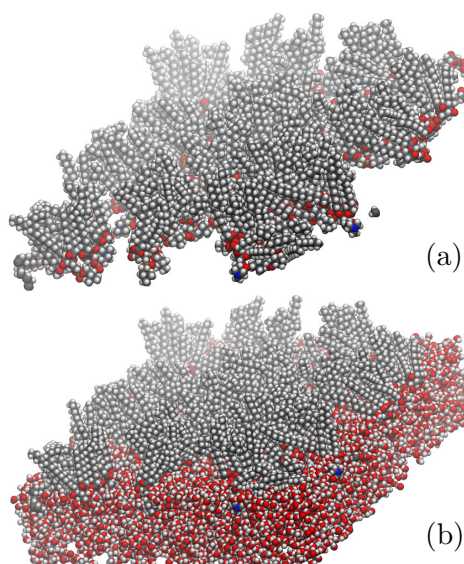
⁴⁰ S. O. Yesylevskyy *et al.* *PLoS Comput. Biol.* 6.6 (2010). Ed. by M. Levitt, e1000810.

⁴¹ Koutsoubas, “Combined Coarse-

The DSPC monolayer simulations were made up of phospholipid molecules modelled with three potential models, each with a different degree of coarse-graining. The Slipids potential model is an all-atom representation of the phospholipid molecules,³⁴ which was used alongside the single point charge water model,³⁵ with a timestep of 0.5 fs, the SHAKE, RATTLE, and PLINCS methods were used to constrain the C–H bond.³⁶ The Berger potential model is obtained by the integration of the hydrogen atoms into the heavy atoms to which they are bound, producing a united-atom potential model;³⁷ again the SPC water molecules were used. This potential model was simulated with an increased timestep of 1 fs.³⁸ Finally, the lowest resolution potential model used was the MARTINI³⁹ alongside the polarisable MARTINI water model,⁴⁰ to avoid the freezing issues observed previously.⁴¹ The MARTINI 4-to-1 heavy atom beading allows for the use of a 20 fs timestep. For the Slipids and Berger potential model simulations a short-range cut-off of 10 Å was used, while for the MARTINI potential model simulations

the cut-off was extended to 15 Å. All simulations were conducted with temperature coupling to a heat bath at 300 K and a leapfrog integrator, and run using GROMACS 5.0.5⁴² on 32 cores of the STFC Scientific Computing resource SCARF. The simulations were of monolayers, therefore the Ewald 3DC correction was applied to allow for the use of x/y -only periodic boundary condition.⁴³ A close-packed “wall” of non-interacting dummy atoms was placed at each side of the simulation cell in the z -direction, to ensure that the atoms could not leave the simulation cell.

The starting simulation structure was generated using the molecular packing software Packmol.⁴⁴ This was used to produce a monolayer of 100 DSPC molecules, with the head group oriented to the bottom of the simulation cell. A 6 Å layer of water was then added such that it overlapped the head groups, this was achieved with the solvate functionality in GROMACS 5.0.5. Examples, of the dry and wet monolayer for the Berger potential model, can be seen in Figure 4.1.



⁴² H. J. C. Berendsen *et al.* *Comput. Phys. Commun.* 91.1-3 (1995), pp. 43–56; E. Lindahl *et al.* *J. Mol. Model.* 7.8 (2001), pp. 306–317; D. van der Spoel *et al.* *J. Comput. Chem.* 26.16 (2005), pp. 1701–1718; B. Hess *et al.* *J. Chem. Theory Comput.* 4.3 (2008), pp. 435–447.

⁴³ I.-C. Yeh *et al.* *J. Chem. Phys.* 111.7 (1999), pp. 3155–3162.

⁴⁴ Martínez *et al.*, “PACKMOL: A Package for Building Initial Configurations for Molecular Dynamics Simulations”, op. cit.

Figure 4.1: The DSPC monolayer; (a) without water layer and (b) with water layer, visualised using VMD (W. Humphrey *et al.* *J. Mol. Graph.* 14.1 (1996), pp. 33–38).

A general protocol was then used to relax the system at the desired surface coverage, reproducing the effects of a Langmuir trough *in-silico*. This involved subjecting the system to a semi-isotropic barostat, with a compressibility of $4.5 \times 10^{-5} \text{ bar}^{-1}$ of the Slurids and Berger simulations and $3.0 \times 10^{-4} \text{ bar}^{-1}$ for the MARTINI simulations. The pressure in the z -dimension was kept constant at 1 bar, while it was increased in the x - and y -dimensions isotropically. This allowed the surface area of the interface to reduce, as the phospholipid molecules have a preference to stay at the interface, while the total volume of the system stayed relatively constant, as the water molecules move down to relax the pressure in the z -dimension. When the xy -area is reached that is associated with the area per molecule⁴⁵ for each surface pressure, described by the experimental surface pressure-isotherm shown in Figure 4.2

⁴⁵ Abbreviated to APM.

and given in Table 4.2, the coordinates were saved and used as the starting structure for the equilibration simulation. This equilibration simulation involved continuing the use of the semi-isotropic barostat, with the xy -area of the box fixed, allowing the system to relax at a pressure of 1 bar in the z -dimension. Following the application of the pair of semi-isotropic barostats, the thickness of the water layer was typically in the region of 30 Å. The equilibration period was 1 ns, following which the 50 ns NVT ensemble production simulations were run, on which all analyses were conducted.

Figure 4.2: The experimental surface pressure isotherm for DSPC, taken from I. Kubo *et al.* *Thin Solid Films* 393.1-2 (2001), pp. 80–85.

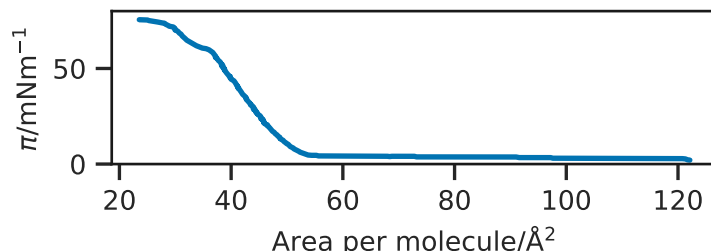


Table 4.2: The areas per molecule (APMs) associated with particular surface pressures and the size of the x - and y -cell dimension for a simulation of 100 phospholipid molecules.

π/mNm^{-1}	APM/ \AA^2	xy -cell length/ \AA
20	47.9	69.1
30	46.4	68.1
40	45.0	67.1
50	44.6	66.0

4.3 DATA ANALYSIS

4.3.1 Traditional layer-model analysis

In order to provide a point of comparison for the simulation-derived methods, the chemically-consistent reflectometry model developed in Chapter 3 was used for the analysis of the experimental data. Two modifications were made to the methodology described in Chapter 3. The first was that the volume of the phospholipid tail group, V_t was constrained based on the APM,⁴⁶

$$V_t = d_t \text{APM}, \quad (4.1)$$

where d_t is the tail layer thickness. The result of this constraint is that both the monolayer model and the simulation-derived models were constrained equally by the measured surface coverage. The second modification was to constrain the head group volume to a value of 339.5 Å, in agreement with the work of Kučerka *et al.*⁴⁷ and Balgavý *et al.*⁴⁸ This constraint was possible on this occasion as the monolayer was at the air-water interface, compared to the air-DES interface previously. A uniform background, limited to lie within

⁴⁶ As taken from the surface pressure-isotherm data

⁴⁷ Kučerka *et al.*, “Determination of Bilayer Thickness and Lipid Surface Area in Unilamellar Dimyristoylphosphatidylcholine Vesicles from Small-Angle Neutron Scattering Curves: A Comparison of Evaluation Methods”, op. cit.

⁴⁸ Balgavý *et al.*, “Evaluation of Small-Angle Neutron Scattering Curves of Unilamellar Phosphatidylcholine Liposomes Using a Mutilshell Model of Bilayer Neutron Scattering Length Density”, op. cit.

10 % of the highest q -vector reflected intensity, and a scale factor were then determined using `refnx` to offer the best agreement between the calculated reflectometry profile and that measured experimentally.

The experimental data from all seven contrasts were co-refined to a single monolayer model at each surface pressure, where the head thickness, tail thickness, and interfacial roughness were allowed to vary. The co-refinement of measurements at different surface pressures was not required, as there was a substantial number of contrasts measured. The values of the head and tail scattering lengths are given in Table 4.3, while the SLD of the super and sub-phase were taken as 0 \AA^{-1} , and 6.35 \AA^{-1} and 0 \AA^{-1} respectively. For each co-refinement of seven neutron reflectometry measurements, there were in total five degrees of freedom in the fitting process, and the fitting was performed using a differential evolution algorithm. As with the work of Chapter 3, Markov chain Monte Carlo sampling was used to obtain experimental uncertainties on the fitted model, enabled by the `emcee` package Foreman-Mackey *et al.*, “Emcee : The MCMC Hammer”, op. cit. The same protocol for this sampling was used herein.

Contrast	d ₁₃ -DSPC	d ₇₀ -DSPC	d ₈₃ -DSPC	h-DSPC
$b_{\text{head}} 10 \times 10^{-4} \text{ \AA}$	19.54	11.21	24.75	6.01
$b_{\text{tail}} 10 \times 10^{-4} \text{ \AA}$	-3.58	69.32	69.32	-3.58

Table 4.3: The different scattering lengths of the head and tail phospholipid components.

4.3.2 Simulation-derived analysis

A custom-class, `md_simulation`, was developed for `refnx`⁴⁹ that enabled the determination of a reflectometry profile from simulation, using a similar method to that employed in previous work, such as Dabkowska *et al.*⁵⁰ The Abelès layer model formalism is applied to layers, the SLD of which is drawn directly from the simulation, and the thickness of which is defined. The layer thickness used was 1 \AA for the Slipid and Berger potential model simulations, with an interfacial roughness between these layers of 0 \AA . For the MARTINI potential model, a layer thickness of 4 \AA was used, with an interfacial roughness of 0.4 \AA .⁵¹ Each of the 50 ns production simulations were analysed each 0.1 ns, and the SLD profiles were determined by summing the scattering lengths, b_j , for each of the atoms in a given layer.

$$\text{SLD}_n = \frac{\sum_j b_j}{V_n}, \quad (4.2)$$

where, V_n is the volume of the layer n , obtained from the simulation cell parameters in the plane of the interface and the defined layer thickness. A uniform background, limited to lie within 10 % of the highest q -value reflected intensity, and a scale factor were then determined using `refnx` to offer the best agreement between

⁴⁹ Nelson *et al.*, “Refnx: Neutron and X-Ray Reflectometry Analysis in Python”, op. cit.; Nelson *et al.*, *Refnx v0.1.2*, op. cit.

⁵⁰ Dabkowska *et al.*, “Modulation of Dipalmitoylphosphatidylcholine Monolayers by Dimethyl Sulfoxide”, op. cit.

⁵¹ The motivation for this is discussed in Section 4.4.2.

the calculated reflectometry profile and that measured experimentally.

4.3.3 Comparison between monolayer model and simulation-derived analysis

In order to assess the agreement between the model from each method, the following goodness-of-fit metric was used, following the transformation of the data into Rq^4 space,

$$\chi^2 = \sum_{i=1}^{N_{\text{data}}} \frac{[R_{\text{exp}}(q_i) - R_{\text{sim}}(q_i)]^2}{[\delta R_{\text{exp}}(q_i)]^2}, \quad (4.3)$$

where, q_i is a given q -vector, $R_{\text{exp}}(q_i)$ is the experimental reflected intensity, $R_{\text{sim}}(q_i)$ is the simulation-derived/traditionally-developed reflected intensity, and $\delta R_{\text{exp}}(q_i)$ is the resolution function of the experimental data.

⁵² Abbreviated to wph.

The number of water molecules per head group⁵² was also compared between the different methods. This was obtained from the monolayer model by considering the solvent fraction in the head-layer, ϕ_h , the volume of the head group, V_h , and taking the volume of a single water molecule to be 29.9 \AA^3 ⁵³,

$$\text{wph} = \frac{\phi_h V_h}{29.9 - 29.9\phi_h}. \quad (4.4)$$

⁵³ Found from the density of water as 997 kg m^{-3} .

⁵⁴ The phospholipid heads, phospholipid tails, and water.

In MD simulations, the number densities, in the z -dimension, for each of the three components⁵⁴ may be obtained directly from the trajectory. In order to determine the number of water molecules per headgroup from the MD simulations, a head-layer region was defined of that which contained the middle 60 % of the phospholipid head number density. The ratio between the water density and the phospholipid head density was then found within the head-layer region.

4.3.4 Simulation trajectory analysis

In order to use the MD trajectory to guide the future development of the chemically-consistent layer model, it was necessary to investigate the solvent penetration into the head group regions of the phospholipids, the roughness of each interface and the phospholipid tail length. The solvent penetration was determined using the intrinsic surfact approach, as detailed by Allen *et al.*⁵⁵ The intrinsic surface approach enables the calculation of the solvent penetration without the effect of the monolayer roughness. This involves taking the z -dimension position of each atom with respect to an anchor point, in this work the anchor point was taken as the phosphorus atom of the phospholipid head that was closest to the atom in the xy -plane. The roughness was probed by investigating the variation in positions from the start, middle and end of each of the head and tail groups. The start of the phospholipid head was defined as the

⁵⁵ D. T. Allen *et al.* *Phys. Chem. Chem. Phys.* 18.44 (2016), pp. 30394–30406; S. A. Pandit *et al.* *J. Chem. Phys.* 119.4 (2003), pp. 2199–2205.

nitrogen atom, the middle the phosphorus and the end the tertiary carbon, which the start of the phospholipid tail was defined as the carbonyl carbon atom, the middle the ninth carbon in the tail, and the end the final carbon in the tail. The distribution of each of these atom types was determined by finding the 95 % quantile for the position in the z-dimension and comparing the spread of the mean and the upper quantile. Finally, the tail length distance, t_t , was found as the distance from the carbonyl carbon atom to the final primary carbon atom of the phospholipid tail. All of these analyses used the MDAnalysis package.⁵⁶

⁵⁶ R. Gowers *et al.* In: Python in Science Conference. Austin, Texas, 2016, pp. 98–105; N. Michaud-Agrawal *et al.* *J. Comput. Chem.* 32.10 (2011), pp. 2319–2327.

4.4 RESULTS & DISCUSSION

Figure 4.3 compared the reflectometry and SLD profiles from each of the different methods at an APM associated with a surface pressure of 30 mN m^{-1} .⁵⁷ In addition, the χ^2 between each of the models and the experimental data for each contrast at an APM associated with a surface pressure of 30 mN m^{-1} , the average χ^2 and standard deviation for each method are given in Table 4.4.⁵⁸

⁵⁷ The data for the other APMs can be found in Appendix ??, however, the trends are similar at all surface pressures.

⁵⁸ The same data for other APMs is available Appendix ??.

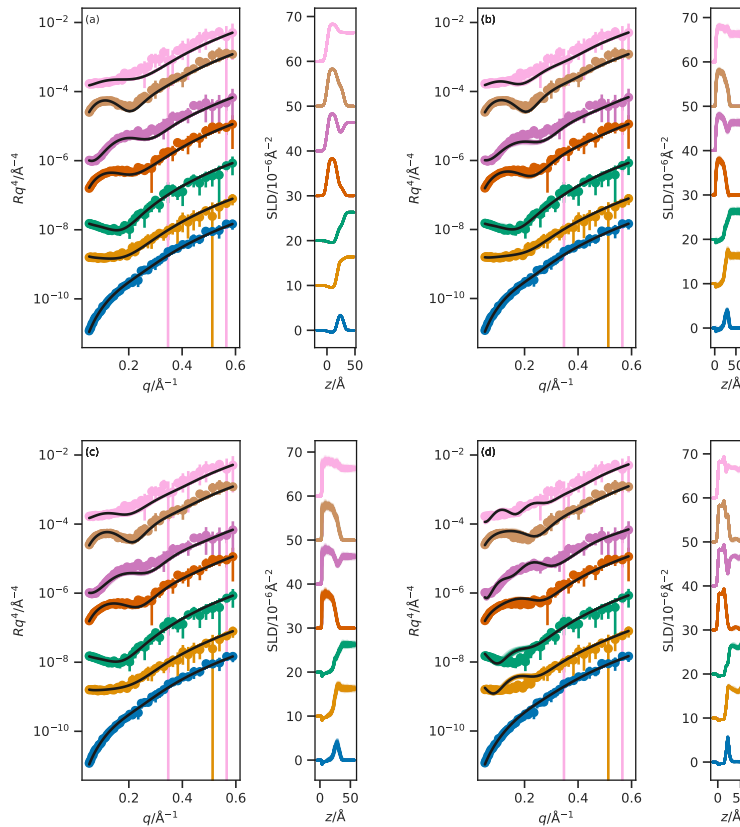


Figure 4.3: The NR profiles (left) and SLD profiles (right) determined at an APM associated with a surface pressure of 30 mN m^{-1} for: (a) the chemically-consistent model, (b) the Slipid all-atom potential model simulations, (c) the Berger united-atom potential model simulations, and (d) the MARTINI coarse-grained potential model simulations. From top-to-bottom the contrasts are as follows; $d_{83}\text{-D}_2\text{O}$, $d_{83}\text{-ACMW}$, $d_{70}\text{-D}_2\text{O}$, $d_{70}\text{-ACMW}$, $h\text{-D}_2\text{O}$, $d_{13}\text{-D}_2\text{O}$, $d_{13}\text{-ACMW}$. The different contrast NR profiles have been offset in the y-axis by an order of magnitude and the SLD profiles offset in the y-axis by $10 \times 10^{-6} \text{\AA}^{-2}$, for clarity.

Contrast	Chemically-consistent	Slipids	Berger	MARTINI
${}^{\text{h}}\text{D}_2\text{O}$	39.42	166.19	119.72	χ^2 values for each of the reflectometry models at an APM surface pressure of 320 mN m^{-1} .
${}^{\text{d}_{13}}\text{D}_2\text{O}$	87.42	235.50	90.35	
${}^{\text{d}_{13}}\text{-ACMW}$	81.93	92.21	85.29	
${}^{\text{d}_{70}}\text{D}_2\text{O}$	131.51	659.32	583.49	
${}^{\text{d}_{70}}\text{-ACMW}$	140.01	83.02	92.85	
${}^{\text{d}_{83}}\text{D}_2\text{O}$	336.02	343.03	424.55	
${}^{\text{d}_{83}}\text{-ACMW}$	104.30	144.51	315.74	
Average	131.52 ± 89.06	246.25 ± 249.21	244.57 ± 238.79	1403.09 ± 1044.80

4.4.1 Traditional analysis

The chemically-consistent model was used to determine the structure of the phospholipid monolayer, Table 4.5 gives the optimum values for the parameters that were varied in the model. It is clear from this Table, that as the surface pressure is increased, as expected, and as found previously,⁵⁹ the overall thickness of the monolayer increases. The thickness increase for the phospholipid tails may be associated with the straightening of the tails with respect to the interface normal, while the thickness increase of the head groups has been noted previously for DSPC.⁶⁰

⁵⁹ Mohwald, "Phospholipid and Phospholipid-Protein Monolayers at the Air-Water Interface", op. cit.; Vaknin *et al.*, "Structural Properties of Phosphatidylcholine in a Monolayer at the Air/Water Interface", op. cit.

⁶⁰ Hollinshead *et al.*, "Effects of Surface Pressure on the Structure of Di-
tearoylphosphatidylcholine Monolayers
Formed at the Air/Water Interface",
it is allowed to vary in the fitting of the
chemically-consistent model, at each
surface pressure measured.

⁶¹ Bayerl *et al.*, "Specular Reflection of Neutrons at Phospholipid Monolayers. Changes of Monolayer Structure and Headgroup Hydration at the Transition from the Expanded to the Condensed Phase State", op. cit.

⁶² J. R. Lu *et al.* *J. Phys. Condens. Matter* 6 (23A 1994), A403–A408.

⁶³ Hollinshead *et al.*, "Effects of Surface Pressure on the Structure of Di-
tearoylphosphatidylcholine Monolayers
Formed at the Air/Water Interface",
op. cit.

⁶⁴ Campbell *et al.*, "Structure of Surfactant and Phospholipid Monolayers at the Air/Water Interface Modeled from Neutron Reflectivity Data", op. cit.

⁶⁵ Small, "Lateral Chain Packing in Lipids and Membranes", op. cit.

Surface Pressure/mN m ⁻¹	$d_h/\text{\AA}$	$d_t/\text{\AA}$	$\sigma_{t,h,s}/\text{\AA}$	$\phi_h \times 10^{-2}$	$V_t/\text{\AA}^3$
20	9.60 ± 0.38	17.89 ± 0.20	$3.31^{+0.03}_{-0.01}$	16.69 ± 4.28	857.17 ± 9.40
30	11.65 ± 0.44	17.99 ± 0.22	$3.31^{+0.04}_{-0.01}$	$30.38^{+3.48}_{-3.64}$	834.86 ± 10.1
40	13.88 ± 0.52	17.85 ± 0.21	$3.31^{+0.03}_{-0.01}$	44.18 ± 2.99	803.38 ± 9.31
50	14.12 ± 0.47	19.01 ± 0.19	$3.31^{+0.06}_{-0.01}$	$45.55^{+2.33}_{-2.45}$	848.00 ± 8.3

It would be anticipated that as the surface pressure increases, there would be a corresponding decrease in the volume fraction of solvent in the head group.⁶¹ However, for DSPC, the volume fraction of the solvent appears to be constant (or even increase slightly) with increasing surface pressure. This is due to the decision to constrain the volume of the phospholipid head, which may decrease with increasing surface pressure. It has been noted previously that the interfacial roughness will increase with increasing surface pressure,⁶² this can be observed with the slight increase between 20-50 mN m⁻¹.

Hollinshead *et al.*⁶³ suggest a tail volume of 972 Å³ from the density data. However, the values found in this work are substantially lower, at ~850 Å³. This reduction, of ~12 %, agrees well with the work of Campbell *et al.*⁶⁴ and Small,⁶⁵ which suggest that under the surface pressure investigated in this work a reduction of the tail volume of up to 15 % may be observed. The model layer structure from the chemically-consistent method provides a satisfactory description of the monolayer structure. However, the use of an MD-driven analysis method may provide greater insight into the chemical nature of the monolayer.

4.4.2 MARTINI

Initially, the MARTINI coarse-grained simulations were analysed with a layer thickness of 1 Å and an interfacial roughness of 0 Å, in a similar fashion to the other potential models. However, as can be seen in Figure 4.4 there is a clear ordering effect present in the MARTINI water, despite the use of the polarised water model. The effect of this ordering on the SLD profile, and therefore the reflectometry profile, can be reduced by using a larger layer thickness and introducing an interfacial roughness. Therefore, in the results discussed below the MARTINI potential model simulation were analysed using a layer thickness of 4 Å and an interfacial roughness of 0.4 Å. It is noted that this structuring may be reduced through the use of a less ordered wall⁶⁶ at the extreme of the simulation cell, however, the aim was to reproduce the experimental conditions using off-the-shelf tools and this would require custom modifications not easily available. Alternatively, it may be possible to effect the presence of this structuring through the inclusion of ~10 % of antifreeze MARTINI beads alongside the normal MARTINI water. However, this method has been noted to also give structuring effects in the presence on an ordered wall.⁶⁷

⁶⁶ Koutsioubas, "Combined Coarse-Grained Molecular Dynamics and Neutron Reflectivity Characterization of Supported Lipid Membranes", op. cit.

⁶⁷ S. J. Marrink *et al.* *Phys. Chem. Chem. Phys.* 12.9 (2010), p. 2254.

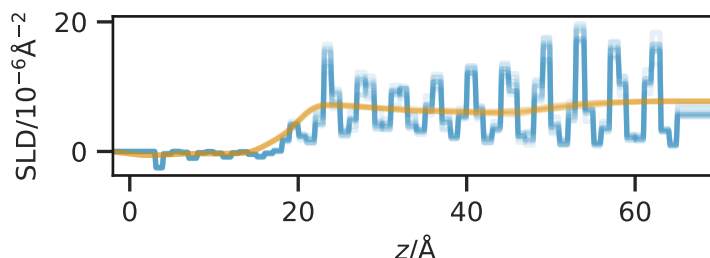


Figure 4.4: A comparison of the scattering length density profile for the MARTINI potential model simulations at an APM associated with a surface pressure of 30 mN m⁻¹; the blue line shows the data where the layer thickness was 1 Å and no interfacial roughness and the orange line shows that with a layer thickness of 4 Å and a roughness of 0.4 Å.

It can be seen from Table 4.4 and Figure 4.3 that even with the larger layer thickness and adding interlayer roughness, the MARTINI potential model simulations do not effectively reproduce the reflectometry profile. Furthermore, it is noted that the agreement with the contrasts containing D₂O is particularly poor. This is most likely an artefact of the structuring effect mentioned above which cannot be completely removed.

However, the agreement for the samples where the contrast uses ACMW, where the water is effectively removed from the SLD profile is also poor. This indicates that there are other artefacts limiting the applicability of the MARTINI potential model. One such artefact is clear from investigating the calculated length of the hydrocarbon tail from the MARTINI simulation, at an APM associated with a surface pressure of 30 mN m⁻¹, which was found to be 16.60^{+1.65}_{-1.88} Å, significantly less than the 24.3 Å estimated by the Tanford equation.⁶⁸ This is due to the nature of the MAR-

⁶⁸ Tanford, *The Hydrophobic Effect: Formation of Micelles and Biological Membranes*, op. cit.

⁶⁹ This corresponds to an all-atom hydrocarbon chain of 16 atoms.

TINI's 4-to-1 beading process, as DSPC has a hydrocarbon tail consisting of 18 carbon atoms, and it is not possible to bead such a chain accurately with the MARTINI potential model. In this work, a MARTINI phospholipid molecule was used with 4 MARTINI beads making up the chain.⁶⁹ Applying the Tanford equation to a hydrocarbon chain of such a length results in an anticipated length of 18.7 Å, which agrees better with that found from the simulation.

In addition to the disagreement from the tail beading process, there is also a clear problem with respect to the solvation of the head layer by polarisable water beads. It can be seen that the number of water molecules per head group in the MARTINI potential model is typically 1.34 ± 0.35 , this is the value at an APM associated with a surface pressure of 30 mN m^{-1} . The chemically-consistent model, however, gives a value of $5.49^{+0.86}_{-0.84}$. It is clear that the 4-to-1 beading present in the MARTINI potential model is creating water molecules that are too large to intercalate into the head layer structure, causing a reduction in the number of waters per head group.

The requirement for a 4-to-1 beading strategy for the MARTINI potential model is a significant weakness. A better method may be limiting experiments to a system that can be modelled exactly or the use of a different beading model. However, we are not aware of an off-the-shelf coarse-grained potential model that would easily offer the exact beading of DSPC.

4.4.3 Comparison with other simulations

Table 4.4 shows that both the Slipid and Berger potential model simulations agree well with the experimental data, with the Slipid potential model offering a slight improvement over the Berger. The quality of agreement between these higher-resolution potential models and the chemically-consistent model is relatively similar. However, the chemically-consistent model still offers a better fit to the experimental data than those determined from MD simulation.

The result that the chemically-consistent model offers better agreement with the data than those from even all-atom simulations is to be expected by considering the level of constraint present implicitly when determining the reflectometry profile directly from the simulation. While the chemically-consistent model constrains the layer model to ensure that the number of phospholipid head groups is the same as the pairs of tail groups, those from MD simulation have more realistic chemical constraints present from the potential model.⁷⁰ The quality of the agreement from this multi-modal approach is sufficient for such a method to be applied regularly to the analysis of neutron reflectometry.

Both the Slipid and Berger potential model simulations produced values for the tail length that were in better agreement with that from the Tanford equation than the MARTINI potential model

⁷⁰ Such as the bonding between atoms, and the non-bonded potentials.

simulations. For the Slipid potential model, with simulations at an APM associated with a surface pressure of 30 mN m^{-1} the tail length was found to be $20.17_{-7.39}^{+1.41}\text{ \AA}$, while for the Berger potential model, at the same APM, a value of $19.80_{-8.17}^{+1.59}\text{ \AA}$ was obtained.

Neither is quite as large as the 24.3 \AA from the Tanford equation.⁷¹

Using the molecular dynamics simulations and the chemically-consistent model, it is possible to compare the number of water molecules per head group. From the Slipid and Berger potential model simulations, the number of water molecules per head group at an APM associated with a surface pressure of 30 mN m^{-1} was found to be $6.41_{-0.76}^{+1.63}$ and $5.49_{-0.53}^{+0.68}$ respectively. These are in good agreement with the value of $5.49_{-0.84}^{+0.86}$ found from the chemically-consistent model, using Equation 4.4.

It should be noted that to obtain the 50 ns production run simulation using the all-atom Slipid potential model required over 13 days of using 32 cores of the SCARF computing resource. This is non-trivial and therefore not necessarily applicable to all neutron reflectometry measurements. However, the use of a 2 fs timestep could reduce this time significantly. Additionally, Figure 4.5 shows the results from the first 5 ns of the Slipid potential model simulations, at an APM associated with a surface pressure of 30 mN m^{-1} , and already good agreement with the data is apparent. It is important to acknowledge that the length of simulation required may be extremely system specific. Furthermore, recent developments of molecular dynamics simulations of graphical processing units (GPUs) may allow for significant speed up of the simulations. The nearly as accurate Berger potential model simulations, only approximately 2 days of the same compute resource was required. This suggests that by using the a larger timestep, shorter simulations, and the power of GPU-based molecular dynamics engines, it may be possible to run these simulations alongside experiments at large facilities to aid interpretation and analysis.

4.4.4 Using the Slipid potential model simulations to improve the monolayer model

Despite the chemically-consistent model offering a small improvement in agreement over the Slipid potential model simulation, we believe that it is possible to use the MD simulations to improve the existing this model. A possible improvement can be found from considering Figure 4.6, which shows the solvent penetration of the phospholipid heads, using the intrinsic surface approach to remove the effect of the interfacial roughness. It is clear that the plot is not step-wise as is obtained from the uniform solvation model that is commonly used in traditional layer models. Nor is the distribution sigmoidal, as there is a small deviation in the region of the ester group of the phospholipid heads. This is either due to the hydrophilic interaction of the carbonyl moiety or from pock-

⁷¹ It should be noted that this value is considered a theoretical maximum for a fully extended carbon chain, which is unlikely to occur, in a liquid phase monolayer, in reality due to entropic considerations.

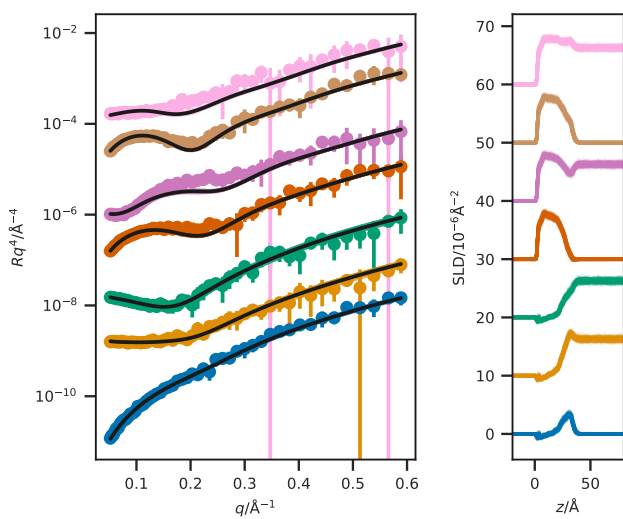


Figure 4.5: The reflectometry and SLD profiles obtained from the first 5 ns of the Slipid potential model simulation, at an APM associated with a surface pressure of 30 mN m^{-1} . From top-to-bottom the contrasts are as follows; $d_{83}-\text{D}_2\text{O}$, $d_{83}-\text{ACMW}$, $d_{70}-\text{D}_2\text{O}$, $d_{70}-\text{ACMW}$, $\text{h}-\text{D}_2\text{O}$, $d_{13}-\text{D}_2\text{O}$, $d_{13}-\text{ACMW}$. The different contrast reflectometry profiles have been offset in the y -axis by an order of magnitude and the SLD profiles offset in the y -axis by $10 \times 10^{-6} \text{ \AA}^{-2}$, for clarity.

ets of water forming at the air-water interface. Regardless of the mechanism, this suggests that a different solvation model should be considered for a realistic description of the solvent penetration.

Figure 4.6: The simulation time-averaged intrinsic density profile of the water molecules (blue dots), and phospholipid components (head groups: green dots, tail groups: red dots), where the phosphorus atoms of the phospholipid heads create the intrinsic surface at $z = 0\text{\AA}$, and the equivalent number density from the chemically-consistent model (orange line).

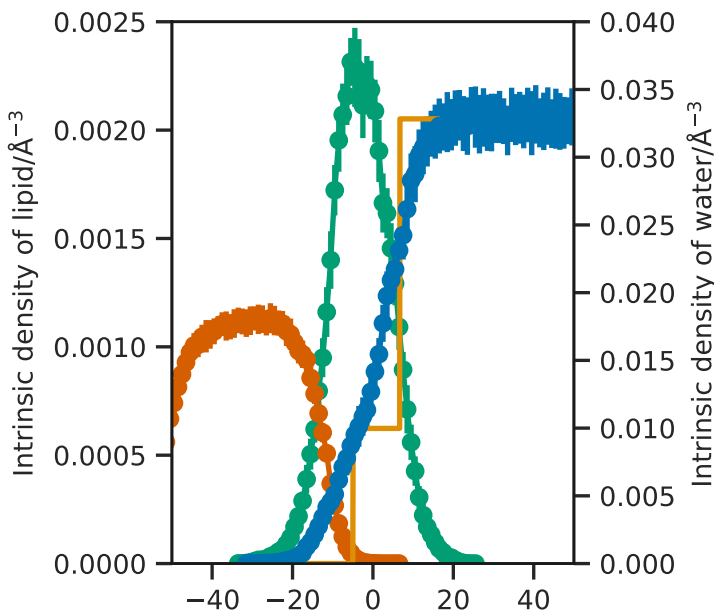


Figure 4.6 also shows that without the presence of the roughness, the distribution of the head groups is relatively normal. This agrees well with the model used previously to fit the experimental data by Hollinshead *et al.*⁷² where Gaussian functions were used to describe the phospholipid head and tail groups. However, the tail group distribution is not Gaussian and this previous method failed to include any additional factors to account for in-

⁷² Hollinshead *et al.*, "Effects of Surface Pressure on the Structure of Disteroylphosphatidylcholine Monolayers Formed at the Air/Water Interface", *op. cit.*

terfacial roughness. Previous work has suggested that when only a single phospholipid type is present, the roughness between the layers should be conformal in nature, that is it should be carried uniformly through the layers.⁷³ However, from the investigation of the SLD profiles in Figure 4.3(b) it appears that the roughness between the phospholipid tails and the air is dramatically different from that at the phospholipid head-water interface. In an effort to quantify the interfacial roughness in the simulations, we have used the method outlined in Section 4.3.4. The values for the mean, 95 % quantile, and the spread between these for the z-dimension position for atoms representative of the start, middle, and end of each of the phospholipid head and tails are given in Table 4.6, for each the APM associated with a surface pressure of 30 mN m^{-1} .⁷⁴ From this table, it is clear that at the very start of the phospholipid molecule⁷⁵ the roughness is very large with a value of $\sim 10 \text{ \AA}$ for the nitrogen atom. However this decreases slightly within the phospholipid head, reaching a value of 8.6 \AA for the end of the head group. There is then a substantial decrease noted in the phospholipid tail, going from $\sim 8.5 \text{ \AA}$ at the start of the tail to $\sim 1.5 \text{ \AA}$ at the end. We believe that this indicates the presence of a highly non-conformal roughness in the phospholipid monolayer of a single phospholipid type and therefore in future, it is important to consider this possibility in the use of model layer structure method.

Position	Mean/ \AA	95 % quantile/ \AA	Spread/ \AA
Start-Head	66.6	76.6	10.1
Mid-Head	67.7	76.6	9.0
End-Head	70.8	79.3	8.6
Start-Tail 1	72.2	80.3	8.1
Start-Tail 2	73.0	81.7	8.6
Mid-Tail 1	80.9	87.1	6.2
Mid-Tail 2	82.3	87.9	5.6
End-Tail 1	91.1	93.3	2.2
End-Tail 2	92.4	93.5	1.1

⁷³ I. V. Kozhevnikov. *Crystallogr. Rep.* 57.4 (2012), pp. 490–498; Campbell *et al.*, “Structure of Surfactant and Phospholipid Monolayers at the Air/Water Interface Modeled from Neutron Reflectivity Data”, op. cit.

⁷⁴ Similar data at other surface pressures can be found in Appendix ??.

⁷⁵ At the head group.

Table 4.6: The mean, 95 % quantile, and their spread for the z-dimension position of atoms representative of difference parts of the phospholipid, at an APM associated with a surface pressure of 30 mN m^{-1} .

4.5 CONCLUSIONS

This chapter presents a direct comparison between a traditional method for the analysis of neutron reflectometry measurements with an analysis method using simulations from a range of all-atom and coarse-grained molecular dynamics potential models. It was shown that the MARTINI potential model could not accurately reproduce the experimental neutron reflectometry data, likely, due to the limitations of the 4-to-1 beading system when applied to a carbon chain of 18 atoms.

The Berger united atom and Slipids all-atom potential models both showed good agreement with the experimental data, however, the best agreement was obtained from the traditional chemically-consistent layer model. This would be expected given

that the chemically-consistent model contains many more “degrees of freedom” than the simulations which are severely chemically-constrained by the potential model.

Finally, some points from the highest resolution, Slipid, simulations were noted that may be used to improve the traditional monolayer model. For example, it is desirable to model non-uniform solvation of the head group region which would enable a more accurate modelling of the lipid monolayer and the use of a conformal roughness may not be the best constraint to apply. Application of these improvements may enable the more accurate modelling of phospholipid monolayers from neutron reflectometry.

A

ADDITIONAL CODE BLOCKS FOR DIFFERENTIAL EVOLUTION

```
import numpy as np

def mutation(p, b, km):
    """
    Performs the mutation step, where the parent population vector
    is transformed to produce a mutant vector.

    Parameters
    -----
    p: float, array_like
        The parent population vector. An array of shape (i, j),
        where i is the number of variables and j is the population
        size.
    b: float, array_like
        The best member of the parent population. An array of
        size i, where i is the number of variables.
    km: float
        The mutation constant.

    Returns
    -----
    float, array_like
        The mutant vector. An array of shape (i, j), where i is
        the number of variables and j is the population size.
    """
    m = np.zeros_like(p)
    R = np.random.randint(p.shape[1], size=(2, p.shape[1]))
    for j in range(p.shape[1]):
        m[:, j] = b + km * (p[:, R[0, j]] - p[:, R[1, j]])
    return m
```

Code Block A.1: The mutation step used in a classical trial method for a differential evolution algorithm, as described in M. Björck. *J. Appl. Crystallogr.* 44.6 (2011), pp. 1198–1204.

```
import numpy as np

def recombination(p, m, kr):
    """
    The recombination step, where the mutant and parent population
    vectors are combined.

    Parameters
    -----
    p: float, array_like
        The parent population vector. An array of shape (i, j),
        where i is the number of variables and j is the population
        size.
    m: float, array_like
        The mutant vector. An array of shape (i, j), where i
        is the number of variables and j is the population size.
    kr: float
        The recombination constant.

    Returns
    -----
    float, array_like
        The offspring population vector. An array of shape (i, j),
        where i is the number of variables and j is the population
        size.
    """
    o = np.array(p)
    rand = np.random.rand(p.shape[0], p.shape[1])
    o[rand < kr] = m[rand < kr]
    return o
```

Code Block A.2: The recombination step used in a classical trial method for a differential evolution algorithm, as described in M. Björck. *J. Appl. Crystallogr.* 44.6 (2011), pp. 1198–1204.

```

import numpy as np

def selection(p, o, f):
    """
    The selection function, where the population member that
    return the minimum value for the figure of merit is brought
    forward to the next generation.

    Parameters
    -----
    p: float, array_like
        The parent population vector. An array of shape (i, j),
        where i is the number of variables and j is the population
        size.
    o: float, array_like
        The offspring population vector. An array of shape (i, j),
        where i is the number of variables and j is the population
        size.
    f: function
        The figure of merit function to be minimised.

    Returns
    -----
    float, array_like
        The new parent population vector. An array of shape (i, j),
        where i is the number of variables and j is the population
        size.
    """
    new_p = np.array(p)
    for j in range(p.shape[1]):
        p_fom = f(p[:, j])
        o_fom = f(o[:, j])
        if o_fom < p_fom:
            new_p[:, j] = o[:, j]
    return new_p

```

Code Block A.3: The selection step used in a differential evolution algorithm, as described in M. Björck. *J. Appl. Crystallogr.* 44.6 (2011), pp. 1198–1204.

REFERENCES

- Abelès, F. "Sur La Propagation Des Ondes Électromagnétiques Dans Les Milieux Sratifiés". *Ann. Phys.* 12.3 (1948), pp. 504–520. doi: 10.1051/anphys/194812030504.
- Ackley, D. H. "A Connectionist Machine for Genetic Hillclimbing". PhD. Michigan, US: University of Michigan, 1987. 260 pp.
- Albrecht, O., H. Gruler, and E. Sackmann. "Polymorphism of Phospholipid Monolayers". *J. Phys. France* 39.3 (1978), pp. 301–313. doi: 10.1051/jphys:01978003903030100.
- Allen, D. T., Y. Saaka, L. C. Pardo, M. J. Lawrence, and C. D. Lorenz. "Specific Effects of Monovalent Counterions on the Structural and Interfacial Properties of Dodecyl Sulfate Monolayers". *Phys. Chem. Chem. Phys.* 18.44 (2016), pp. 30394–30406. doi: 10.1039/C6CP05714D.
- Andersen, H. C. "Molecular Dynamics Simulations at Constant Pressure and/or Temperature". *J. Chem. Phys.* 72.4 (1980), pp. 2384–2393. doi: 10.1063/1.439486.
- Anderson, P. M. and M. R. Wilson. "Molecular Dynamics Simulations of Amphiphilic Graft Copolymer Molecules at a Water/Air Interface". *J. Chem. Phys.* 121.17 (2004), p. 8503. doi: 10.1063/1.1796251.
- Anton, N., H. Mojzisova, E. Porcher, J.-P. Benoit, and P. Saulnier. "Reverse Micelle-Loaded Lipid Nano-Emulsions: New Technology for Nano-Encapsulation of Hydrophilic Materials". *Int. J. Pharm.* 398.1-2 (2010), pp. 204–209. doi: 10.1016/j.ijpharm.2010.07.039.
- Araujo, C. F., J. A. P. Coutinho, M. M. Nolasco, S. F. Parker, P. J. A. Ribeiro-Claro, S. Rudić, B. I. G. Soares, and P. D. Vaz. "Inelastic Neutron Scattering Study of Reline: Shedding Light on the Hydrogen Bonding Network of Deep Eutectic Solvents". *Phys. Chem. Chem. Phys.* 19.27 (2017), pp. 17998–18009. doi: 10.1039/C7CP01286A.
- Armen, R. S., O. D. Uitto, and S. E. Feller. "Phospholipid Component Volumes: Determination and Application to Bilayer Structure Calculations". *Biophys. J.* 75.2 (1998), pp. 734–744. doi: 10.1016/S0006-3495(98)77563-0.
- Arnold, T., A. J. Jackson, A. Sanchez-Fernandez, D. Magnone, A. E. Terry, and K. J. Edler. "Surfactant Behavior of Sodium Dodecylsulfate in Deep Eutectic Solvent Choline Chloride/Urea".

- Langmuir* 31.47 (2015), pp. 12894–12902. doi: 10.1021/acs.langmuir.5b02596.
- Arnold, T., C. Nicklin, J. Rawle, J. Sutter, Trevor Bates, B. Nutter, G. McIntyre, and M. Burt. “Implementation of a Beam Deflection System for Studies of Liquid Interfaces on Beamline I07 at Diamond”. *J. Synchrotron Radiat.* 19.3 (2012), pp. 408–416. doi: 10.1107/S0909049512009272.
- Balgavý, P., N Kučerka, V. I. Gordeliy, and V. G. Cherezov. “Evaluation of Small-Angle Neutron Scattering Curves of Unilamellar Phosphatidylcholine Liposomes Using a Mutishell Model of Bilayer Neutron Scattering Length Density”. *Acta Phys. Slovaca* 51.1 (2001), pp. 53–68.
- Banjare, M. K., K. Behera, M. L. Satnami, S. Pandey, and K. K. Ghosh. “Self-Assembly of a Short-Chain Ionic Liquid within Deep Eutectic Solvents”. *RSC Adv.* 8.15 (2018), pp. 7969–7979. doi: 10.1039/C7RA13557B.
- Banks, J. L., H. S. Beard, Y. Cao, A. E. Cho, Wolfgang Damm, R. Farid, A. K. Felts, T. A. Halgren, D. T. Mainz, J. R. Maple, R. Murphy, D. M. Philipp, M. P. Repasky, L. Y. Zhang, B. J. Berne, R. A. Friesner, E. Gallicchio, and R. M. Levy. “Integrated Modeling Program, Applied Chemical Theory (IMPACT)”. *J. Comput. Chem.* 26.16 (2005), pp. 1752–1780. doi: 10.1002/jcc.20292.
- Barker, R. D., L. E. McKinley, and S. Titmuss. “Neutron Reflectivity as a Tool for Physics-Based Studies of Model Bacterial Membranes”. In: *Biophysics of Infection*. Ed. by M. C. Leake. New York: Springer, 2016, pp. 261–282. ISBN: 978-3-319-32189-9.
- Bayerl, T. M., R. K. Thomas, J. Penfold, A. Rennie, and E. Sackmann. “Specular Reflection of Neutrons at Phospholipid Monolayers. Changes of Monolayer Structure and Headgroup Hydration at the Transition from the Expanded to the Condensed Phase State”. *Biophys. J.* 57.5 (1990), pp. 1095–1098. doi: 10.1016/S0006-3495(90)82628-X.
- Bello, G., A. Bodin, M. J. Lawrence, D. Barlow, A. J. Mason, R. D. Barker, and R. D. Harvey. “The Influence of Rough Lipopolysaccharide Structure on Molecular Interactions with Mammalian Antimicrobial Peptides”. *BBA - Biomembranes* 1858.2 (2016), pp. 197–209. doi: 10.1016/j.bbamem.2015.11.007.
- Berendsen, H. J. C., J. R. Grigera, and T. P. Straatsma. “The Missing Term in Effective Pair Potentials”. *J. Phys. Chem.* 91.24 (1987), pp. 6269–6271. doi: 10.1021/j100308a038.
- Berendsen, H. J. C., J. P. M. Postma, W. F. van Gunsteren, A. Di-Nola, and J. R. Haak. “Molecular Dynamics with Coupling to an External Bath”. *J. Chem. Phys.* 81.8 (1984), pp. 3684–3690. doi: 10.1063/1.448118.
- Berendsen, H. J. C., D. van der Spoel, and R. van Drunen. “GROMACS: A Message-Passing Parallel Molecular Dynamics Implementation”. *Comput. Phys. Commun.* 91.1-3 (1995), pp. 43–56. doi: 10.1016/0010-4655(95)00042-E.

- Berger, O., O. Edholm, and F. Jähnig. "Molecular Dynamics Simulations of a Fluid Bilayer of Dipalmitoylphosphatidylcholine at Full Hydration, Constant Pressure, and Constant Temperature". *Biophys. J.* 72.5 (1997), pp. 2002–2013. doi: 10.1016/S0006-3495(97)78845-3.
- Björck, M. "Fitting with Differential Evolution: An Introduction and Evaluation". *J. Appl. Crystallogr.* 44.6 (2011), pp. 1198–1204. doi: 10.1107/S0021889811041446.
- Björck, M. and G. Andersson. "GenX: An Extensible X-Ray Reflectivity Refinement Program Utilizing Differential Evolution". *J. Appl. Crystallogr.* 40.6 (2007), pp. 1174–1178. doi: 10.1107/S0021889807045086.
- Bobone, S., Y. Gerelli, M. De Zotti, G. Bocchinfuso, A. Farrotti, B. Orioni, F. Sebastiani, E. Latter, J. Penfold, R. Senesi, F. Formaggio, A. Palleschi, C. Toniolo, G. Fragneto, and L. Stella. "Membrane Thickness and the Mechanism of Action of the Short Peptibol Trichogin GA IV". *(BBA) - Biomembranes* 1828.3 (2013), pp. 1013–1024. doi: 10.1016/j.bbamem.2012.11.033.
- Bowerman, S., A. S. J. B. Rana, A. Rice, G. H. Pham, E. R. Strieter, and J. Wereszczynski. "Determining Atomistic SAXS Models of Tri-Ubiquitin Chains from Bayesian Analysis of Accelerated Molecular Dynamics Simulations". *J. Chem. Theory Comput.* 13.6 (2017), pp. 2418–2429. doi: 10.1021/acs.jctc.7b00059.
- Braun, L., M. Uhlig, R. von Klitzing, and R. A. Campbell. "Polymers and Surfactants at Fluid Interfaces Studied with Specular Neutron Reflectometry". *Adv. Colloid Interface Sci.* 247 (2017), pp. 130–148. doi: 10.1016/j.cis.2017.07.005.
- Brini, E., E. A. Algaer, P. Ganguly, C. Li, F. Rodríguez-Ropero, and N. F. A. van der Vegt. "Systematic Coarse-Graining Methods for Soft Matter Simulations – a Review". *Soft Matter* 9.7 (2013), pp. 2108–2119. doi: 10.1039/C2SM27201F.
- Bryant, S. J., R. Atkin, and G. G. Warr. "Spontaneous Vesicle Formation in a Deep Eutectic Solvent". *Soft Matter* 12.6 (2016), pp. 1645–1648. doi: 10.1039/C5SM02660A.
- Bryant, S. J., R. Atkin, and G. G. Warr. "Effect of Deep Eutectic Solvent Nanostructure on Phospholipid Bilayer Phases". *Langmuir* 33.27 (2017), pp. 6878–6884. doi: 10.1021/acs.langmuir.7b01561.
- Buckingham, R. A. "The Classical Equation of State of Gaseous Helium, Neon and Argon". *Proc. Royal Soc. Lond. A.* 168.933 (1938), pp. 264–283. doi: 10.1098/rspa.1938.0173.
- Bucknall, D. G., S. A. Butler, H. E. Hermes, and J. S. Higgins. "Neutron Reflectivity Investigations of Semi-Crystalline Polymer Interfaces". *Physica B* 241-243 (1997), pp. 1071–1073. doi: 10.1016/S0921-4526(97)00793-X.
- Bussi, G., D. Donadio, and M. Parrinello. "Canonical Sampling through Velocity Rescaling". *J. Chem. Phys.* 126.1 (2007), p. 014101. doi: 10.1063/1.2408420.

- Campbell, R. A., Y. Saaka, Y. Shao, Y. Gerelli, R. Cubitt, E. Nazaruk, D. Matyszewska, and M. J. Lawrence. "Structure of Surfactant and Phospholipid Monolayers at the Air/Water Interface Modeled from Neutron Reflectivity Data". *J. Colloid Interface Sci.* 531 (2018), pp. 98–108. doi: 10.1016/j.jcis.2018.07.022.
- Campbell, R. A., H. P. Wacklin, I. Sutton, R. Cubitt, and G. Fragneto. "FIGARO: The New Horizontal Neutron Reflectometer at the ILL". *Eur. Phys. J. Plus* 126.11 (2011), p. 107. doi: 10.1140/epjp/i2011-11107-8.
- Carbone, P., H. A. K. Varzaneh, X. Chen, and F. Müller-Plathe. "Transferability of Coarse-Grained Force Fields: The Polymer Case". *J. Chem. Phys.* 128.6 (2008), p. 064904. doi: 10.1063/1.2829409.
- Clifton, L. A., M. Sanders, C. Kinane, T. Arnold, K. J. Edler, C. Neylon, R. J. Green, and R. F. Frazier. "The Role of Protein Hydrophobicity in Thionin–Phospholipid Interactions: A Comparison of A1 and A2-Purothionin Adsorbed Anionic Phospholipid Monolayers". *Phys. Chem. Chem. Phys.* 14.39 (2012), p. 13569. doi: 10.1039/c2cp42029e.
- Cordobés, F., J. Muñoz, and C. Gallegos. "Linear Viscoelasticity of the Direct Hexagonal Liquid Crystalline Phase for a Heptane/Nonionic Surfactant/Water System". *J. Colloid Interface Sci.* 187.2 (1997), pp. 401–417. doi: 10.1006/jcis.1996.4707.
- Cordomí, A., G. Caltabiano, and L. Pardo. "Membrane Protein Simulations Using AMBER Force Field and Berger Lipid Parameters". *J. Chem. Theory Comput.* 8.3 (2012), pp. 948–958. doi: 10.1021/ct200491c.
- Coulomb, C. A. "Premier Mémoire Sur l'électricité et Le Magnétisme". *Histoire de l'Académie Royale des Sciences. Imprimerie Royale* (1788), pp. 569–577.
- Coulomb, C. A. "Second Mémoire Sur l'électricité et Le Magnétisme". *Histoire de l'Académie Royale des Sciences. Imprimerie Royale* (1788), pp. 578–611.
- Dabkowska, A. P., L. E. Collins, D. J. Barlow, R. Barker, S. E. McLain, M. J. Lawrence, and C. D. Lorenz. "Modulation of Dipalmitoylphosphatidylcholine Monolayers by Dimethyl Sulfoxide". *Langmuir* 30.29 (2014), pp. 8803–8811. doi: 10.1021/la501275h.
- Dai, Y., J. van Spronsen, G.-J. Witkamp, R. Verpoorte, and Y. H. Choi. "Natural Deep Eutectic Solvents as New Potential Media for Green Technology". *Anal. Chim. Acta* 766 (2013), pp. 61–68. doi: 10.1016/j.aca.2012.12.019.
- Daillant, J., L. Bosio, and J. J. Benattar. "X-Ray Reflectivity Study of the Liquid-Expanded Liquid-Condensed Phase Transition". *EPL* 12.8 (1990), pp. 715–720. doi: 10.1209/0295-5075/12/8/008.
- Dane, A. D., A. Veldhuis, D. K. G. de Boer, A. J. G. Leenaers, and L. M. C. Buydens. "Application of Genetic Algorithms for Char-

- acterization of Thin Layered Materials by Glancing Incidence X-Ray Reflectometry". *Physica B* 253.3-4 (1998), pp. 254–268. doi: 10.1016/S0921-4526(98)00398-6.
- Darré, L., J. Iglesias-Fernandez, A. Kohlmeyer, H. Wacklin, and C. Domene. "Molecular Dynamics Simulations and Neutron Reflectivity as an Effective Approach To Characterize Biological Membranes and Related Macromolecular Assemblies". *J. Chem. Theory Comput.* 11.10 (2015), pp. 4875–4884. doi: 10.1021/acs.jctc.5b00635.
- De Broglie, L. "Recherches Sur La Théorie Des Quanta". *Ann. Phys. (Paris)* 10.3 (1925), pp. 22–125.
- De Haan, V.-O. and G. G. Drijkoningen. "Genetic Algorithms Used in Model Finding and Fitting for Neutron Reflection Experiments". *Physica B* 198.1-3 (1994), pp. 24–26. doi: 10.1016/0921-4526(94)90118-X.
- Edler, K. J. and D. T. Bowron. "Combining Wide-Angle and Small-Angle Scattering to Study Colloids and Self-Assembly". *Curr. Opin. Colloid Interface Sci.* 20.4 (2015), pp. 227–234. doi: 10.1016/j.cocis.2015.07.002.
- Essmann, U., L. Perera, M. L. Berkowitz, T. Darden, H. Lee, and L. G. Pedersen. "A Smooth Particle Mesh Ewald Method". *J. Chem. Phys.* 103.19 (1995), pp. 8577–8593. doi: 10.1063/1.470117.
- Ewald, P. P. "Die Berechnung Optischer Und Elektrostatischer Gitterpotentiale". *Ann. Phys.* 369.3 (1921), pp. 253–287. doi: 10.1002/andp.19213690304.
- Farago, B. "Recent Developments and Applications of NSE in Soft Matter". *Curr. Opin. Colloid Interface Sci.* 14.6 (2009), pp. 391–395. doi: 10.1016/j.cocis.2009.07.004.
- Foglia, F., G. Fragneto, L. A. Clifton, M. J. Lawrence, and D. J. Barlow. "Interaction of Amphotericin B with Lipid Monolayers". *Langmuir* 30.30 (2014), pp. 9147–9156. doi: 10.1021/la501835p.
- Foglia, F., M. J. Lawrence, and D. J. Barlow. "Studies of Model Biological and Bio-Mimetic Membrane Structure: Reflectivity vs Diffraction, a Critical Comparison". *Curr. Opin. Colloid Interface Sci.* 20.4 (2015), pp. 235–243. doi: 10.1016/j.cocis.2015.08.001.
- Foreman-Mackey, D., D. W. Hogg, D. Lang, and J. Goodman. "Emcee : The MCMC Hammer". *Publ. Astron. Soc. PAc.* 125.925 (2013), pp. 306–312. doi: 10.1086/670067.
- Frenkel, D. and B. Smit. *Understanding Molecular Simulation: From Algorithms to Applications*. San Diego, USA: Academic Press, 1996. ISBN: 978-0-12-267351-1.
- Garcia Sakai, V. and A. Arbe. "Quasielastic Neutron Scattering in Soft Matter". *Curr. Opin. Colloid Interface Sci.* 14.6 (2009), pp. 381–390. doi: 10.1016/j.cocis.2009.04.002.

- Garcia-Gutierrez, M. C. and D. R. Rueda. "Bases of Synchrotron Radiation, Light Sources, and Features of X-Ray Scattering Beamlines". In: *Applications of Synchrotron Light to Scattering and Diffraction in Materials and Life Sciences*. Ed. by M. Gomez, A. Nogales, M. C. Garcia-Gutierrez, and T. A. Ezquerra. Berlin, DE: Springer-Verlag Berlin Heidelberg, 2009, pp. 1–22. ISBN: 978-3-540-95968-7.
- Geoghegan, M., R. A. L. Jones, D. S. Sivia, J. Penfold, and A. S. Clough. "Experimental Study of Surface Segregation and Wetting in Films of a Partially Miscible Polymer Blend". *Phys. Rev. E* 53.1 (1996), pp. 825–837. doi: 10.1103/PhysRevE.53.825.
- Gerelli, Y. "Aurore: New Software for Neutron Reflectivity Data Analysis". *J. Appl. Crystallogr.* 49.1 (2016), pp. 330–339. doi: 10.1107/S1600576716000108.
- Gerelli, Y. "Aurore: New Software for Neutron Reflectivity Data Analysis. Corrigendum". *J. Appl. Crystallogr.* 49.2 (2016), pp. 712–712. doi: 10.1107/S1600576716002466.
- Gil, D. L. and D. Windover. "Limitations of X-Ray Reflectometry in the Presence of Surface Contamination". *J. Phys. D* 45.23 (2012), p. 235301. doi: 10.1088/0022-3727/45/23/235301.
- Gilks, W., S. Richardson, and D. Spiegelhalter. *Markov Chain Monte Carlo in Practice*. Chapman & Hall/CRC Interdisciplinary Statistics. Boca Raton, US: CRC Press, 1995. ISBN: 978-0-412-05551-5.
- Goodman, J. and J. Weare. "Ensemble Samplers with Affine Invariance". *Comm. App. Math. Comp. Sci.* 5 (2010), pp. 65–80. doi: 10.2140/camcos.2010.5.65.
- Goodwin, J. *Colloids and Interfaces with Surfactants and Polymers*. 2nd ed. Chichester, UK: John Wiley & Sons, 2009. ISBN: 978-0-470-51880-9.
- Gowers, R., M. Linke, J. Barnoud, T. Reddy, M. Melo, S. Seyler, J. Domański, D. Dotson, S. Buchoux, I. Kenney, and O. Beckstein. "MDAnalysis: A Python Package for the Rapid Analysis of Molecular Dynamics Simulations". In: Python in Science Conference. Austin, Texas, 2016, pp. 98–105. doi: 10.25080/Majora-629e541a-00e.
- Graner, F., S. Perez-Oyarzun, A. Saint-Jalmes, C. Flament, and F. Gallet. "Phospholipidic Monolayers on Formamide". *J. Phys. II France* 5.2 (1995), pp. 313–322. doi: 10.1051/jp2:1995131.
- Grigoriev, D., R. Krustev, R. Miller, and U. Pison. "Effect of Monovalent Ions on the Monolayers Phase Behavior of the Charged Lipid DPPG". *J. Phys. Chem. B* 103.6 (1999), pp. 1013–1018. doi: 10.1021/jp983704s.
- Grillo, I. "Small-Angle Neutron Scattering and Applications in Soft Condensed Matter". In: *Soft-Matter Characterization*. Ed. by R. Borsali and R. Pecora. New York, USA: Springer, 2008, pp. 723–782. ISBN: 978-1-4020-4465-6.
- Gumbart, J., L. G. Trabuco, E. Schreiner, E. Villa, and K. Schulten. "Regulation of the Protein-Conducting Channel by a Bound

- Ribosome". *Structure* 17.11 (2009), pp. 1453–1464. doi: 10.1016/j.str.2009.09.010.
- Gutiérrez, M. G., M. L. Ferrer, C. R. Mateo, and F. del Monte. "Freeze-Drying of Aqueous Solutions of Deep Eutectic Solvents: A Suitable Approach to Deep Eutectic Suspensions of Self-Assembled Structures". *Langmuir* 25.10 (2009), pp. 5509–5515. doi: 10.1021/la900552b.
- Hammond, O. S., D. T. Bowron, and K. J. Edler. "Liquid Structure of the Choline Chloride-Urea Deep Eutectic Solvent (Re-line) from Neutron Diffraction and Atomistic Modelling". *Green Chem.* 18.9 (2016), pp. 2736–2744. doi: 10.1039/C5GC02914G.
- Hammond, O. S., D. T. Bowron, A. J. Jackson, T. Arnold, A. Sanchez-Fernandez, N. Tsapatsaris, V. Garcia Sakai, and K. J. Edler. "Resilience of Malic Acid Natural Deep Eutectic Solvent Nanostructure to Solidification and Hydration". *J. Phys. Chem. B* 121.31 (2017), pp. 7473–7483. doi: 10.1021/acs.jpcb.7b05454.
- Hargreaves, R., D. T. Bowron, and K. Edler. "Atomistic Structure of a Micelle in Solution Determined by Wide Q -Range Neutron Diffraction". *J. Am. Chem. Soc.* 133.41 (2011), pp. 16524–16536. doi: 10.1021/ja205804k.
- Harvey, J. *Computational Chemistry*. Oxford: Oxford University Press, 2018. ISBN: 978-0-19-875550-0.
- Hassan, P. A., G. Fritz, and E. W. Kaler. "Small Angle Neutron Scattering Study of Sodium Dodecyl Sulfate Micellar Growth Driven by Addition of a Hydroscopic Salt". *J. Colloid Interface Sci.* 257.1 (2003), pp. 154–162. doi: 10.1016/S0021-9797(02)00020-6.
- Hastings, W. K. "Monte Carlo Sampling Methods Using Markov Chains and Their Applications". *Biometrika* 57.1 (1970), pp. 97–109. doi: 10.1093/biomet/57.1.97.
- Hayward, D. W., J. B. Gilroy, P. A. Rupar, L. Chabanne, C. Pizzey, M. A. Winnik, G. R. Whittell, I. Manners, and R. M. Richardson. "Liquid Crystalline Phase Behavior of Well-Defined Cylindrical Block Copolymer Micelles Using Synchrotron Small-Angle X-Ray Scattering". *Macromolecules* 48.5 (2015), pp. 1579–1591. doi: 10.1021/ma502222f.
- Hazell, G., A. P. Gee, T. Arnold, K. J. Edler, and S. E. Lewis. "Langmuir Monolayers Composed of Single and Double Tail Sulfobetaine Lipids". *J. Colloid Interface Sci.* 474 (2016), pp. 190–198. doi: 10.1016/j.jcis.2016.04.020.
- Heinrich, F., H. Nanda, H. Z. Goh, C. Bachert, M. Lösche, and A. D. Linstedt. "Myristoylation Restricts Orientation of the GRASP Domain on Membranes and Promotes Membrane Tethering". *J. Biol. Chem.* 289.14 (2014), pp. 9683–9691. doi: 10.1074/jbc.M113.543561.
- Helm, C. A., H. Möhwald, K. Kjær, and J. Als-Nielsen. "Phospholipid Monolayer Density Distribution Perpendicular to the

- Water Surface. A Synchrotron X-Ray Reflectivity Study". *EPL* 4.6 (1987), pp. 697–703. doi: 10.1209/0295-5075/4/6/010.
- Hess, B. "P-LINCS: A Parallel Linear Constraint Solver for Molecular Simulation". *J. Chem. Theory Comput.* 4.1 (2008), pp. 116–122. doi: 10.1021/ct700200b.
- Hess, B., C. Kutzner, D. van der Spoel, and E. Lindahl. "GROMACS 4: Algorithms for Highly Efficient, Load-Balanced, and Scalable Molecular Simulation". *J. Chem. Theory Comput.* 4.3 (2008), pp. 435–447. doi: 10.1021/ct700301q.
- Holland, J. H. *Adaptation in Natural and Artificial Systems*. 2nd ed. Boston, USA: MIT Press, 1992. ISBN: 978-0-262-58111-0.
- Hollinshead, C. M., R. D. Harvey, D. J. Barlow, J. R. P. Webster, A. V. Hughes, A. Weston, and M. J. Lawrence. "Effects of Surface Pressure on the Structure of Distearoylphosphatidylcholine Monolayers Formed at the Air/Water Interface". *Langmuir* 25.7 (2009), pp. 4070–4077. doi: 10.1021/la8028319.
- Hoogerheide, D. P., S. Y. Noskov, A. J. Kuszak, S. K. Buchanan, T. K. Rostovtseva, and H. Nanda. "Structure of Voltage-Dependent Anion Channel-Tethered Bilayer Lipid Membranes Determined Using Neutron Reflectivity". *Acta Crystallogr. D* 74.12 (2018), pp. 1219–1232. doi: 10.1107/S2059798318011749.
- Hoover, W. G. "Canonical Dynamics: Equilibrium Phase-Space Distributions". *Phys. Rev. A* 31.3 (1985), pp. 1695–1697. doi: 10.1103/PhysRevA.31.1695.
- Hsieh, Y.-T. and Y.-R. Liu. "Micelle Structure in a Deep Eutectic Solvent for the Electrochemical Preparation of Nanomaterials". *Langmuir* 34.35 (2018), pp. 10270–10275. doi: 10.1021/acs.langmuir.8b01896.
- Hub, J. S. "Interpreting Solution X-Ray Scattering Data Using Molecular Simulations". *Curr. Opin. Struct. Biol.* 49 (2018), pp. 18–26. doi: 10.1016/j.sbi.2017.11.002.
- Hughes, A. V. *RasCAL*. URL: <https://sourceforge.net/projects/rscl/> (Accessed 2016-8-8).
- Hughes, A. V., F. Ciesielski, A. C. Kalli, L. A. Clifton, T. R. Charlton, M. S. P. Sansom, and J. R. P. Webster. "On the Interpretation of Reflectivity Data from Lipid Bilayers in Terms of Molecular-Dynamics Models". *Acta Crystallogr. D* 72.12 (2016), pp. 1227–1240. doi: 10.1107/S2059798316016235.
- Humphrey, W., A. Dalke, and K. Schulten. "VMD: Visual Molecular Dynamics". *J. Mol. Graph.* 14.1 (1996), pp. 33–38. doi: 10.1016/0263-7855(96)00018-5.
- ILL: Neutron for Science: Technical Characteristics*. URL: <https://www.ill.eu/reactor-environment-safety/high-flux-reactor/technical-characteristics/> (Accessed 2016-8-8).
- ISIS – How ISIS Works*. URL: <https://www.isis.stfc.ac.uk/Pages/What-does-ISIS-Neutron-Muon-Source-do.aspx> (Accessed 2018-9-25).

- ISIS – SANS2D.* URL: <https://www.isis.stfc.ac.uk/Pages/Sans2d.aspx> (Accessed 2018-9-25).
- Israelachvili, J. *Intermolecular and Surface Forces*. 3rd ed. Cambridge, USA: Academic Press, 2011. ISBN: 978-0-12-391933-5.
- Ivanović, M. T., L. K. Bruetzel, J. Lipfert, and J. S. Hub. “Temperature-Dependent Atomic Models of Detergent Micelles Refined against Small-Angle X-Ray Scattering Data”. *Angew. Chemie Int. Ed.* 57.20 (2018), pp. 5635–5639. doi: 10.1002/anie.201713303.
- Jämbbeck, J. P. M. and A. P. Lyubartsev. “An Extension and Further Validation of an All-Atomistic Force Field for Biological Membranes”. *J. Chem. Theory Comput.* 8.8 (2012), pp. 2938–2948. doi: 10.1021/ct300342n.
- Jämbbeck, J. P. M. and A. P. Lyubartsev. “Derivation and Systematic Validation of a Refined All-Atom Force Field for Phosphatidylcholine Lipids”. *J. Phys. Chem. B* 116.10 (2012), pp. 3164–3179. doi: 10.1021/jp212503e.
- Jämbbeck, J. P. M. and A. P. Lyubartsev. “Another Piece of the Membrane Puzzle: Extending Lipids Further”. *J. Chem. Theory Comput.* 9.1 (2013), pp. 774–784. doi: 10.1021/ct300777p.
- Jensen, G. V., R. Lund, J. Gummel, T. Narayanan, and J. S. Pedersen. “Monitoring the Transition from Spherical to Polymer-like Surfactant Micelles Using Small-Angle X-Ray Scattering”. *Angew. Chemie Int. Ed.* 53.43 (2014), pp. 11524–11528. doi: 10.1002/anie.201406489.
- Jmol: An Open-Source Java Viewer for Chemical Structures in 3D.* URL: <http://www.jmol.org/> (Accessed 2018-1-28).
- Johnson, S. J., T. M. Bayerl, D. C. McDermott, G. W. Adam, A. R. Rennie, R. K. Thomas, and E. Sackmann. “Structure of an Adsorbed Dimyristoylphosphatidylcholine Bilayer Measured with Specular Reflection of Neutrons”. *Biophys. J.* 59.2 (1991), pp. 289–294. doi: 10.1016/S0006-3495(91)82222-6.
- Jones, E., T. Oliphant, P. Peterson, et al. *SciPy: Open Source Scientific Tools for Python*. URL: <http://www.scipy.org> (Accessed 2019-3-4).
- Jones, R. A. L. *Soft Condensed Matter*. Oxford, UK: Oxford University Press, 2002. ISBN: 978-0-19-850589-1.
- Jorgensen, W. L. and J. Tirado-Rives. “The OPLS [Optimized Potentials for Liquid Simulations] Potential Functions for Proteins, Energy Minimizations for Crystals of Cyclic Peptides and Crambin”. *J. Am. Chem. Soc.* 110.6 (1988), pp. 1657–1666. doi: 10.1021/ja00214a001.
- Jurašin, D., M. Vinceković, A. Pustak, I. Šmit, M. Bujan, and N. Filipović-Vinceković. “Lamellar to Hexagonal Columnar Liquid Crystalline Phase Transition in a Catanionic Surfactant Mixture: Dodecylammonium Chloride–Sodium Bis(2-Ethylhexyl) Sulfosuccinate”. *Soft Matter* 9.12 (2013), p. 3349. doi: 10.1039/c3sm27665a.

- Kataoka, K., A. Harada, and Y. Nagasaki. "Block Copolymer Micelles for Drug Delivery: Design, Characterization and Biological Significance". *Adv. Drug Deliv. Rev.* 64 (2012), pp. 37–48. doi: 10.1016/j.addr.2012.09.013.
- Kennedy, J. and R. Eberhart. "Particle Swarm Optimization". In: *Proceedings of ICNN'95*. International Conference on Neural Networks. Perth, AU: IEEE, 1995, pp. 1942–1948. doi: 10.1109/ICNN.1995.488968.
- Kewalramani, S., H. Hlaing, B. M. Ocko, I. Kuzmenko, and M. Fukuto. "Effects of Divalent Cations on Phase Behavior and Structure of a Zwitterionic Phospholipid (DMPC) Monolayer at the Air–Water Interface". *J. Phys. Chem. Lett.* 1.2 (2010), pp. 489–495. doi: 10.1021/jz9002873.
- Khodakarimi, S., M. H. Hekmatshoar, and F. Abbasi. "X-Ray Reflectivity and Topography of the Solvent-Treated P3HT:PCBM Thin Films". *J. Mater. Sci. Mater. Electron.* 27.1 (2016), pp. 182–190. doi: 10.1007/s10854-015-3735-3.
- Kienzle, P. A., M. Douchet, D. J. McGilivray, K. V. O'Donovan, N. K. Berk, and C. F. Majkrzak. *NCNR Reflectometry Software*. URL: <http://www.ncnr.nist.gov/reflpak> (Accessed 2018-3-4).
- Kmiecik, S., D. Gront, M. Kolinski, L. Wieteska, A. E. Dawid, and A. Kolinski. "Coarse-Grained Protein Models and Their Applications". *Chem. Rev.* 116.14 (2016), pp. 7898–7936. doi: 10.1021/acs.chemrev.6b00163.
- Koutsoubas, A. "Combined Coarse-Grained Molecular Dynamics and Neutron Reflectivity Characterization of Supported Lipid Membranes". *J. Phys. Chem. B* 120.44 (2016), pp. 11474–11483. doi: 10.1021/acs.jpcb.6b05433.
- Kozhevnikov, I. V. "General Laws of X-Ray Reflection from Rough Surfaces: II. Conformal Roughness". *Crystallogr. Rep.* 57.4 (2012), pp. 490–498. doi: 10.1134/S1063774512030133.
- Kraack, H., B. M. Ocko, P. S. Pershan, E. Sloutskin, and M. Deutsch. "Structure of a Langmuir Film on a Liquid Metal Surface". *Science* 298.5597 (2002), pp. 1404–1407. doi: 10.1126/science.1078372.
- Kraft, D. J., J. Hilhorst, M. A. P. Heinen, M. J. Hoogenraad, B. Luigjes, and W. K. Kegel. "Patchy Polymer Colloids with Tunable Anisotropy Dimensions". *J. Phys. Chem. B* 115.22 (2011), pp. 7175–7181. doi: 10.1021/jp108760g.
- Kratky, O and G Porod. "Diffuse Small-Angle Scattering of x-Rays in Colloid Systems". *J. Colloid Sci.* 4.1 (1949), pp. 35–70. doi: 10.1016/0095-8522(49)90032-X.
- Krauth, W. *Statistical Mechanics: Algorithms and Computations*. Oxford Master Series in Statistical, Computational, and Theoretical Physics 13. Oxford, UK: Oxford University Press, 2006. ISBN: 978-0-19-851536-4.
- Kubo, I., S. Adachi, H. Maeda, and A. Seki. "Phosphatidylcholine Monolayers Observed with Brewster Angle Microscopy and

- A Isotherms". *Thin Solid Films* 393.1-2 (2001), pp. 80–85. doi: 10.1016/S0040-6090(01)01101-4.
- Kučerka, N., B. W. Holland, C. G. Gray, B. Tomberli, and J. Katsaras. "Scattering Density Profile Model of POPG Bilayers As Determined by Molecular Dynamics Simulations and Small-Angle Neutron and X-Ray Scattering Experiments". *J. Phys. Chem. B* 116.1 (2012), pp. 232–239. doi: 10.1021/jp208920h.
- Kučerka, N., M. A. Kiselev, and P. Balgavý. "Determination of Bilayer Thickness and Lipid Surface Area in Unilamellar Dimyristoylphosphatidylcholine Vesicles from Small-Angle Neutron Scattering Curves: A Comparison of Evaluation Methods". *Eur. Biophys. J.* 33.4 (2004), pp. 328–334. doi: 10.1007/s00249-003-0349-0.
- Kunz, K., J. Reiter, A. Goetzelmann, and M. Stamm. "Model-Free Analysis of Neutron Reflectivity Data from Polymer Thin Films with the Simulated Annealing Technique". *Macromolecules* 26.16 (1993), pp. 4316–4323. doi: 10.1021/ma00068a038.
- Leach, A. R. *Molecular Modelling: Principles and Applications*. Harlow, UK: Addison Wesley London Ltd, 1996. ISBN: 978-0-582-38210-7.
- Lennard-Jones, J. E. "On the Determination of Molecular Fields. II. From the Equation of State of a Gas". *Proc. Royal Soc. Lond. A.* 106.738 (1924), pp. 463–477. doi: 10.1098/rspa.1924.0082.
- Levenberg, K. "A Method for the Solution of Certain Non-Linear Problems in Least Squares". *Quart. Appl. Math.* 2.2 (1944), pp. 164–168. doi: 10.1090/qam/10666.
- Lindahl, E., B. Hess, and D. van der Spoel. "GROMACS 3.0: A Package for Molecular Simulation and Trajectory Analysis". *J. Mol. Model.* 7.8 (2001), pp. 306–317. doi: 10.1007/s008940100045.
- Lovell, M. R. and R. M. Richardson. "Analysis Methods in Neutron and X-Ray Reflectometry". *Curr. Opin. Colloid Interface Sci.* 4.3 (1999), pp. 197–204. doi: 10.1016/S1359-0294(99)00039-4.
- Lu, J. R., E. M. Lee, and R. K. Thomas. "The Analysis and Interpretation of Neutron and X-Ray Specular Reflection". *Acta Crystallogr. A* 52.1 (1996), pp. 11–41. doi: 10.1107/S0108767395011202.
- Lu, J. R., E. A. Simister, R. K. Thomas, and J. Penfold. "Some Aspects of the Structure of Amphiphilic Monolayers at the Air-Liquid Interface Determined by Neutron Reflection". *J. Phys. Condens. Matter* 6 (23A 1994), A403–A408. doi: 10.1088/0953-8984/6/23A/066.
- Magnussen, O. M., B. M. Ocko, M. Deutsch, M. J. Regan, P. S. Pershan, D. Abernathy, G. Grübel, and J.-F. Legrand. "Self-Assembly of Organic Films on a Liquid Metal". *Nature* 384 (1996), pp. 250–252. doi: 10.1038/384250a0.
- Marquardt, D. W. "An Algorithm for Least-Squares Estimation of Nonlinear Parameters". *J. Soc. Indust. Appl. Math.* 11.2 (1963), pp. 431–441. doi: 10.1137/0111030.

- Marrink, S. J., V. Corradi, P. C. T. Souza, H. I. Ingólfsson, D. P. Tieleman, and M. S. P. Sansom. "Computational Modeling of Realistic Cell Membranes". *Chem. Rev.* (2019), acs.chemrev.8b00460. doi: 10.1021/acs.chemrev.8b00460.
- Marrink, S. J., X. Periole, D. P. Tieleman, and A. H. de Vries. "Comment on "On Using a Too Large Integration Time Step in Molecular Dynamics Simulations of Coarse-Grained Molecular Models" by M. Winger, D. Trzesniak, R. Baron and W. F. van Gunsteren, *Phys. Chem. Chem. Phys.*, 2009, 11, 1934". *Phys. Chem. Chem. Phys.* 12.9 (2010), p. 2254. doi: 10.1039/b915293h.
- Marrink, S. J., H. J. Risselada, S. Yefimov, D. P. Tieleman, and A. H. de Vries. "The MARTINI Force Field: Coarse Grained Model for Biomolecular Simulations". *J. Phys. Chem. B* 111.27 (2007), pp. 7812–7824. doi: 10.1021/jp071097f.
- Marsh, D. "Molecular Volumes of Phospholipids and Glycolipids in Membranes". *Chem. Phy. Lipids* 163.7 (2010), pp. 667–677. doi: 10.1016/j.chmplyslip.2010.06.005.
- Martínez, L., R. Andrade, E. G. Birgin, and J. M. Martínez. "PACK-MOL: A Package for Building Initial Configurations for Molecular Dynamics Simulations". *J. Comput. Chem.* 30.13 (2009), pp. 2157–2164. doi: 10.1002/jcc.21224.
- McCluskey, A. R. and K. J. Edler. "Model-Dependent Small-Angle Scattering for the Study of Complex Organic Materials". *Curr. Org. Chem.* 22.8 (2018), pp. 750–757. doi: 10.2174/1875692115666170612104439.
- McCluskey, A. R., B. J. Morgan, K. J. Edler, and S. C. Parker. *Arm61/Pylj*: Pylj-1.1.0. 2018. url: <http://doi.org/10.5281/zenodo.1403828>.
- McCluskey, A. R., B. J. Morgan, K. J. Edler, and S. C. Parker. "Pylj: A Teaching Tool for Classical Atomistic Simulation". *J. Open Source Educ.* 1.2 (2018), pp. 19–21. doi: 10.21105/jose.00019.
- McCluskey, A. R., A. Sanchez-Fernandez, K. J. Edler, S. C. Parker, A. J. Jackson, R. A. Campbell, and T. Arnold. *Lipids_at_airdes* (Version 1.0). 2019. url: <http://doi.org/10.5281/zenodo.2577796>.
- McConlogue, C. W. and T. K. Vanderlick. "A Close Look at Domain Formation in DPPC Monolayers". *Langmuir* 13.26 (1997), pp. 7158–7164. doi: 10.1021/la970898e.
- MetalJet X-Ray Source Technology*. url: <https://www.excillum.com/technology/> (Accessed 2018-12-6).
- Metropolis, N., A.W. Rosenbluth, M. N. Rosenbluth, A. H. Teller, and E. Teller. "Equation of State Calculations by Fast Computing Machines". *J. Chem. Phys.* 21.6 (1953), pp. 1087–1092. doi: 10.1063/1.1699114.
- Michaud-Agrawal, N., E. J. Denning, T. B. Woolf, and O. Beckstein. "MDAnalysis: A Toolkit for the Analysis of Molecular Dynamics Simulations". *J. Comput. Chem.* 32.10 (2011), pp. 2319–2327. doi: 10.1002/jcc.21787.

- Miller, A. F., M. R. Wilson, M. J. Cook, and R. W. Richards. "Monte Carlo Simulations of an Amphiphilic Polymer at a Hydrophobic/Hydrophilic Interface". *Mol. Phys.* 101.8 (2003), pp. 1131–1138. doi: 10.1080/0026897031000068569.
- Miyamoto, S. and P. A. Kollman. "Settle: An Analytical Version of the SHAKE and RATTLE Algorithm for Rigid Water Models". *J. Comput. Chem.* 13.8 (1992), pp. 952–962. doi: 10.1002/jcc.540130805.
- Mohwald, H. "Phospholipid and Phospholipid-Protein Monolayers at the Air-Water Interface". *Annu. Rev. Phys. Chem.* 41 (1990), pp. 441–476. doi: 10.1146/annurev.pc.41.100190.002301.
- Morse, P. M. "Diatom Molecules According to the Wave Mechanics. II. Vibrational Levels". *Phys. Rev.* 34.1 (1929), pp. 57–64. doi: 10.1103/PhysRev.34.57.
- Nawaz, S., M. Redhead, G. Mantovani, C. Alexander, C. Bosquillon, and P. Carbone. "Interactions of PEO-PPO-PEO Block Copolymers with Lipid Membranes: A Computational and Experimental Study Linking Membrane Lysis with Polymer Structure". *Soft Matter* 8.25 (2012), p. 6744. doi: 10.1039/c2sm25327e.
- Negro, E., R. Latsuzbaia, A. H. de Vries, and G. J. M. Koper. "Experimental and Molecular Dynamics Characterization of Dense Microemulsion Systems: Morphology, Conductivity and SAXS". *Soft Matter* 10.43 (2014), pp. 8685–8697. doi: 10.1039/C4SM01763C.
- Nelson, A. R. J. "Co-Refinement of Multiple-Contrast Neutron/X-Ray Reflectivity Data Using MOTOFIT". *J. Appl. Crystallogr.* 39.2 (2006), pp. 273–276. doi: 10.1107/S0021889806005073.
- Nelson, A. R. J. "Towards a Detailed Resolution Smearing Kernel for Time-of-Flight Neutron Reflectometers. Corrigendum". *J. Appl. Crystallogr.* 47.3 (2014), p. 1162. doi: 10.1107/S1600576714009595.
- Nelson, A. R. J. and C. D. Dewhurst. "Towards a Detailed Resolution Smearing Kernel for Time-of-Flight Neutron Reflectometers". *J. Appl. Crystallogr.* 46.5 (2013), pp. 1338–1346. doi: 10.1107/S0021889813021936.
- Nelson, A. R. J. and S. W. Prescott. "Refnx: Neutron and X-Ray Reflectometry Analysis in Python". *J. Appl. Crystallogr.* 52.1 (2019), pp. 193–200. doi: 10.1107/S1600576718017296.
- Nelson, A. R. J., S. W. Prescott, I. Gresham, and A. R. McCluskey. *Refnx v0.1.2. 2019.* url: <http://doi.org/10.5281/zenodo.2552023>.
- Nérot, L. and P. Croce. "Caractérisation Des Surfaces Par Réflexion Rasante de Rayons X. Application à l'étude Du Polissage de Quelques Verres Silicates". *Rev. Phys. Appl. (Paris)* 15.3 (1980), pp. 761–779. doi: 10.1051/rphysap:01980001503076100.
- Nosé, S. "A Unified Formulation of the Constant Temperature Molecular Dynamics Methods". *J. Chem. Phys.* 81.1 (1984), pp. 511–519. doi: 10.1063/1.447334.

- Ott, F. *SimulReflec*. URL: <http://www-l1b.cea.fr/prism/programs/simulreflec/simulreflec.html> (Accessed 2019-3-4).
- Owejan, J. E., J. P. Owejan, S. C. DeCaluwe, and J. A. Dura. "Solid Electrolyte Interphase in Li-Ion Batteries: Evolving Structures Measured In Situ by Neutron Reflectometry". *Chem. Mater.* 24.11 (2012), pp. 2133–2140. doi: 10.1021/cm3006887.
- Pambou, E., J. Crewe, M. Yaseen, F. N. Padia, S. Rogers, D. Wang, H. Xu, and J. R. Lu. "Structural Features of Micelles of Zwitterionic Dodecyl-Phosphocholine (C₁₂ PC) Surfactants Studied by Small-Angle Neutron Scattering". *Langmuir* 31.36 (2015), pp. 9781–9789. doi: 10.1021/acs.langmuir.5b02077.
- Pan, J., F. A. Heberle, S. Tristram-Nagle, M. Szymanski, M. Koepfinger, J. Katsaras, and N Kučerka. "Molecular Structures of Fluid Phase Phosphatidylglycerol Bilayers as Determined by Small Angle Neutron and X-Ray Scattering". *BBA - Biomembranes* 1818.9 (2012), pp. 2135–2148. doi: 10.1016/j.bbamem.2012.05.007.
- Pandey, A., R. Rai, M. Pal, and S. Pandey. "How Polar Are Choline Chloride-Based Deep Eutectic Solvents?" *Phys. Chem. Chem. Phys.* 16.4 (2014), pp. 1559–1568. doi: 10.1039/C3CP53456A.
- Pandit, S. A., D. Bostick, and M. L. Berkowitz. "An Algorithm to Describe Molecular Scale Rugged Surfaces and Its Application to the Study of a Water/Lipid Bilayer Interface". *J. Chem. Phys.* 119.4 (2003), pp. 2199–2205. doi: 10.1063/1.1582833.
- Parratt, L. G. "Surface Studies of Solids by Total Reflection of X-Rays". *Phys. Rev.* 95.2 (1954), pp. 359–369. doi: 10.1103/PhysRev.95.359.
- Parrinello, M. and A. Rahman. "Polymorphic Transitions in Single Crystals: A New Molecular Dynamics Method". *J. Appl. Phys.* 52.12 (1981), pp. 7182–7190. doi: 10.1063/1.328693.
- Pearson, K. "Notes on Regression and Inheritance in the Case of Two Parents". *Proc. Royal Soc. Lond.* 58 (1895), pp. 240–242.
- Pedersen, J. S. "Monte Carlo Simulation Techniques Applied in the Analysis of Small-Angle Scattering Data from Colloids and Polymer System". In: *Neutron, X-Rays and Light. Scattering Methods Applied to Soft Condensed Matter*. Ed. by Th. Zemb and P. Lindner. Amsterdam, NL: Elsevier Science B.V., 2002, pp. 381–390. ISBN: 978-0-08-093013-8.
- Pluhackova, K. and R. A. Böckmann. "Biomembranes in Atomistic and Coarse-Grained Simulations". *J. Phys. Condens. Matter* 27.32 (2015), p. 323103. doi: 10.1088/0953-8984/27/32/323103.
- Poli, R. "Analysis of the Publications on the Applications of Particle Swarm Optimisation". *J. Artif. Evol. Appl.* 2008 (2008), pp. 1–10. doi: 10.1155/2008/685175.
- Politsch, E. and G. Cevc. "Unbiased Analysis of Neutron and X-Ray Reflectivity Data by an Evolution Strategy". *J. Appl. Crystallogr.* 35.3 (2002), pp. 347–355. doi: 10.1107/S0021889802004351.

- Rahman, A. "Correlations in the Motion of Atoms in Liquid Argon". *Phys. Rev.* 136 (2A 1964), A405–A411. doi: 10.1103/PhysRev.136.A405.
- RCSB PDB: Protein Data Bank.* url: <http://www.rcsb.org> (Accessed 2018-1-28).
- Ribeiro, B. D., C. Florindo, L. C. Iff, M. A. Z. Coelho, and I. M. Marrucho. "Menthol-Based Eutectic Mixtures: Hydrophobic Low Viscosity Solvents". *ACS Sustain. Chem. Eng.* 3.10 (2015), pp. 2469–2477. doi: 10.1021/acssuschemeng.5b00532.
- Rodriguez-Loureiro, I., E. Scoppola, L. Bertinetti, A. Barbetta, G. Fragneto, and E. Schneck. "Neutron Reflectometry Yields Distance-Dependent Structures of Nanometric Polymer Brushes Interacting across Water". *Soft Matter* 13.34 (2017), pp. 5767–5777. doi: 10.1039/C7SM01066D.
- Rondelli, V., G. Fragneto, S. S., E. Del Favero, and L. Cantù. "Reflectivity from Floating Bilayers: Can We Keep the Structural Asymmetry?" *J. Phys. Conf. Ser.* 340 (2012), p. 012083. doi: 10.1088/1742-6596/340/1/012083.
- Rose, D. R., J. Phipps, J. Michniewicz, G. I. Birnbaum, F. R. Ahmed, A. Muir, W. F. Anderson, and S. Narang. "Crystal Structure of T4-Lysozyme Generated from Synthetic Coding DNA Expressed in Escherichia Coli". *Protein Eng. Des. Sel.* 2.4 (1988), pp. 277–282. doi: 10.1093/protein/2.4.277.
- Rosen, M. J. and J. T. Kunjappu. *Surfactants and Interfacial Phenomena*. 4th ed. Hoboken, USA: John Wiley & Sons, 2012. ISBN: 978-0-470-54194-4.
- Rudd, R. E and J. Q. Broughton. "Coarse-Grained Molecular Dynamics and the Atomic Limit of Finite Elements". *Phys. Rev. B* 58.10 (1998), R5893–R5896. doi: 10.1103/PhysRevB.58.R5893.
- Sammalkorpi, M., M. Karttunen, and M. Haataja. "Ionic Surfactant Aggregates in Saline Solutions: Sodium Dodecyl Sulfate (SDS) in the Presence of Excess Sodium Chloride (NaCl) or Calcium Chloride (CaCl₂)". *J. Phys. Chem. B* 113.17 (2009), pp. 5863–5870. doi: 10.1021/jp901228v.
- Sanchez-Fernandez, A., T. Arnold, A. J. Jackson, S. L. Fussell, R. K. Heenan, R. A. Campbell, and K. J. Edler. "Micellization of Alkyltrimethylammonium Bromide Surfactants in Choline Chloride:Glycerol Deep Eutectic Solvent". *Phys. Chem. Chem. Phys.* 18.48 (2016), pp. 33240–33249. doi: 10.1039/C6CP06053F.
- Sanchez-Fernandez, A., K. J. Edler, T. Arnold, D. Alba Venero, and A. J. Jackson. "Protein Conformation in Pure and Hydrated Deep Eutectic Solvents". *Phys. Chem. Chem. Phys.* 19.13 (2017), pp. 8667–8670. doi: 10.1039/C7CP00459A.
- Sanchez-Fernandez, A., O. S. Hammond, K. J. Edler, T. Arnold, J. Doutch, R. M. Dalgliesh, P. Li, K. Ma, and A. J. Jackson. "Counterion Binding Alters Surfactant Self-Assembly in Deep Eutectic

- Solvents". *Phys. Chem. Chem. Phys.* 20.20 (2018), pp. 13952–13961. doi: 10.1039/C8CP01008K.
- Sanchez-Fernandez, A., G. L. Moody, L. C. Murfin, T. Arnold, A. J. Jackson, S. M. King, S. E. Lewis, and K. J. Edler. "Self-Assembly and Surface Behaviour of Pure and Mixed Zwitterionic Amphiphiles in a Deep Eutectic Solvent". *Soft Matter* 14.26 (2018), pp. 5525–5536. doi: 10.1039/C8SM00755A.
- Sanders, S. A. and A. Z. Panagiotopoulos. "Micellization Behavior of Coarse Grained Surfactant Models". *J. Chem. Phys.* 132.11 (2010), p. 114902. doi: 10.1063/1.3358354.
- Sapir, L., C. B. Stanley, and D. Harries. "Properties of Polyvinylpyrrolidone in a Deep Eutectic Solvent". *J. Phys. Chem. A* 120.19 (2016), pp. 3253–3259. doi: 10.1021/acs.jpca.5b11927.
- Schmaljohann, D. "Thermo- and pH-Responsive Polymers in Drug Delivery". *Adv. Drug Deliv. Rev.* 58.15 (2006), pp. 1655–1670. doi: 10.1016/j.addr.2006.09.020.
- Schnablegger, H. and Y. Singh. *The SAXS Guide: Getting Acquainted with the Principles*. 4th ed. Graz, AT: Anton Paar GmbH, 2017.
- Schramm, L. L., E. N. Stasiuk, and D. G. Marangoni. "Surfactants and Their Applications". *Annu. Rep. Prog. Chem., Sect. C: Phys. Chem.* 99 (2003), pp. 3–48. doi: 10.1039/B208499F.
- Scoppola, E. and E. Schneck. "Combining Scattering and Computer Simulation for the Study of Biomolecular Soft Interfaces". *Curr. Opin. Colloid Interface Sci.* 37 (2018), pp. 88–100. doi: 10.1016/j.cocis.2018.06.008.
- Segala, E., D. Guo, R. K. Y. Cheng, A. Bortolato, F. Deflorian, A. S. Doré, J. C. Errey, L. H. Heitman, A. P. IJzerman, F. H. Marshall, and R. M. Cooke. "Controlling the Dissociation of Ligands from the Adenosine A_{2A} Receptor through Modulation of Salt Bridge Strength". *J. Med. Chem.* 59.13 (2016), pp. 6470–6479. doi: 10.1021/acs.jmedchem.6b00653.
- Shapiro, S. S. and M. B. Wilk. "An Analysis of Variance Test for Normality (Complete Samples)". *Biometrika* 52.3-4 (1965), pp. 591–611. doi: 10.1093/biomet/52.3-4.591.
- Shi, Y. and R. Eberhart. "A Modified Particle Swarm Optimizer". In: *1998 IEEE International Conference on Evolutionary Computation Proceedings*. IEEE World Congress on Computational Intelligence. Anchorage, US: IEEE, 1998, pp. 69–73. doi: 10.1109/ICEC.1998.699146.
- Simons, K. and D. Toomre. "Lipid Rafts and Signal Transduction". *Nat. Rev. Mol. Cell Biol.* 1 (2000), pp. 31–39. doi: 10.1038/35036052.
- Sivia, D. S. *Elementary Scattering Theory: For X-Ray and Neutron Users*. Oxford, UK: Oxford University Press, 2011. ISBN: 978-0-19-922868-3.
- Sivia, D. S., W. I. F. David, K. S. Knight, and S. F. Gull. "An Introduction to Bayesian Model Selection". *Physica D* 66.1-2 (1993), pp. 234–242. doi: 10.1016/0167-2789(93)90241-R.

- Sivia, D. S., W. A. Hamilton, and G. S. Smith. "Analysis of Neutron Reflectivity Data: Maximum Entropy, Bayesian Spectral Analysis and Speckle Holography". *Physica B* 173.1-2 (1991), pp. 121–138. doi: 10.1016/0921-4526(91)90042-D.
- Sivia, D. S. and J. Skilling. *Data Analysis: A Bayesian Tutorial*. 2nd ed. Oxford: Oxford University Press, 2006. ISBN: 978-0-19-856832-2.
- Sivia, D. S. and J. R. P. Webster. "The Bayesian Approach to Reflectivity Data". *Physica B* 248.1-4 (1998), pp. 327–337. doi: 10.1016/S0921-4526(98)00259-2.
- Skou, S., R. E. Gillilan, and N. Ando. "Synchrotron-Based Small-Angle X-Ray Scattering of Proteins in Solution". *Nat. Protoc.* 9.7 (2014), pp. 1727–1739. doi: 10.1038/nprot.2014.116.
- Small, D. "Lateral Chain Packing in Lipids and Membranes". *J. Lipids Res.* 25 (1984), pp. 1490–1500.
- Smith, E. L., A. P. Abbott, and K. S. Ryder. "Deep Eutectic Solvents (DESs) and Their Applications". *Chem. Rev.* 114.21 (2014), pp. 11060–11082. doi: 10.1021/cr300162p.
- Storn, R. and K. Price. "Differential Evolution – A Simple and Efficient Heuristic for Global Optimization over Continuous Spaces". *J. Global Optim.* 11 (1997), pp. 341–359. doi: 10.1023/A:1008202821328.
- Sun, W.-J., R. M. Suter, M. A. Knewton, C. R. Worthington, S. Tristram-Nagle, R. Zhang, and J. F. Nagle. "Order and Disorder in Fully Hydrated Unoriented Bilayers of Gel-Phase Dipalmitoylphosphatidylcholine". *Phys. Rev. E* 49.5 (1994), pp. 4665–4676. doi: 10.1103/PhysRevE.49.4665.
- Swope, W. C., H. C. Andersen, P. H. Berens, and K. R. Wilson. "A Computer Simulation Method for the Calculation of Equilibrium Constants for the Formation of Physical Clusters of Molecules: Application to Small Water Clusters". *J. Chem. Phys.* 76.1 (1982), pp. 637–649. doi: 10.1063/1.442716.
- Tanford, C. *The Hydrophobic Effect: Formation of Micelles and Biological Membranes*. 2nd ed. New York: John Wiley & Sons, 1980. ISBN: 978-0-471-04893-0.
- Tieleman, D. P., J. L. MacCallum, W. L. Ash, C. Kandt, Z. Xu, and L. Monticelli. "Membrane Protein Simulations with a United-Atom Lipid and All-Atom Protein Model: Lipid–Protein Interactions, Side Chain Transfer Free Energies and Model Proteins". *J. Phys. Condens. Matter* 18.28 (2006), S1221–S1234. doi: 10.1088/0953-8984/18/28/S07.
- Ulyanenkov, A., K. Omote, and J. Harada. "The Genetic Algorithm: Refinement of X-Ray Reflectivity Data from Multilayers and Thin Films". *Physica B* 283 (2000), pp. 237–241. doi: 10.1016/S0921-4526(99)01972-9.
- Ulyanenkov, A. and S. Sobolewski. "Extended Genetic Algorithm: Application to x-Ray Analysis". *J. Phys. D* 38 (10A 2005), A235–A238. doi: 10.1088/0022-3727/38/10A/046.

- Uusitalo, J. J., H. I. Ingólfsson, P. Akhshi, D. P. Tieleman, and S. J. Marrink. "Martini Coarse-Grained Force Field: Extension to DNA". *J. Chem. Theory Comput.* 11.8 (2015), pp. 3932–3945. doi: 10.1021/acs.jctc.5b00286.
- Vaknin, D., K. Kjaer, J. Als-Nielsen, and M. Lösche. "Structural Properties of Phosphatidylcholine in a Monolayer at the Air/Water Interface". *Biophys. J.* 59.6 (1991), pp. 1325–1332. doi: 10.1016/S0006-3495(91)82347-5.
- Van der Spoel, D., E. Lindahl, B. Hess, G. Groenhof, A. E. Mark, and H. J. C. Berendsen. "GROMACS: Fast, Flexible, and Free". *J. Comput. Chem.* 26.16 (2005), pp. 1701–1718. doi: 10.1002/jcc.20291.
- Van Osch, D. J. G. P., L. F. Zubeir, A. van den Bruinhorst, M. A. A. Rocha, and M. C. Kroon. "Hydrophobic Deep Eutectic Solvents as Water-Immiscible Extractants". *Green Chem.* 17.9 (2015), pp. 4518–4521. doi: 10.1039/C5GC01451D.
- Von Hansen, Y., S. Gekle, and R. R. Netz. "Anomalous Anisotropic Diffusion Dynamics of Hydration Water at Lipid Membranes". *Phys. Rev. Lett.* 111.11 (2013), pp. 118103–118105. doi: 10.1103/PhysRevLett.111.118103.
- Wang, S. and R. G. Larson. "Coarse-Grained Molecular Dynamics Simulation of Self-Assembly and Surface Adsorption of Ionic Surfactants Using an Implicit Water Model". *Langmuir* 31.4 (2015), pp. 1262–1271. doi: 10.1021/la503700c.
- Watkins, E. B., C. E. Miller, D. J. Mulder, T. L. Kuhl, and J. Majewski. "Structure and Orientational Texture of Self-Organizing Lipid Bilayers". *Phys. Rev. Lett.* 102.23 (2009), pp. 238101–238104. doi: 10.1103/PhysRevLett.102.238101.
- Weinbach, S. P., K. Kjaer, J. Als-Nielsen, M. Lahav, and L. Leiserowitz. "Self-Assembled Langmuir Monolayers and Trilayers at the Air-Formamide Interface". *J. Phys. Chem.* 97.20 (1993), pp. 5200–5203. doi: 10.1021/j100122a003.
- Willis, B. T. M. and C. J. Carlile. *Experimental Neutron Scattering*. Oxford, UK: Oxford University Press, 2009. ISBN: 978-0-19-967377-3.
- Wojciechowski, K., M. Orczyk, T. Gutberlet, G. Brezesinski, T. Geue, and P. Fontaine. "On the Interaction between Digitonin and Cholesterol in Langmuir Monolayers". *Langmuir* 32.35 (2016), pp. 9064–9073. doi: 10.1021/acs.langmuir.6b01737.
- Wojciechowski, K., M. Orczyk, T. Gutberlet, and T. Geue. "Complexation of Phospholipids and Cholesterol by Triterpenic Saponins in Bulk and in Monolayers". *BBA - Biomembranes* 1858.2 (2016), pp. 363–373. doi: 10.1016/j.bbamem.2015.12.001.
- Wormington, M., C. Panaccione, K. M. Matney, and D. K. Bowen. "Characterization of Structures from X-Ray Scattering Data Using Genetic Algorithms". *Philos. Trans. R. Soc. London Ser. A* 357.1761 (1999), pp. 2827–2848. doi: 10.1098/rsta.1999.0469.

- Wu, G., R. Mallipeddi, and P. N. Suganthan. "Ensemble Strategies for Population-Based Optimization Algorithms – A Survey". *Swarm Evol. Comput.* 44 (2019), pp. 695–711. doi: 10.1016/j.swevo.2018.08.015.
- Xue, M., L. Cheng, I. Faustino, W. Guo, and S. J. Marrink. "Molecular Mechanism of Lipid Nanodisk Formation by Styrene-Maleic Acid Copolymers". *Biophys. J.* 115.3 (2018), pp. 494–502. doi: 10.1016/j.bpj.2018.06.018.
- Yeh, I.-C. and M. L. Berkowitz. "Ewald Summation for Systems with Slab Geometry". *J. Chem. Phys.* 111.7 (1999), pp. 3155–3162. doi: 10.1063/1.479595.
- Yesylevskyy, S. O., L. V. Schäfer, D. Sengupta, and S. J. Marrink. "Polarizable Water Model for the Coarse-Grained MARTINI Force Field". *PLoS Comput. Biol.* 6.6 (2010). Ed. by M. Levitt, e1000810. doi: 10.1371/journal.pcbi.1000810.
- Zagnoni, M. "Miniaturised Technologies for the Development of Artificial Lipid Bilayer Systems". *Lab on a Chip* 12.6 (2012), p. 1026. doi: 10.1039/c2lc20991h.
- Zahn, S., B. Kirchner, and D. Mollenhauer. "Charge Spreading in Deep Eutectic Solvents". *ChemPhysChem* 17.21 (2016), pp. 3354–3358. doi: 10.1002/cphc.201600348.
- Zhou, X.-L. and S.-H. Chen. "Theoretical Fundation of X-Ray and Neutron Reflectometry". *Phys. Rep.* 257 (1995), pp. 223–348. doi: 10.1016/0370-1573(94)00110-O.
- Zhou, Xiao-Lin and Sow-Hsin Chen. "Model-Independent Method for Reconstruction of Scattering-Length-Density Profiles Using Neutron or x-Ray Reflectivity Data". *Physical Review E* 47.5 (1993), pp. 3174–3190. doi: 10.1103/PhysRevE.47.3174.